4.2c) is normally used for nDEP where particles experiencing negative DEP that are in the plane of the electrodes will be trapped in the center of the electrodes. Figure 4.2d shows schematic of array of microelectrodes (~3 μm diameter) that are used to manipulate cells.[155] The electrode geometry/size plays a key role in controlling the factor ∇E^2, which has dimensions of V^2/m^3.[151-152]

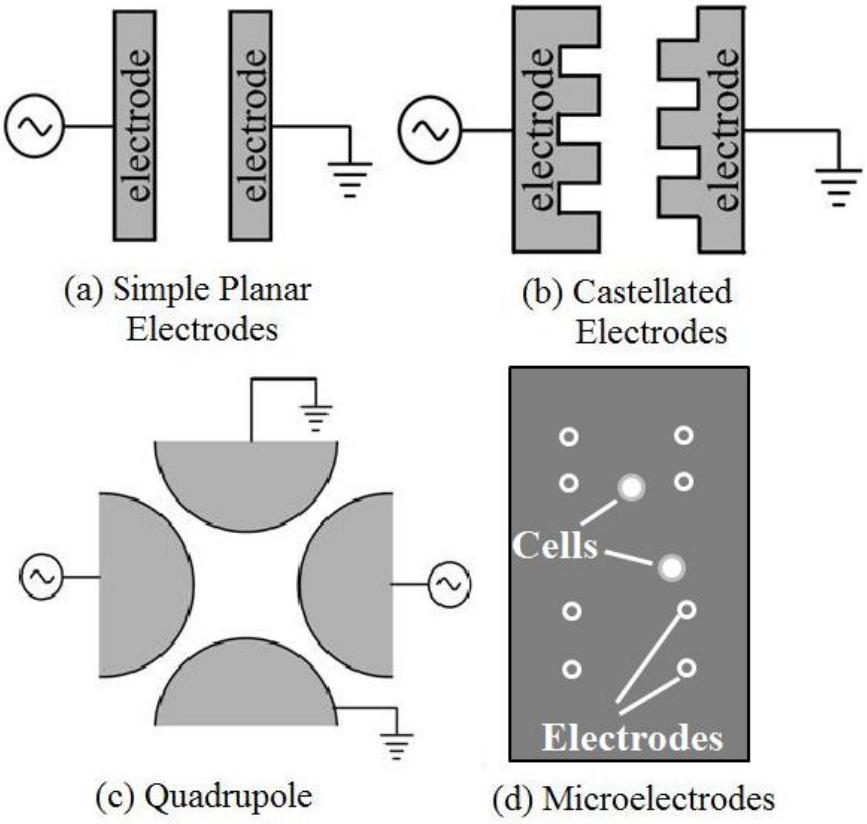

Figure 4.2 Commonly employed electrode geometries for DEP experiments. (a-c: Adapted with permission from ref. 150. Copyright © 2004, American Scientific Publishers; d: Adapted with permission from ref. 155. Copyright © 2004, with permission from Elsevier.)

4.4 Predicting Clausius Mossotti factor using homogeneous sphere model

DEP has been widely used to manipulate biological particles such as bacteria,[70, 137] viruses,[156] spores,[157] yeast[158] and other eukaryotic cell types as well as proteins,[159] nucleic acids,[147, 160] and other biomolecules. These bioparticles have more complicated internal structure and inhomogeneous composition than that of a solid homogeneous spherical particle. Though the structures are complicated, the fundamental physics does not change much if they are properly

accounted for while calculating the DEP force. To account for their heterogeneous structure they can be modeled using single (cross-over frequency determination), and smeared-out multishell model.[161-164] Depending on the availability of parameters from literature, either of these two approaches can be employed to calculate the dependence of CM factor on the frequency of the applied field. Let us now, look at how we can use multi-shell model to predict the DEP behavior of bioparticles, in particular *E. coli* cells, and vaccina virus. This kind of prediction will be very helpful when one want to separate or manipulate a single bioparticle from a heterogeneous mixture.

To predict the DEP response of *E. coli* cells, it is convenient to model it as a sphere covered by two shells (inner shell: cytoplasmic membrane, outer shell: cell wall) as shown in Figure 4.3. The complex permittivity of *E. coli* (ε_p^*) cells has to be replaced with an effective complex permittivity (ε_{eff}^*) which is calculated using the multishell smeared-out sphere model (see Equation 4.3).

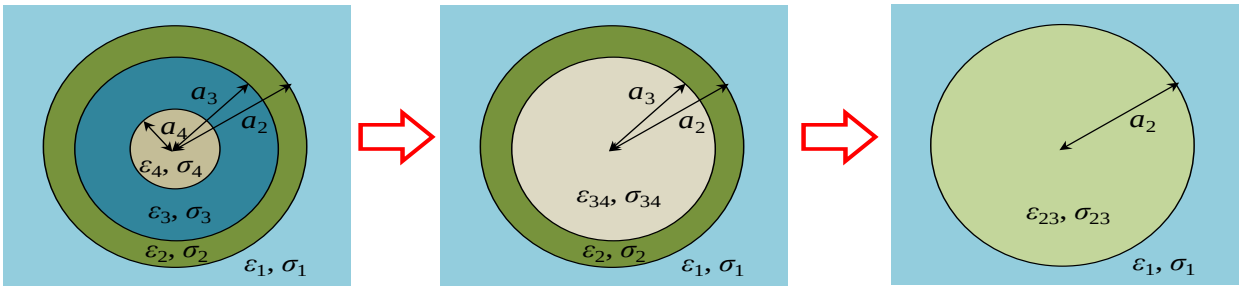

Figure 4.3 Schematic of three shell "smeared-out" model approach for calculating effective permittivity (ε_{eff}^*) of *E. coli* cells.

$$\varepsilon_{34}^* = \varepsilon_3 \frac{\left(\frac{a_3}{a_4}\right)^3 + 2\left(\frac{\varepsilon_4^* - \varepsilon_3^*}{\varepsilon_4^* + 2\varepsilon_3^*}\right)}{\left(\frac{a_3}{a_4}\right)^3 - \left(\frac{\varepsilon_4^* - \varepsilon_3^*}{\varepsilon_4^* + 2\varepsilon_3^*}\right)}; \varepsilon_{23}^*(\varepsilon_{Eff}^*) = \varepsilon_2^* \frac{\left(\frac{a_2}{a_3}\right)^3 + 2\left(\frac{\varepsilon_{34}^* - \varepsilon_2^*}{\varepsilon_{34}^* + 2\varepsilon_2^*}\right)}{\left(\frac{a_2}{a_3}\right)^3 - \left(\frac{\varepsilon_{34}^* - \varepsilon_2^*}{\varepsilon_{34}^* + 2\varepsilon_2^*}\right)}; CM(\omega) = \frac{\varepsilon_{eff}^* - \varepsilon_1^*}{\varepsilon_{eff}^* + 2\varepsilon_1^*} \quad \textbf{(4.3)}$$

The parameters used for the calculation of ε_{eff}^* for *E. coli* cells can be found from previous reports,[134, 165-166] which are listed below in Table 4.1. In most of the DEP experiments water or buffer is preferred as the suspending medium. So, the only parameter which can be varied is the conductivity of the suspending medium. Different scenarios of the dependence of

CM factor based on the conductivity of the suspended medium can be deduced using the Equation 4.3 and the values presented in Table 4.1.

Table 4.1 Parameter values used for theoretical predictions of Re[CM(ω)] for *E. coli* cells.[134]

Component	**Parameter**	**Value**
Cell	Radius	1 μm
Cell cytoplasm	Relative perimittivity (ε_4)	60
	Conductivity (σ_4)	0.1 S/m
Cell membrane	Relative perimittivity (ε_3)	10
	Conductivity (σ_3)	50 nS/m
	Thickness	5 nm
Cell wall	Relative perimittivity (ε_2)	60
	Conductivity (σ_2)	0.5 S/m
	Thickness	20 nm
Suspension medium (DI water)	Relative perimittivity (ε_1)	80
	Conductivity (σ_1)	**Variable** S/m

Similar kind of predictions about the CM factor can also be done for smaller bioparticles like vaccine virus. In case of viruses, the model is simpler due to absence of a cell wall and cell membrane as shown in Figure 4.4. The complex permittivity of *E. coli* (ε_p^*) cells has to be replaced with an effective complex permittivity (ε_{eff}^*) which is calculated using the two shell smeared-out sphere model (see Equation 4.4). The parameters used for the calculation of ε_{eff}^* for vaccina virus can be found from previous reports[136], which are listed in Table 4.2.

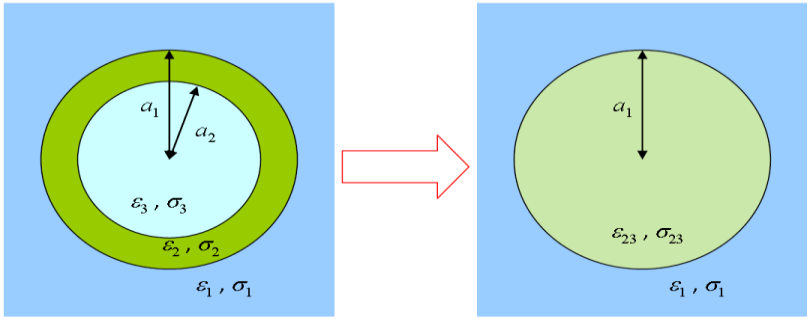

Figure 4.4 Schematic of two shell "smeared-out" model approach for calculating effective permittivity (ε_{eff}^*) of vaccina virus.

$$\bar{\varepsilon}_{23}(\varepsilon^*_{eff}) = \bar{\varepsilon}_2 \frac{\left(\frac{a_1}{a_2}\right)^3 + 2\left(\frac{\bar{\varepsilon}_3 - \bar{\varepsilon}_2}{\bar{\varepsilon}_3 + 2\bar{\varepsilon}_2}\right)}{\left(\frac{a_1}{a_2}\right)^3 - \left(\frac{\bar{\varepsilon}_3 - \bar{\varepsilon}_2}{\bar{\varepsilon}_3 + 2\bar{\varepsilon}_2}\right)} \quad ; \quad f_{CM,23} = \frac{\varepsilon^*_{eff} - \bar{\varepsilon}_1}{\varepsilon^*_{eff} + 2\bar{\varepsilon}_1} \qquad \textbf{(4.4)}$$

Table 4.2 Parameter values used for theoretical predictions of Re[CM(ω)] for vaccina virus.[136]

Component	**Parameter**	**Value**
Bulk	Relative permittivity (ε_3)	65
	Conductivity (σ_3)	1.6×10^{-1} S/m
Membrane	Relative permittivity (ε_2)	10.3
	Conductivity (σ_2)	0.19×10^{-9} S/m
	Thickness	20 nm
Suspension medium (DI water)	Relative permittivity (ε_1)	80
	Conductivity (σ_1)	**Variable** S/m

Using the values listed in Table 4.1 and Table 4.2, the predict spectra of CM factor vs. different frequencies of the AC voltage at various suspending medium conductivities of the *E. coli* cells and vaccine virus is shown in Figure 4.5. Suspending medium conductivities of 0.1, 0.01, and 0.001 S/m were selected in this case.

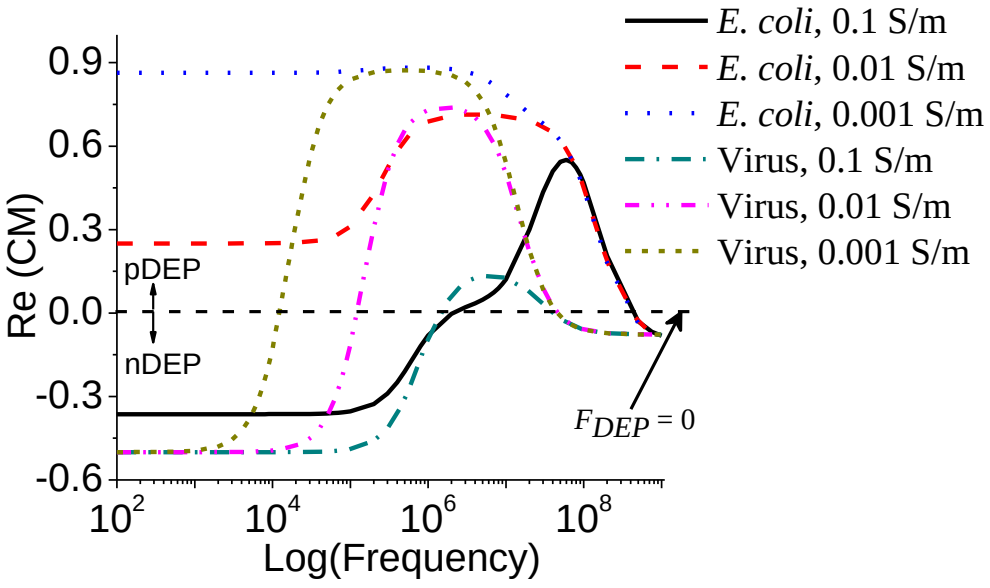

Figure 4.5 DEP Spectrum of *E. coli* cells and Vaccinia virus at medium conductivities of 0.1, 0.01, and 0.001 S/m.

The excel sheet template programmed to calculate the effective permittivity and there by the CM factor for both *E. coli* cells and vaccina virus are attached as supplementary files. It can be observed from Figure 4.5 that, at low suspending medium conductivities (0.01 or 0.001 S/m) and lower frequencies (1-10 kHz), the *E. coli* cells always have a positive value of CM factor leading to a pDEP force, whereas vaccina virus has a negative value of CM factor there by experiencing nDEP. These observations can be very useful for future studies dealing with *E. coli* cells or viruses individually or together.

4.5 Experimental details

4.5.1 DEP Device Fabrication

Fabrication of the DEP device (see Appendix Figure B.1) involves five major steps: (1) preparation of a randomly distributed VACNF NEA covering the whole surface of a Si chip of 1 cm x 2 cm in size, (2) UV-lithography patterning to define an active capture area (200 μm x 200 μm) on the VACNF NEA chip using a 2 μm thick SU-8 photoresist (see Figure 4.7a), (3) UV-lithographic patterning a microchannel of 500 μm in width with a 2 mm diameter circle on a ITO-glass substrate (1 cm x 2 cm) using a 18 μm thick SU-8 photoresist (see Figure 4.7a), (4) aligning and bonding of SU-8 patterned NEA chip and ITO substrates, and (5) making fluidic and electrical connections. The details of each step are given below.

(1) Embedded VACNF NEAs were made by the method described in chapter 2 (see section 2.2).

(2) SU-8 2002 photoresist (Microchem, Newton, MA) of ~2.0 μm in thickness was used to develop patterns on the planarized NEA. The substrate was cleaned by rinsing with acetone several times, blow-dried in air and dehydrated at 150 ^{o}C for 20 min in an oven (Fisher Scientific, 3510-1FS). SU-8 2002 was spin coated on NEA chip at 2800 rpm speed for 40 sec using a spin coater. It was soft-baked at 95 ^{o}C for 75 sec on a hot plate, exposed to UV light (44 mW/cm^2) for 3 sec through a Mylar mask in soft contact mode to define a 200 μm x 200 μm active area, post baked for 90 sec on a hot plate at 95 ^{o}C, developed in SU-8 developer, and washed with isopropyl alcohol (IPA) and dried using a stream of dry N_2.

(3) SU-8 2010 photoresist (Microchem, Newton, MA) of ~18 μm in thickness was deposited on a 2 cm x 4 cm ITO-coated glass electrode by spin coating SU-8 2010 at 1350 rpm speed for 40 sec. It was then soft baked at 95 ^{o}C for 4 min on a hot plate, exposed to UV light

(44 mW/cm^2) for 5.7 sec through the second Mylar mask to define the microchannel and circular chamber, post baked for 4 min at 95 ^{o}C on a hot plate. The remaining steps were the same as explained for NEAs. Finally, two holes were drilled from glass side using a 0.75 mm diameter diamond drill bit at the two ends of the microchannel and then a section (1 cm x 2 cm) of ITO-glass electrode containing the microchannel was diced to eliminate edge-beads, which may interfere with the bonding process.

(4) SU-8 patterned NEA and ITO-glass electrodes were cleaned with IPA to remove dust particles. Alignment markers on both the substrates were used to align them under a regular table top microscope with a 4X objective lens and then a mechanical force was applied to hold the substrates together (see Figure 4.7a and Figure 4.7b). Subsequently, the substrates were placed in a vacuum oven (Curtin Matheson Scientific, Inc) which was preheated to 175 ^{o}C. It was evacuated and held at 25 Torr for ~20 min for the substrates to bond with each other.

(5) Electrical connections to the electrical pads on the NEA and ITO-glass were made using conductive silver epoxy (MG Chemicals, Ontario) and thirty gauge wire. Microbore tubing was connected from a 1 ml glass syringe to the DEP device using sleeves, ferrules and fittings (Upchurch Scientific Inc, WA). A syringe pump (NE-1000, New Era Pump Systems, Inc) was used to control the flow rate during the experiments.

4.5.2 E. coli cell culture and labeling

Frozen *E. coli* DHα5 stock was purchased from Fisher (18265-017) and stored at -80 ^{o}C. For bacterial culture, the stock was thawed on ice for 20 min and inoculated in 2.0 ml LB medium in a sterile culture tube and incubated overnight at 37 ^{o}C. For each DEP experiment, 20 µl of grown culture was transferred into 2.0 ml of fresh LB media and incubated at 37 ^{o}C to reach a cell concentration of ~1 x 10^9 cells/ml into the late log phase. Bacterial cell counting was done using a Petroff-Hausser counting chamber. The cells were centrifuged at 5000 rpm for 5 min and supernatant LB media was discarded. The collected cells were resuspended and washed in ~1.5 ml 1x phosphate buffer saline (PBS) at least 3 times to eliminate the remaining ingredients of the LB media. Labeling of *E. coli* cells was done in two steps, as shown in Figure 4.6. In first step, ~3 x 10^9 cells/ml were incubated with FITC conjugated rabbit anti-*E. coli* Ab (AbD Serotech, NC) at 330 µg/ml for 1 hr at room temperature (RT). The cells were then subjected to pelleting with centrifugation (7000 rpm), and washing with PBS three times. In the

second step, *E. coli* cells were incubated with Alexa 555 conjugated goat anti-rabbit second Ab (Invitrogen, CA) at 130 µg/ml for 1 hr at RT. The labeled *E. coli* cells were pelleted and washed two times with 1x PBS followed by two times with DI water. The cells were finally resuspended in DI water to a desired concentration of ~1 x 10^9 cells/ml for the DEP experiments.

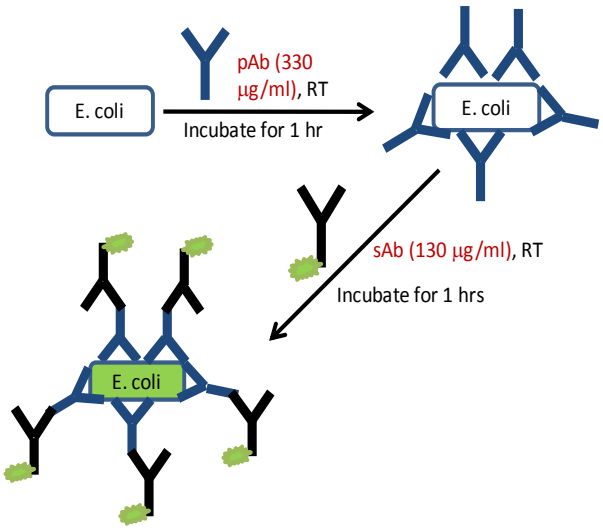

Figure 4.6 Schematic showing two stage labeling procedure of *E. coli* cells using primary antibody (pAb) and secondary antibody (sAb).

4.5.3 DEP capturing experimental details

An upright fluorescence optical microscope (Axioskop 2 FS plus; Carl Zeiss) in reflection mode was used for DEP experiments. The packed fluidic chip was placed under the 50X objective and focused at 200 µm x 200 µm active NE area through the transparent ITO-glass electrode. A filter set with excitation wavelength of 540-552 nm and emission wavelength of 567-647 nm (filter set 20HE, Carl Zeiss) was used in connection with an Axio Cam MRm digital camera to record fluorescence videos at an exposure time of 0.4 s using multi-dimensional acquisition mode in the Axio-vision 4.7.1 release software (Carl Zeiss MicroImaging, Inc). Before performing DEP experiments 1.0 ml BSA solution (2% w/v) was fed through the channel at a flow rate (Q) of 0.2 µl/min to passivate the surface of SU-8 and SiO_2 in the fluidic channel in order to prevent non-specific adsorption of *E. coli* cells. The channel was then washed with 2 ml DI water at a Q = 5.0 µl/min. Labeled *E. coli* suspension in DI water was injected into the channel. DEP experiments at different frequencies (f) of the sinusoidal AC voltage and at

different flow velocities of *E. coli* cells were performed. Each experiment was performed for a span of 30 sec during which no voltage (V_{off}) was applied in the initial ~10 sec, fixed AC voltage at different frequencies was applied (V_{on}) in the next ~10 sec, and no voltage was applied (V_{off}) in the last ~10 sec. Videos were recorded during each experiment. The response of *E. coli* cells was also visually monitored using microscope to determine the optimum frequency of the AC voltage for DEP capture of *E. coli* cells. DEP videos were later analyzed using Automeasure module in Axio vision software to quantify the capture of *E. coli* cells.

4.5.4 Impedance measurement after DEP capture

Electrochemical impedance spectroscopy (EIS) was measured in two-electrode setup before and after *E. coli* cells were captured dielectrophoretically with a potentiostat (PARSTAT 2273, Princeton Applied Research Corporation) with *E. coli* cells suspended in DI water filled between the CNF NEA and the ITO-glass electrode in the microfluidic channel. An AC voltage of 2.8 V_{pp} (peak-to-peak voltage) at the limit of the instrument was applied at the CNF NEA at the open-circuit potential vs. the ITO-glass electrode with the frequency uniformly spanned in the logarithm scale from 1 MHz to 100 mHz. The applied voltage amplitude is much larger than the value of 10-50 mV_{pp} used in conventional EIS measurements since our goal is at developing real-time impedance measurements in which the AC voltage serves both as the DEP driving force and the EIS probe. For capturing, *E. coli* cells were injected into the fluidic channel at a flow velocity of 0.11 mm/sec. The pDEP was applied for 5-10 seconds with an AC voltage of 10 V_{pp} using a wave function generator (Model 33120A, Hewlett Packard) at a fixed frequency of 100 kHz. After capturing enough *E. coli* cells, the flow was turned off while the AC voltage remained on for ~10 minutes. Sufficient number of *E. coli* cells were observed by fluorescence microscope to stick to the exposed tips of the CNF and remained stably attached after the AC voltage was turned off. The cell was then disconnected with the solution sealed in the channel by two inline valves and moved to the potentiostat for EIS measurements.

4.6 Results and Discussion

A critical factor for efficient cell trapping is the strength of F_{DEP} required to overcome the hydrodynamic drag force (F_{DRAG}) excerted on the cells by the fluidic flow which carries the cells moving downstream with fluid. F_{DRAG} could be considerably large at high flow velocities above 100 μm/s. The rationale behind the design of the DEP device is based on the results of DEP

modeling performed using two-dimensional (2D) finite element multiphysics software.[131] According to this study, higher trapping efficiencies are attained either by injecting the particles at a height less than 3 μm from the NEA or by applying a higher voltage bias 9 V_{pp}. Efficient capture was observed at a high flow velocity up to 2 mm/sec. In the same study, a comparison of ∇E^2 and magnitudes of F_{DRAG} and F_{DEP} for particles located at different heights in the channel was made. In the middle of the fluidic channel, the direction of F_{DEP} (namely the vector of ∇E^2) is mostly in vertical direction, which is perpendicular to F_{DRAG} by the fluidic flow.[131] As a result, even a small DEP force is sufficient to deflect the bacterial particles downward as they flow. But as the particle is moved closer to the NEA, a larger horizontal component in ∇E^2 starts to play a significant role which may exceed the horizontal drag force by the fluidic flow and retain the particles at the nanoelectrode site. In this study, the opposite vertical drag force as the particles are pulled down by the initial vertical DEP force F_{DRAG} is neglected since the vertical velocity is negligible comparing to the high lateral flow velocity of the fluid. It was found that, at a height of 2 μm, F_{DEP} is 3 orders of magnitude higher than the F_{DRAG} at a high flow velocity of 10 mm/sec. If a particle is injected at an optimum point above the NEA, high trapping efficiencies even at very high flow velocities can be achieved.

To achieve efficient bacterial capture at a selected location, a square area of 200 μm x 200 μm was opened in a thin SU-8 2002 coating on the NEA substrate which is limited at ~2 μm in thickness in this study. A microchannel of ~18 μm in height was patterned in the 18 μm thick SU-8 2010 layer on ITO-glass electrode. The height of the feature in the SU-8 films on the NEA and the ITO-glass were measured using Ambios Technology XP-2 profiler and was consistent with the design (see Appendix Figure B.2). A bright field image of the DEP device with the active NEA square at the bottom and a microchannel with the circular chamber in the SU-8 on the ITO-coated glass on top is shown in Figure 4.7a. The inset shows an enlarged crossectional schematic of the F_{DRAG} and F_{DEP} on a single *E. coli* cell as it is flowing through the mid of the channel above the active NEA square. A cross-sectional view of the structure of the DEP device is further schematically shown in Figure 4.7b. Fluid enters from one end and collected in a waste collector at the other end. The top-view SEM image of the surface of a CNF NEA is shown in Figure 4.7c, which indicates that the diameter of exposed CNFs is ~100 nm and the density of exposed CNFs is ~2×10^7 CNFs/cm^2 with an average spacing of ~2.0 μm. At such low density,

the exposed CNF tips are well separated from each other and each is expected to behave same as a single NE.

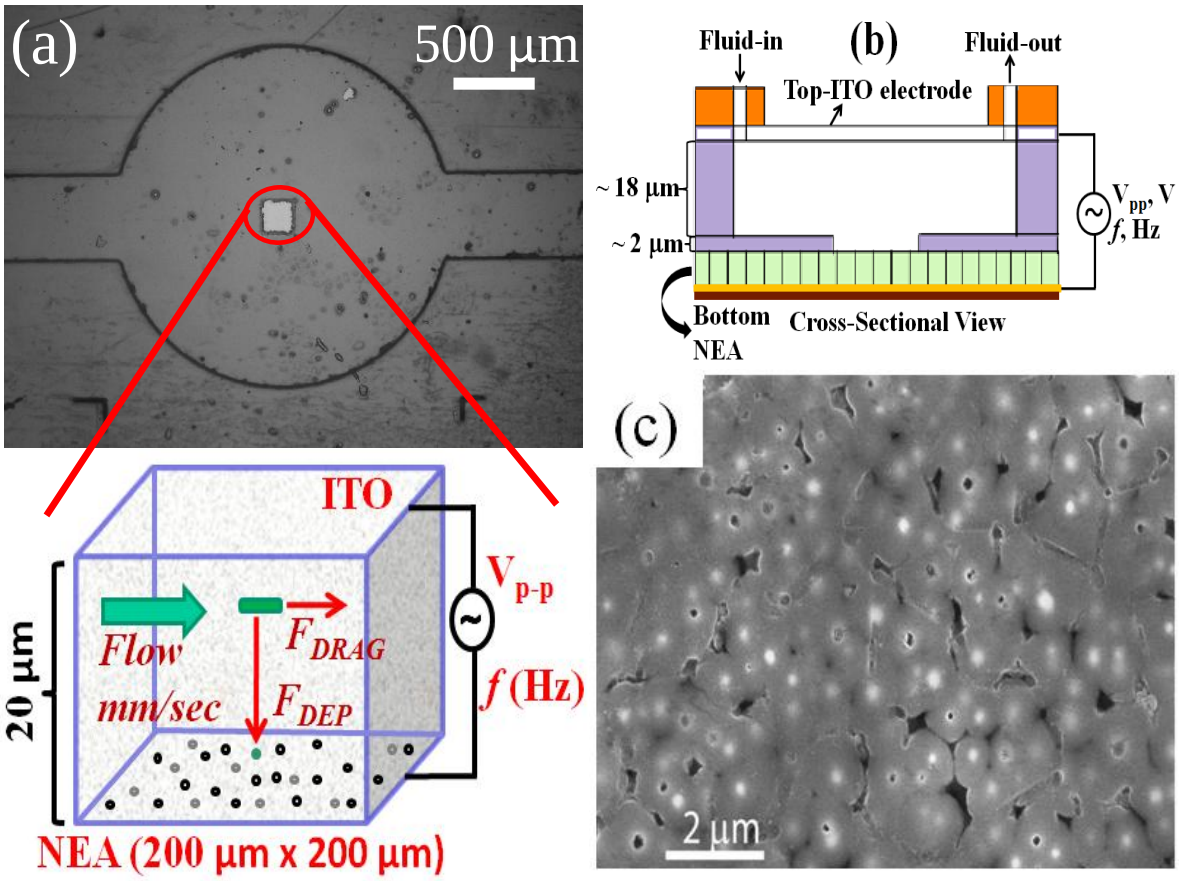

Figure 4.7 Design of nano-DEP device. (a) A brightfield image taken using an upright optical microscope (4x objective) in reflection mode of a DEP device. The small square (200 µm x 200 µm) at the center is the exposed active CNF NEA placed at the bottom. A 500 µm wide microchannel with a 2 mm diameter chamber is patterned on an ITO-glass electrode which is flipped upside down, placed on top CNF NEA, and aligned to the center of the square. The inset beneath shows the enlarged schematic of an *E. coli* cell influenced by the major forces when it flow through the channel between the two electrodes where a AC voltage is applied. The total height of the channel is 20 µm. (b) A cross-sectional schematic view of the nano-DEP-device. (c) A scanning electron microscopy image (top view) of the CNF NEA showing exposed CNF tips.

The captured *E. coli* cells at each exposed CNF tip appear as round bright spots as shown in the enlarged schematic of the device in Figure 4.7a. As the AC voltage is turned-off the captured *E. coli* cells are released and pushed away from the exposed tips by the hydrodynamic drag force F_{DRAG} from the fluidic flow. To stably capture the cells, the F_{DEP} has to somehow overcome F_{DRAG} acting on an *E. coli* cell. When an AC voltage of proper frequency is applied to the CNF NEA, *E. coli* cells will be pulled by the pDEP force (F_{DEP}) toward the exposed tips of NEA and remain captured as long as the AC voltage is on. DEP capture experiments at various AC frequencies (50 kHz to 1 MHz) at fixed AC amplitude of 10 V_{pp} were first carried out. The number of captured *E. coli* cells is quantified by counting the number of individual fixed bright spots using Automeasure module of the microscope software. Figure 4.8 shows a plot of number of bright spots at different frequencies of the AC voltage. It can be observed that there is least number (~30) of bright spots at 1 MHz frequency whereas the count was maximum (~300) at 100 kHz, indicating more *E. coli* cells being captured at the NEA. Clearly, 100 kHz gives the best capture efficiency for pDEP capture of *E. coli* cells. Thus the 1 MHz AC voltage used in the previous study[131] was too high and far from the optimum condition.

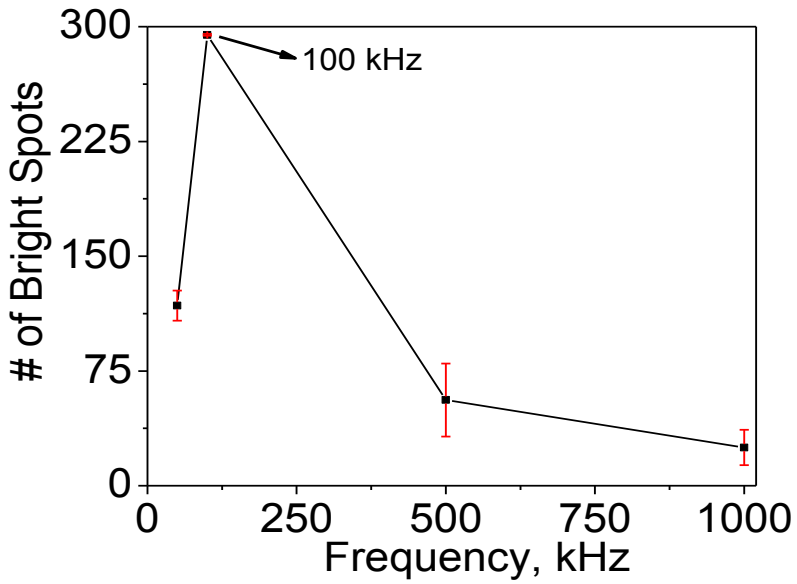

Figure 4.8 The number of bright spots count in each pDEP experiment vs. the frequency of the applied AC voltage. All experiments use an AC voltage bias of 10 V_{pp}. The maximum trapping efficiency is obtained at 100 kHz.

The conductivity of the solution suspended with ~1 x 10^9 cells/ml is 6.74 μS/cm, only ~3.5 times higher than the value of 1.9 μS/cm for ultrapure DI water. Using the value of 6.74 μS/cm for the suspending medium, the dependence of CM factor on the frequency of the AC voltage was studied, with all other parameter same as discussed above in section 4.4. As seen in Figure 4.9, at all frequencies below ~10^7 Hz, *E. coli* cells are expected to experience approximately same DEP force. At higher frequencies (>10^8 Hz), CM factor becomes negatives indicating that *E. coli* cells will experience nDEP. The variation of the CM factor vs. frequency between the theoretical calculation and experimental observation of *E. coli* cell capture (as shown in Figure 4.8) is not consistent at this stage. One possibility could be due to the attachment of antibodies on the surface of *E. coli* cells, causing a thicker protein cell wall. However, increasing the thickness of cell wall by ~20 nm does not show any change in the calculated CM factor (red curve in Figure 4.9). On the other hand, from theoretical calculations (see Figure 4.5), we know that at high medium conductivities, CM factor can flip from positive to negative as the frequency is lowered. There might be some error when conductivity measurements were done or if any residual salts left due to PBS buffer in the channel might change the local conductivity, which leads to the difference in theoretical calculation and experimental observations. This needs to be carefully investigated in details in future studies.

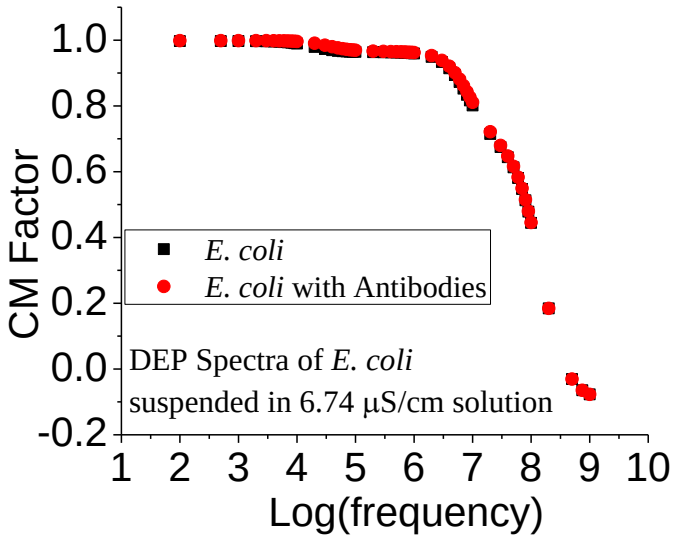

Figure 4.9 Calculated CM factor of *E. coli* cells suspended in a medium with the conductivity of 6.74 μS/cm.

We then carried out pDEP capture experiments with AC voltage fixed at the frequency of 100 kHz while sequentially increasing the flow velocity of *E. coli* cells from 0.11 mm/sec to 1.6 mm/sec. The flow velocities referred in this paper is the linear flow velocities at the 200 μm x 200 μm NEA area calculated from the recorded videos (see supplementary videos files for details). Before performing DEP capture experiments, *E. coli* cells at a particular flow velocity were flowed through the channel for sufficient time to get rid of air bubbles and other particles to attain a uniform and stable flow. Figure 4.10a shows snap shot of the video as *E. coli* cells are flowing at 0.11 mm/sec through the channel when the voltage is turned off, where each cell appears as a stretched line. Green pseudocolor is used to represent the fluorescence emission.

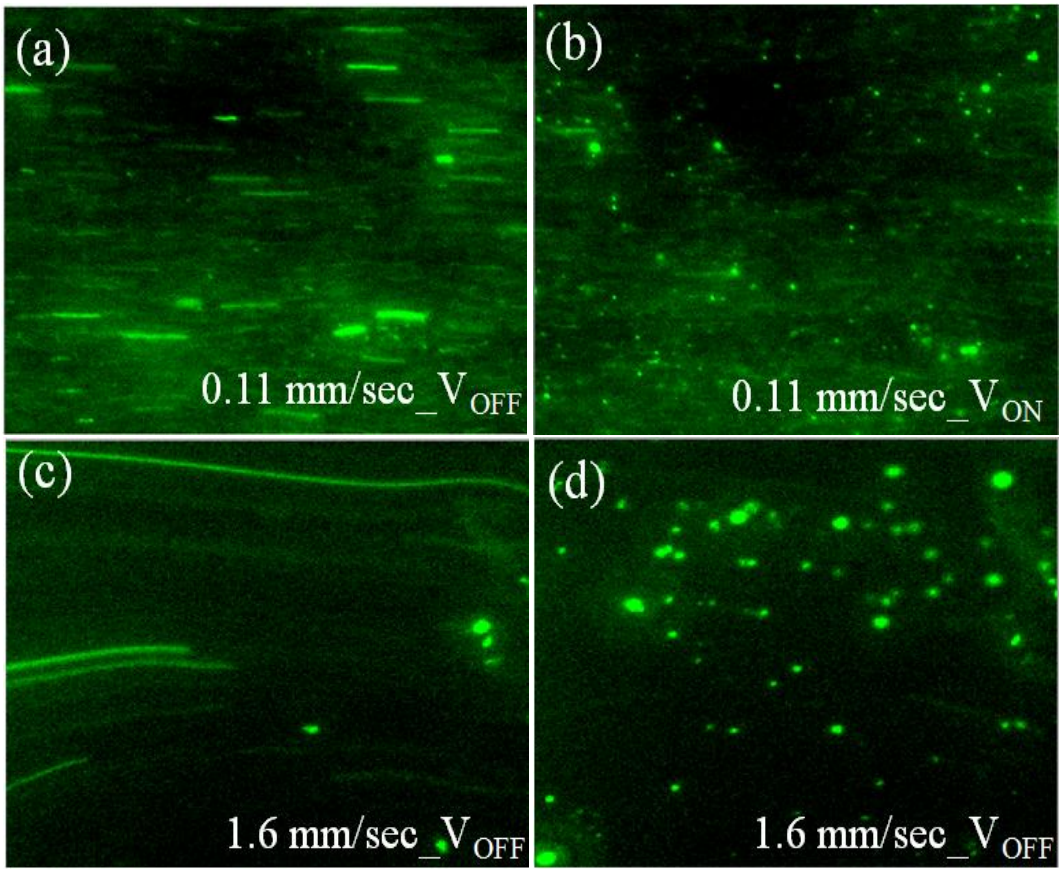

Figure 4.10 Images of *E. coli* cells before and after being captured at the CNF NEA with 100 kHz frequency and 10 V_{pp} AC bias. (a) and (c) Snap shots of *E. coli* cells flowing at 0.11 and 1.6 mm/sec flow velocities, respectively, in the DEP device when no voltage is applied. (b) and (d) Snap shots of *E. coli* cells captured at the exposed tips of CNF NEA by applying an AC voltage of 10 V_{pp} at 0.11 and 1.6 mm/sec flow velocities, respectively.

Almost immediately after the voltage is turned on, the stretched lines turn into bright round green spots at fixed positions as shown in Figure 4.10b, indicating that *E. coli* cells are captured at the tips of CNF NEA by pDEP. When the flow velocity is increased, *E. coli* cells experience a larger F_{DRAG} since F_{DRAG} is proportional to the flow velocity. As a result, less *E. coli* cells can be stably captured. Figure 4.10c shows a snap shot from a video of *E. coli* cells flowing at a flow velocity of 1.6 mm/sec when the voltage is turned-off. *E. coli* cells appear as much longer stretched lines due to the higher flow velocity as compared to that in Figure 4.10a. When the voltage is turned on, substantial number of *E. coli* cells are captured by pDEP at the NE tips as seen in Figure 4.10d. This indicates that the pDEP force is sufficient to attract many cells (likely those that are closer to the bottom NEA surface) toward the NEA. Once they are at the CNF tip, the lateral DEP force component is larger than the hydrodynamic drag force along the flow direction even at a high flow velocity of 1.6 mm/sec and thus is able to keep the *E. coli* cell at the surface.

Further analysis was carried out to show the capture kinetics at three different flow velocities. The number of bright spots at each time frame was counted during DEP capture experiments and plotted vs. time in Figure 4.11a. At the initial conditions at all three flow velocities almost no *E. coli* cell is trapped when no AC voltage is applied, the moment an AC voltage is applied, a sudden increase in the count of bright spots is seen, indicating the capture of *E. coli* cells at the NEA. The count remains almost the same during the time the voltage is applied. But the number of the bright spots clearly depends on the flow velocity. At a low flow velocity of 0.11 mm/sec, the count of bright spots is ~300 while it sharply drops to ~70 as the flow velocity is increased to 1.6 mm/sec. More details of the kinetic process to capture *E. coli* cells can be seen in real-time DEP videos at 0.11 mm/sec and 1.6 mm/sec flow velocities in supplementary videos. The flow velocity at 1.6 mm/sec is ~3 times higher than the maximum flow velocity of 0.5 mm/sec that is reported for a micro-points-and-lid device[155] and is at the high end of the typical range of the flow velocity (0.04-2 mm/sec) used in interdigitated micro-DEP device.[167]

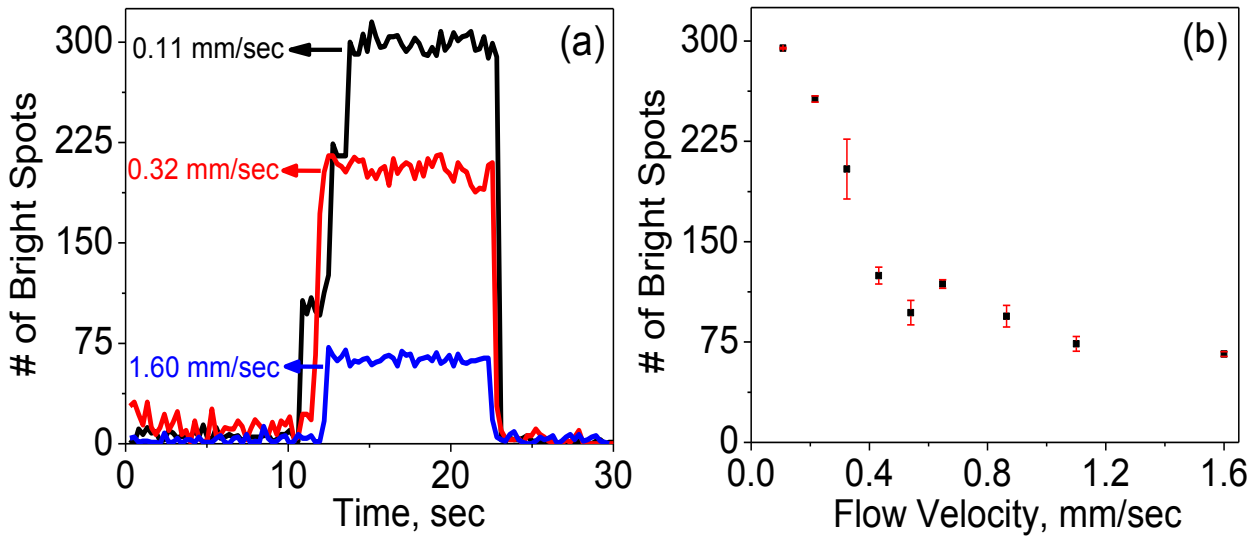

Figure 4.11 Quantifying *E. coli* cells captured at different flow velocities. (a) The change in number of captured *E. coli* cells (correlated to the number of bright spots counted) with respect to time at three different flow velocities (0.11, 0.32 and 1.6 mm/sec). DEP capture experiments are performed by applying an AC voltage of 10 V_{pp} at a frequency of 100 kHz. (b) The change in number of bright spots as a function of flow velocity as *E. coli* cells are flowing through the channel.

For stable capture of a particle, two sequential processes are involved. First, a vertical DEP force has to be strong to be able to quickly pull the particle to the NEA tip before it flows out of the active area. Second, the lateral DEP force F_{DEP} at the NEA tip has to overcome the lateral drag force F_{DRAG} by the lateral fluidic flow which depends on the flow velocity. The hydrodynamic drag force by the fluid to carry the particles with the flow in a microfluidic channel is defined by Stokes equation:[167]

$$F_{drag} = 6\pi k r \eta \upsilon_m \quad \textbf{(4.3)}$$

where η is the dynamic viscosity of the fluid, υ_m is the velocity of the medium fluid at the center of the particle, and k (>1) is a nondimensional factor accounting for the wall effects. It should be noted that the value of υ_m is height-dependent since the fluid follows in a parabolic laminar flow profile with the highest velocity at the center and slowest velocity at the channel walls. In our results reported in this work, the flow velocity is calculated from the length of stretched lines in

the videos focused on the CNF NEA surface at the bottom of the microchannel, and thus it is the actual υ_m within the depth of field of the camera (~0.6 μm by the tutorial calculator at Carl Zeiss website) from the CNF NEA surface. The average flow velocity $<\upsilon_m>$ is ~2.78 mm/sec (see Appendix B), much higher than 2.0 mm/s used in the previous study.[131] From Equation 4.3, increasing the flow velocity clearly does not favor pDEP capture of the bacterial cells. However, many practical applications require rapidly isolating bacterial cells from a dilute solution, in which a high flow rate has to be used to obtain sufficient throughput. It has been very challenging to use pDEP for such applications. The pDEP force has to be increased to compete with the increased drag force. According to the DEP modeling study published earlier,[131] the square of the electric field strength at the NE tip is 200 times higher than that of the micro electrodes used in points-and-lid configuration. This provides a very high DEP force required to counteract the large drag force and capture *E. coli* stably at the CNF NEA. However, the experiments were carried out only at two average flow velocities, i.e. 0.25 mm/sec and 2.0 mm/sec. Here we show the systematic study at a series of surface flow velocities from 0.11 mm/sec to 1.6 mm/sec. It is convincing that pDEP capture of *E. coli* cells is effective at the flow velocity of 1.6 mm/sec or even higher.

The kinetic profiles of the fluorescent spots vs. time during pDEP capture of *E. coli* cells in our study can be interestingly compared with those in the previous study by Arumugam et al.[131] They found that, at low AC voltage amplitude (1-7 V_{pp}), there was a slow kinetic process which took seconds for the fluorescence intensity of captured *E. coli* cells to reach the saturated level. But it almost immediately jumped to the saturated level at a high AC voltage of 9 V_{pp}. The fast kinetic phenomena at 9 V_{pp} is consistent with our results in Figure 4.11a, all of which were measured at 10 V_{pp} AC bias. Interestingly, although the saturated level of the fluorescence counts varies with the flow velocity, none of the curves shows the slow kinetic process during which bacterial cells slowly accumulates when the AC voltage is turned on. It seems that pDEP action is accomplished instantaneously even at the highest flow velocity. The saturated level of the captured fluorescent spots is plotted vs. the flow velocity in Figure 4.11b. A monotonically decreasing curve is obtained as the flow velocity is increased. The trend is consistent with our discussion above.

Our long-term goal is to develop this technique as a rapid pathogen detection technique using handheld electronics. The fluorescence measurement needs to be replaced with simpler

electronic methods for detection. Impedance biosensors integrated with techniques like DEP, termed as DEPIM, are widely employed for rapid detection of pathogenic bacteria. DEPIM has been demonstrated to monitor the processes utilizing pDEP force to capture bioparticles on the electrode surface at a fixed AC frequency using real-time impedance measurements.[70] It can detect pathogenic bacteria both quantitatively and selectively at IDEs where the bacteria are trapped in between the electrode pair in a pearl chain fashion and the conductance change between the electrodes was monitored.[168-169]

To explore the feasibility of DEPIM with CNF NEAs, we carried out EIS measurements with 2.8 V_{pp} AC voltage bias before and after pDEP capture of *E. coli* cells. The Bode plots of EIS are shown in Figure 4.12. Figure 4.12a shows the |Z| value over the whole frequency range after pDEP performed at 10 V_{pp} in comparison with that without subjected to pDEP capture. Clear differences can be seen at frequencies below 100 Hz.

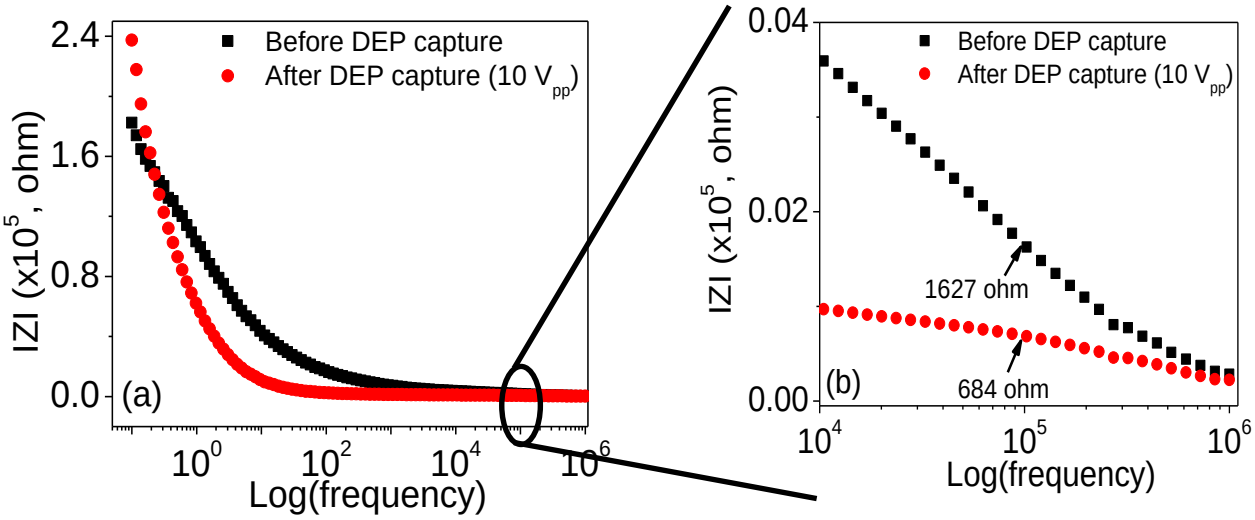

Figure 4.12 Variation of the electrochemical impedance spectroscopy (EIS) before and after bacterial cell capture. (a) The Bode plot of the EIS, that is the amplitude of |Z| vs. the logarithm of the AC frequency, recorded in an *E. coli* cell suspension in DI water before and after subjected to DEP capture at the exposed CNF tips by applying an AC potential of 10 V_{pp} at 100 kHz frequency. (b) An enlarged portion of the Bode plot to show impedance change at the frequency around 100 kHz in an *E. coli* cell suspension before and after subjected to DEP capture at the CNF NEA.

The enlarged plot in Figure 4.12b shows that, percentage of the change in the |Z| value at 100 kHz (the optimum pDEP frequency) is as large as that at low frequencies. The |Z| value of CNF NEA in *E. coli* suspension at 100 kHz is ~1627 Ω before pDEP bacterial capture. After running pDEP experiments to capture *E. coli* cells, the |Z| value decreases to ~684 Ω (by ~58%). The arrows in Figure 4.12b indicate the |Z| values at 100 kHz. Thus the decrease in the impedance may be likely because the large (1-2 μm in size) and more conductive bacterial cells that are in direct contact with the small CNF tips (~100 nm in dia.) which is equivalent to increasing the electrode size. The results in this study serve as a reference of the maximum change that one can obtain to reach the saturated bacterial capture.

4.7 Conclusions

In summary, a brief theory behind the concept of dielectrophoresis was presented. Multi-shell smeared-out model can be readily used for the prediction of effective permittivity and CM factors for complex bioparticles like *E. coli* cells and vaccina virus. Then a theoretical prediction of CM factor and DEP force at different medium conductivities for *E. coli* and vaccine virus was discussed. We demonstrated effective pDEP based capture of *E. coli* cells from a high-velocity flow at the exposed tips of an embedded CNF NEA. The CNF NEA is placed at the bottom of a microfluidic channel vs. a large transparent ITO-coated glass at the top with 20 μm spacing in between to form a "points-and-lid" configuration. Our results have confirmed the observations in a previous report using such nano-DEP device. More importantly, we found that the optimum frequency of the AC voltage is around 100 Hz, much lower than 1 MHz used in the previous study. *E. coli* cells can be captured in a selected area by lithographically defining a window on the CNF NEA chip. The total quantity of captured *E. coli* cells is found to decrease monotonically as the flow velocity is increased. Interestingly, the fluorescence signal representing the captured *E. coli* cells immediately jumps to the saturated level at all flow velocities once a 10 V_{pp} AC bias is applied. No kinetic accumulation is observed at such a high-voltage bias. EIS before and after capturing *E. coli* cells show clear changes over the whole frequency range. Particularly, the |Z| value at 100 kHz (i.e. the optimum pDEP operation condition) is decreased by ~58% after cell capture. Therefore, it is highly feasible in future studies to use real-time impedance (i.e. DEPIM) for directly monitoring the process during pDEP capture of bacterial cells.

Chapter 5 - Luminol Decorated Gold Nanoparticles (GNPs) as a Sensitive Chemiluminescence (CL) Biosensor for Trace Blood Detection

Provision patent No. 61/595,958 (A Nanoparticle-functionalized Chemiluminescent Method for Biosensing, by Lateef U. Syed, Jun Li, Judy Wu, and Mark Richter) was filed on Feb. 7th, 2012.

Reproduced partly from "An Ultrasensitive Chemiluminescence Method for Trace Blood Detection Using Luminol-Labeled Gold Nanoparticles" Syed. L. U.; Rochford. C.; Wang. F.; Wu. J.; Richter. M.; Balivada. S.; Troyer. D.; Li. J. manuscript in preparation.

5.1 Introduction

CL is a process in which visible light is emitted as a result of chemical reactions. CL is a much more sensitive and convenient analytical technique than commonly used fluorescence methods due to high quantum yield, no need of exciting light sources, and low background.[170] It has been widely utilized for forensic investigations by spraying luminol (5-amino-2,3-dihydro-1,4-phthalazine-dione) and hydrogen peroxide to identify dried blood stains.[171-172] CL catalyzed by luciferase is also used in pyrosequencing, one of the most successful DNA sequencing techniques.[172] In this chapter, we will discuss our study to improve luminol based CL by covalently attaching luminol molecules onto gold nanoparticles (GNPs) that are protected by a monolayer of carboxylic acid terminated alkane thiols. Using GNPs as high-surface carriers, manipulation and binding of luminol moieties to desired locations were made easier. In addition, the absorption or colorimetry of GNPs may serve as an additional signal modal for analytical measurements.

GNPs have gained considerable attention in the past few decades due to their unparalleled optical, electronic, physical, and chemical properties.[173-175] The ease of surface modification of GNPs with alkane thiol molecules[176-179] and further covalent linking with other biological moieties makes GNPs an attractive choice for biosensor applications. Modifying GNPs with a particular DNA probe or an antibody has become a common practice for developing affinity based biosensors. In addition, GNPs present strong size-dependant surface

plasmon resonance. This makes them ideal sensors for colorimetric or absorption detection of DNA, amino acids, and proteins, by specific binding with another recognition element in bulk solution or immobilized on a substrate.[77-78, 80, 180-183] The detection limit for nucleic acids based on GNP aggregation varies in a large range, with the lowest reported at ~33 zmol ($2.0x10^4$ target molecules).[184] The GNPs in such detection may be much more than target molecules. Here, we demonstrate that CL from luminol molecules carried by GNPs can be detected with as low as ~1,000 GNPs.

Luminol belongs to the family of heterocyclic hydrazide compounds, and is by far one of the most popular agents for CL applications.[185-188] The concept of light production by luminol catalyzed by Fe^{3+} ions released from red blood cells is the basis of forensic and hospital analysis of blood contamination.[30, 171, 189] When GNPs are added to a solution containing luminol and ferricyanide ($Fe(CN)_6^{3-}$), they may inhibit the CL signal of luminol due to quenching if the diameter is less than 5 nm or enhance it due to catalytic effects if d is ~25-38 nm).[190-191] The effect of GNPs was found to be minimum with 5-10 nm diameter.[190-191] However, in one study, CL signal was reduced by ~5.0 fold with luminol covalently attached to 30 nm GNPs compared to that in solution.[192] The mechanism of these effects remains to be understood.

In general, electron transfer may facilitate catalytic effects while energy transfer to GNPs may cause nonradiative deactivation (quenching) of chemically excited luminol products. To avoid the complication, we chose to use 10 nm-diameter GNPs in this study, where GNPs only serve as nanocarriers with a large surface-to-volume ratio for ease of manipulation of luminol molecules. In addition, the surface of GNPs is protected with a close-packed self-assembled monolayer of long-chain thiol linker, mercaptoundecanoic acid (MUA), to minimize both electron transfer and energy transfer between luminol and the GNP. This allows us to assess whether the surface-functionalized luminol can generate CL as efficiently as in bulk solution, which was an issue in previous studies.[192-193] Using this design, we have observed very strong CL from luminol-attached GNPs and found that the CL intensity increased linearly on the logarithmic scale with the number of GNPs over 7 orders of magnitude. We measured CL with as small as ~1,000 luminol-labeled GNPs. Using this method, we were able to detect sheep blood samples after 10^8 fold dilution from the stock solution.

5.2 Experimental details

5.2.1 Materials and reagents

Citrate protected GNPs (8.0-12.0 nm in diameter), and mercaptoundecanoic acid (MUA) were purchased from Sigma Aldrich. Luminol (LUM), EDC, NHS, Tween 20, potassium ferricyanide ($K_3Fe(CN)_6$), PBS, sodium hydroxide (NaOH), and hydrogen peroxide (H_2O_2) were obtained from Fisher Scientific. Polydimethylsiloxane (PDMS) was ordered from Dow Corning. All chemicals used in this study were analytical grade. DI water was used in all the experiments.

5.2.2 Multiwell fabrication for blood experiments

A polydimethylsiloxane (PDMS) test strip ~1 mm thick was fabricated on a glass slide using a fixture shown in Figure C.1a. A 20:1 ratio of PDMS and curing agent respectively was mixed and cured at ~60 ^{o}C for 20 min. An array of oval shaped holes (~4 mm x 3 mm) was punched through the PDMS that can hold ~12 μl volume of solution for CL experiments.

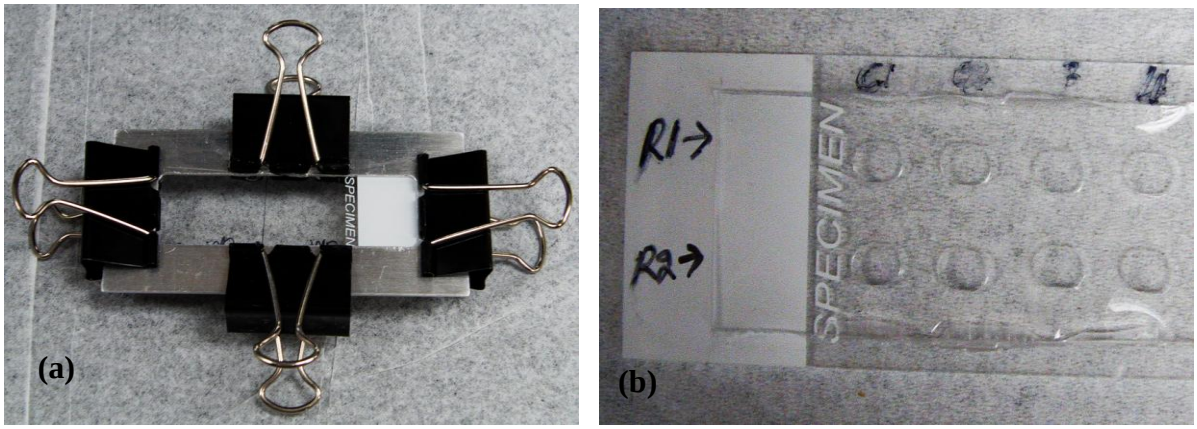

Figure 5.1 (a) Fixture used to fabricate PDMS test strip for chemiluminescence experiments. (b) Test strip with holes punched in the PDMS.

5.2.3 Blood sample preparation

Whole sheep blood was obtained from HemoStat Laboratories (Dixon, CA). The concentration of the sheep red blood cells in the stock blood solution was measured as ~$4.6x10^9$ cells/ml using Petroff Hausser counting chamber under an upright optical microscope (AxioSkop II, Carl Zeiss), as shown in optical image (Figure 5.2a). The received blood sample was stored at

~4^{o}C. Before CL experiments, the sample was inspected under an optical microscope, to make sure that the cells were intact. In the experiments using lysed cells, 100 μL blood samples were frozen at -20^{o}C and thawed on ice before use. This resulted in complete cell lysis (see Figure 5.2b). Also, UV-Visible study of lysed and unlysed RBCs was done, which further confirmed that the freeze-thaw of RBCs indeed lyse them (see Appendix Figure C.1)

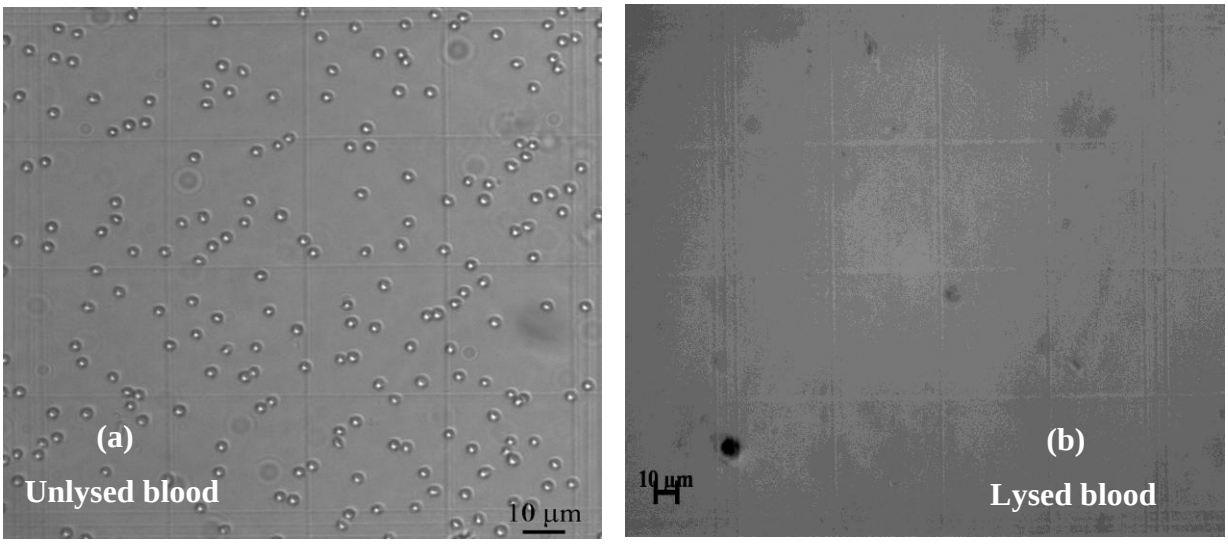

Figure 5.2 (a) Bright field image of unlysed 10X diluted sheep blood on a Petroff-Hausser counting chamber. The RBCs are ~3-4 μm in size. (b) Bright field image after lysing RBCs using freeze-thaw method.

5.2.4 Characterization instruments

UV-visible absorption spectra were recorded using Beckman DU640 spectrophotometer in a 360 μL microcuvette with an optical path length of 10.0 mm. Infrared spectroscopy (IR) was performed on a Nicolet 380 FT-IR spectrophotometer with neat solid samples in transmission mode. Transmission electron microscopy (TEM) measurements were carried out using FEI Tecnai F20 XT field emission system.

5.2.5 Modification of GNPs with chemiluminescent luminol

The initial step was to exchange the citrate groups with the MUA ligand on the surface of GNPs under the protection of the nonionic surfactant Tween-20. Typically, 2 ml of citrate-protected GNP stock solution (5.99×10^{11} particles/ml) was transferred in a clean, dry test tube

with a screw-cap followed by addition of 2 ml of 1X PBS with 0.2 mg/ml Tween-20 buffer (the same buffer composition was used for all following steps during functionalization). The mixed solution was incubated at room temperature (RT) for 30 min before 2 ml of 3.0 mM MUA solution (in 1:3 ethanol/DI water) was added. The solution was further incubated overnight at RT with gentle shaking. The mixture was centrifuged at 14,100 rpm for 20 min to pellet the MUA-covered GNPs (GNP-MUA). The supernatant was discarded and the pellet was re-suspended in the buffer. The pellet was washed three more times before the final suspension in the buffer. MUA modified GNPs (200 µl) were then reacted with 100 µl of freshly prepared aqueous solution of 50 mM EDC and 50 mM NHS for 15 min. This mixture was then combined with 100 µl of 50 mM LUM solution (a few drops of 0.4 M NaOH were added to increase the solubility of LUM in DI water) and incubated at RT for 2 h. Finally, the LUM-modified GNPs (GNP-MUA-LUM) were washed 3 times with buffer and finally suspended in the buffer solution to obtain a final concentration of ~$1x10^{12}$ GNP/ml.

5.2.6 CL measurement

CL experiments were carried out using a IVIS Lumina II system (Caliper Life Sciences, CA), which utilizes a highly sensitive, -90^{o}C cooled, and back illuminated CCD camera as the detector. A layer of PDMS of ~1.5 mm in thickness was laid on a glass microscope slide (3" x 1" x 1 mm) in which an array of oval shaped holes (3 mm x 4 mm) was punched through to form CL reaction wells of ~12 µl in volume. The GNP-MUA-LUM solution was dropped in the well and dried before CL measurements. Each well contained a known number of luminol modified GNPs. Typical CL experiments involved mixing 4 µl of 0.033 M NaOH, 4 µl of 0.47 M H_2O_2, and 4 µl of 1 mM $Fe(CN)_6^{3-}$ solution or, in some experiments, blood samples (at varied concentrations) in different PDMS wells. The slide was then quickly placed in the light tight black box of the IVIS Lumina II system. A bright field reference photograph was first recorded using the CCD camera (this process takes ~3 sec), and then the CL signal (Photon flux) was recorded in the kinetic mode (i.e. flux of photons vs. time) with an exposure time of 10 sec to the CCD camera. The CL signal is represented in a pseudocolor image by overlaying the bright-field and CL images. The elapse between consecutive CL snap shots in the kinetic mode is approximately 13 sec (i.e. 3 sec for reference photograph, and 10 sec to collect CL signal).

Normally, 10 such CL snapshot images were taken and the integrated photon flux over the designated PDMS well was plotted vs. time.

5.3 Results and discussion

5.3.1 GNPs modification and characterization

The two-step strategy to functionalize luminol on GNPs and the scheme of using such functionalized GNPs for detecting Fe^{3+} containing analytes are illustrated in Figure 5.3. In the first step, the citrate ligand, which was used to stabilize GNP colloid in the starting material, was replaced with MUA by ligand exchange. This process produced a self-assembled monolayer of MUA on each GNP through stronger Au-thiol interaction, yielding carboxylic acid (-COOH) terminal groups at the exterior surface. In the second step, the MUA derivatized GNP colloid was reacted with luminol in the presence of EDC and NHS, which facilitated the covalent binding of luminol onto the GNPs via an amide bond formed between the -COOH group of MUA and the $–NH_2$ group of luminol.

The product is labeled as *compound A* (i.e. GNP-MUA-LUM) in Figure 5.3. UV-vis, IR, and HRTEM measurements were employed at each stage of modification to confirm physical and chemical changes occurring at the surface of the GNPs.

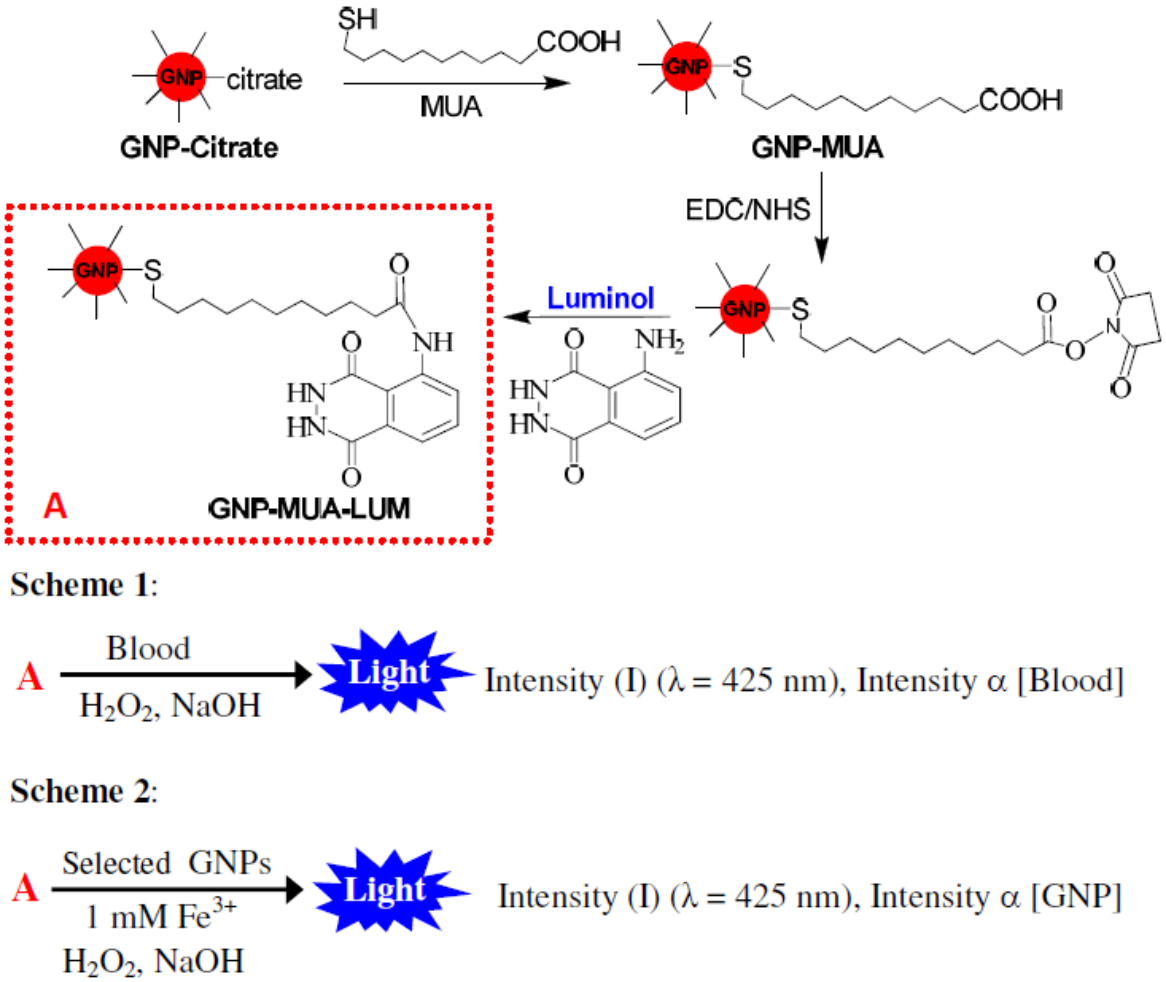

Figure 5.3 Schematic of the two-step modification of gold nanoparticles (GNPs) with luminol (LUM): ligand exchange of citrate with mercaptoundecanoic acid (MUA) and amide formation between the –COOH group in MUA and $–NH_2$ group in LUM. Two schemes to implement luminol-labeled GNPs (compound A) for analytical applications are illustrated: Scheme 1– to detect analytes (such as red blood cells) which can catalyze the CL reaction in presence of sufficient amount of A and required reagents (H_2O_2 and NaOH); Scheme 2 – to detect selected amount of A by supplying sufficient Fe^{3+} catalyst and required reagents (H_2O_2 and NaOH).

5.3.1.1 UV-visible absorption characterization of modified GNPs

The UV-visible absorption spectra in Figure 5.4 show the GNPs with different functional moieties at each stage, i.e. GNP-citrate, GNP-MUA, and GNP-MUA-LUM. Strong absorption

peaks were observed for all GNPs at ~516 nm, corresponding to the SPR. The full-width-half-maximum in the case of GNP-MUA and GNP-MUA-LUM is slightly larger than that of the GNP-Citrate. But the wavelength at the peak absorption of the GNP solution remains the same (as indicated by the deep red color shown in inset of Figure 5.4). These data indicate that the particle size remains similar as it goes through the ligand exchange and luminol functionalization processes. For GNP-MUA-LUM, however, there is an additional small, but noticeable peak at 347 nm, which corresponds to one of the absorption peaks of the luminol. UV-Visible absorption spectrum of pure luminol is shown in Appendix Figure C.2.

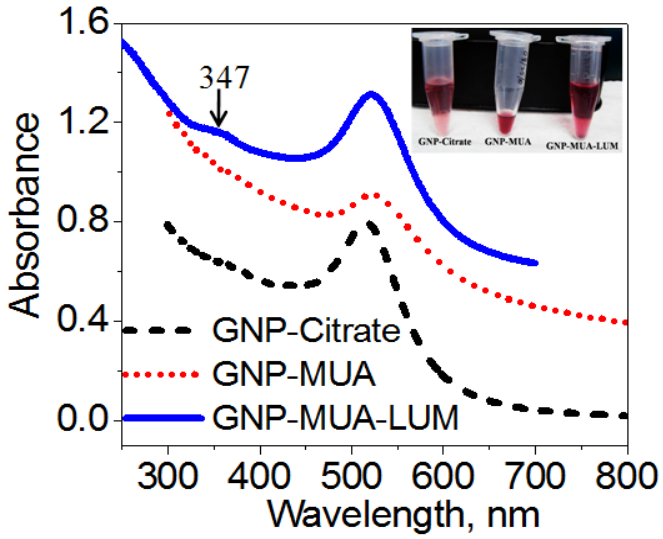

Figure 5.4 UV-visible spectra of citrate-stabilized GNPs (big dots), MUA modified GNPs i.e. after replacing citrate with MUA (small dots), and LUM attached GNPs (solid line). The small peak at 347 nm in the solid curve corresponds to an absorption peak of LUM. The GNP-MUA and GNP-MUA-LUM curves were translated upward by 0.2 and 0.5 units, respectively, along the y-axis for better comparison.

5.3.1.2 TEM characterization of modified GNPs

TEM images shown in Figure 5.3 further confirm that the shape and size of the GNPs before and after the modification have not been altered.

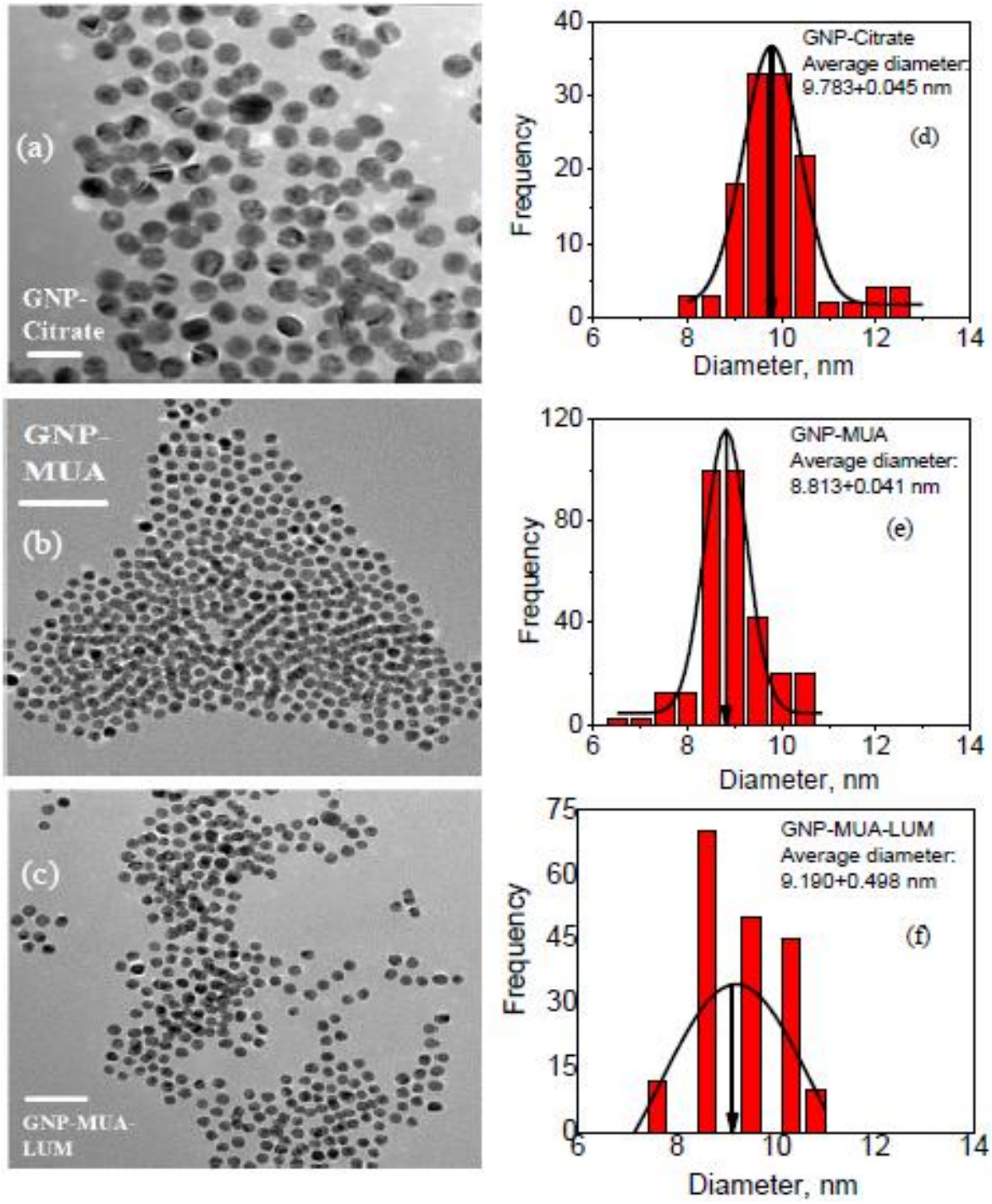

Figure 5.5 TEM images of GNPs with citrate protection (a), after MUA exchange (b), and luminol functionalization (c). The scale bars for (a)-(c) is 20, 50, and 50 nm, respectively. (d)-(f) show the size distribution of GNPs in (a)-(c). The average diameter of citrate stabilized, MUA exchanged, and luminol modified GNPs is ~9.8, ~8.8, and ~9.2 nm, respectively.

The average diameter of citrate-stabilized GNPs was found to be ~9.78 ±0.05 nm, in good agreement with the average size of 10 nm and a range distribution between 8.0 and 12.0 nm as certified by the vendor. After ligand exchange and luminol functionalization, the measured size of GNPs changed to ~8.81±0.04 nm and ~9.2±0.5 nm, respectively, within the size range of 8.0-12.0 nm, and no noticeable aggregation was observed.

5.3.1.3 FT-IR absorption characterization of modified GNPs

After ligand exchange and luminol functionalization steps, the GNP samples (including the starting GNP-citrate) were dried at room temperature and characterized with FT-IR. Figure 5.6 shows the FT-IR spectra of neat solid GNPs at different steps of functionalization. For MUA modified GNPs, the characteristic IR absorption peaks can be clearly seen at 2919 and 2849 cm^{-1}, which can be ascribed to the vibrational stretches of $–CH_2–$ functional groups in the MUA chain.[194] A peak corresponding to the C=O stretch in the terminal carboxylic acid group of MUA is expected at ~1700 cm^{-1}, but it was shifted to ~1550 to 1610 cm^{-1} for GNP-MUA and split between 1600 to 1730 cm^{-1} for GNP-MUA-LUM. This indicates that the carboxylic acid group in GNP-MUA presents in the ionized form (i.e. as carboxylate salts)[195] since the pH value of the suspension solution is ~7, above the pKa of general –COOH groups. The IR absorption at 1600 to 1730 cm^{-1} in GNP-MUA-LUM is consistent with the formation of amide bonds between the –COOH group in MUA and the $–NH_2$ group in luminol.[196] Also, a peak at 1396 cm^{-1} corresponding to the bending of C-H bond in the long alkane chain can be seen in GNP-MUA. The peaks corresponding to the C-H stretch of $–CH_2–$ in the alkane chain were observed at 2913 and 2864 cm^{-1} in GNP-MUA-LUM, confirming that the MUA monolayer was intact after LUM functionalization. The N-H stretch mode of luminol, which is expected to be at 3,300 to 3,500 cm^{-1}, however, was buried under the strong background absorption by GNPs. Overall, the FTIR spectra confirmed that the ligand exchange to replace citrate with MUA and functionalization of LUM to MUA were successful following the schemes shown in Figure 5.3.

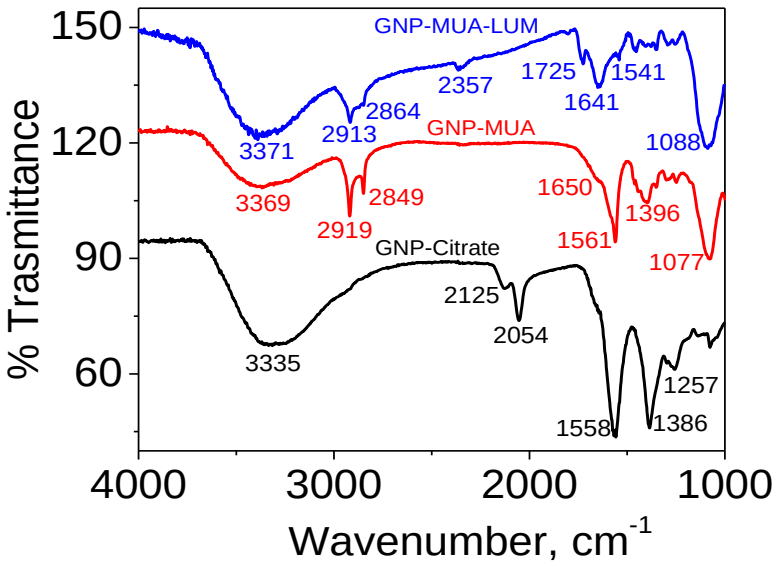

Figure 5.6 FT-IR spectra of citrate-stabilized GNPs (black curve), MUA modified GNPs after replacing citrate (red curve), and LUM attached GNPs (blue curve). The GNP-MUA and GNP-MUA-LUM curves were translated upward by 20 and 50 units, respectively, along y-axis for better presentation.

5.3.2 CL Assessment

After functionalizing GNPs with CL luminol molecules, the concentration of the stock solution was adjusted such that a 10 µl solution dispensed ~$1x10^{10}$ GNPs. This was used in a series of dilutions to obtain GNP-MUA-LUM solutions at concentrations varying over 8 orders of magnitude. The PDMS wells on the test strip were loaded with a 10 µl solution of respective concentration and dried in the incubator before CL measurements. Figure 5.7a and Figure 5.7b include representative snapshot CCD images of CL signals recorded during the CL measurements from the PDMS wells loaded with $1x10^{10}$ and $1x10^{3}$ GNP-MUA-LUM, respectively. Complete CL images are shown in Appendix Figure C.3 from the PDMS wells loaded with the LUM-labeled GNPs from $1x10^{10}$ to $1x10^{3}$ particles/well. Photons were emitted immediately upon addition of the premixed solution consisting of 4 µl of NaOH (0.033 M), 4 µl of H_2O_2 (0.47 M), and 4 µl of $Fe(CN)_6^{3-}$ (1.0 mM) to the PDMS wells. The region of interest (ROI) in the image was selected over the specific PDMS well using the IVIS Lumina II system software and the photon counts was integrated over this region.

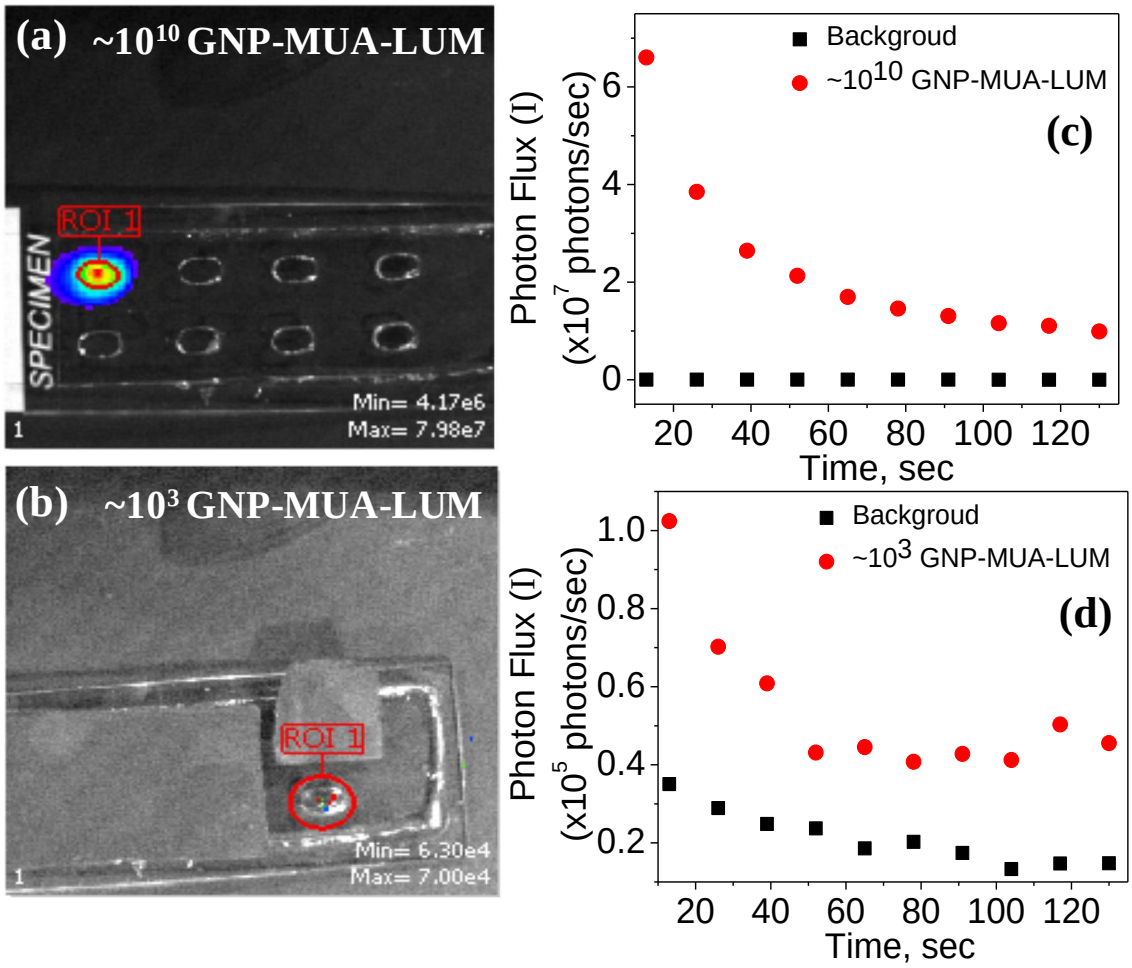

Figure 5.7 CL signal recorded using IVIS Lumina II. (a) and (b) are snapshot images using psuedocolor to represent the CL intensities from two designated PDMS wells on a glass slide, which are loaded with ~1x10^{10} and ~1x10^{3} GNP-MUA-LUM, respectively. (c) and (d) show plots of integrated CL signal (filled circles) from the wells containing ~1.0x10^{10} and ~1.0x10^{3} GNP-MUA-LUM over background signal (filled squares) obtained in control experiments without $Fe(CN)_6^{3-}$ ions.

CL of luminol is known to follow a flash mechanism in which CL occurs immediately and then decays quickly.[31] The half-life strongly depends on the experimental conditions.[171] It can be seen in Figure 5.7c and Figure 5.7d, that the integrated CL signal (filled circles) has the maximum value at the first snapshot image for the PDMS wells loaded respectively with 1x10^{10} to 1x10^{3} luminol labeled GNPs. The data sampling rate was limited by the imaging speed at ~13 s/frame. The CL signal decayed exponentially with time as shown in Figure 5.7c and Figure

5.7d. Nevertheless, the CL signal from $1x10^3$ luminol-labeled GNPs clearly remained above the background (filled squares) which was recorded by replacing the 1.0 mM $Fe(CN)_6^{3-}$ solution with DI water while all other experimental settings were kept the same. The half life is about 30 seconds for both $1.0x10^{10}$ to $1.0x10^3$ luminol labeled GNPs, indicating that the CL mechanism remained the same over such a large range.

In the experiment with the lowest number of luminol labeled GNPs (i.e. ~1,000 GNPs), the total number of CL photons was comparable to the estimated number of luminol molecules (~$1.4x10^3$ luminol/GNP) by assuming the formation of a close-packed thiol monolayer with the same density as on a flat gold surface. But the large variation in the measurement value limited the assessment of exact value of CL quantum yield of the attached luminol molecules. In an alternative approach, the CL signal measured with $1.0x10^{10}$ luminol-labeled GNPs was compared with that from the same number of free luminol molecules that were dispersed in solution (4 μL of 23 μM of luminol in each PDMS well) with all other parameters the same. As shown in Appendix Figure C.4, the maximum CL signal from GNP-MUA-LUM is about ~37% of that from the luminol solution. The reduction factor is ~2.7, much smaller than the 5.0 times reduction in the previous study using 30 nm diameter GNPs through a much shorter linker (3-mercaptopropionic acid).[192] If the absorption of the CL photons by GNPs is considered, the difference between luminols attached to GNPs and those freely dispersed in solution in our measurements is even smaller. This is probably why ultrahigh sensitivity was obtained in this study. The mechanism of CL on luminol-labeled GNPs and the size effect of GNP are certainly worth further study. Due to the fast decay in the CL signal, it is necessary to use the signal from the first snapshot (i.e the maximum CL signal I_{max}) instead of the average signal for quantitative analyses.

Figure 5.8 shows a calibration curve in which the background subtracted maximum CL signal (ΔI_{max}) is plotted vs. the number of luminol-labeled GNPs in a PDMS well.

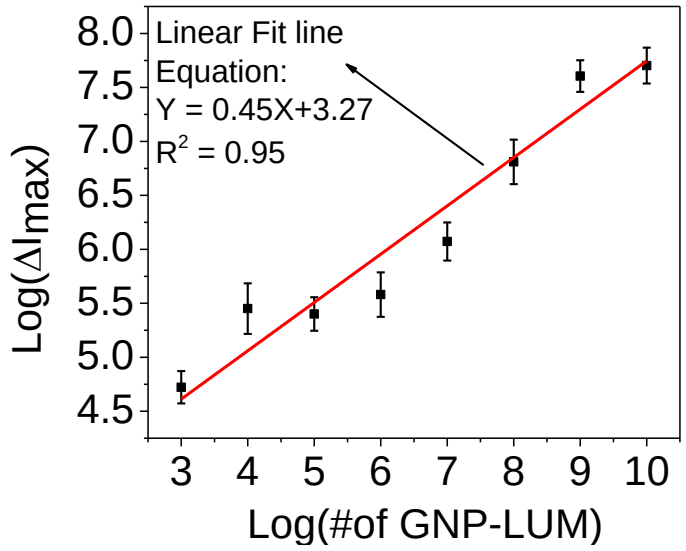

Figure 5.8 Calibration curve on a Log-Log scale of ΔI_{max} (background subtracted peak CL intensity from kinetic measurements) vs. the number of luminol modified GNPs. The solid line is the linear fitting line.

A linear relationship between the CL signal and the number of GNPs was obtained from $1x10^3$ to $1x10^{10}$ GNPs as:

$$Log(\Delta I_{max}) = 0.45Log(N_{GNP}) + 3.27 \quad \textbf{(5.1)}$$

with a R^2 value of 0.95, where N_{GNP} is the number of GNPs placed in the PDMS well. Even though CL signal from 1,000 GNPs can be clearly observed with ΔI_{max} = ~$5.0x10^4$ photons/s (see Figure 5.7d), the rigorous statistical detection limit depends on the standard deviation of the CL measurements with blank samples (with s_{blank} = $1.9x10^4$ photons/s). Following the convention, the signal at the detection limit needs to be:

$$I_{DL} = I_{blank} + 3s_{blank} \quad \textbf{(5.2)}$$

where the background signal I_{blank} is ~$2.4\ x10^4$ photons/s. Therefore, the statistical detection limit is derived to be ~2,600 GNPs. This can be improved by reducing the variation of

the background reading which was due to the variation in the experimental setting and the drift of the CCD camera.

The CL signal should be, in principle, proportional to the concentration of the luminol. However, the relationship between the background-subtracted maximum CL signal (ΔI_{max}) and the number of luminol-attached GNPs (N) was $\Delta I_{max} \propto N^{0.45}$ instead of a linear relationship as $\Delta I_{max} \propto N$. This might be due to luminol molecules being attached to the surface of GNPs which were deposited at the bottom of the well. It is a pseudo-two-dimensional system instead of the usual dispersion in bulk solution. The mechanism is worth further investigation.

GNPs are known to present strong SPR, which has been widely utilized to enhance the sensitivity in colorimetric or optical absorption methods.[78, 147] Our results suggest that CL can provide even higher detection sensitivity. To compare CL with absorption approaches, Figure 5.9 shows the UV-visible absorption spectra of GNP-MUA-LUM measured with 350 μl solution in a microcuvette of 10.0 mm optical path length. The total number of GNPs is varied from $1x10^{10}$ to $1x10^{3}$. At high concentrations (≥ ~$1x10^{8}$ GNPs), it shows a strong absorption peak at 518 nm, corresponding to the SPR of GNPs of ~10 nm in diameter. However, the absorption is below the baseline noise as the number of GNPs is at or below $1x10^{7}$. Also, the red color associated with the GNPs is only visually observable with naked eyes when the number of GNPs is more than ~$1x10^{9}$. The height of the absorption peak at 518 nm is fitted and plotted against the number of GNPs in the solution in Appendix Figure C.5. Clearly, the peak absorbance varies linearly with the number of GNPs when it is near or above $1x10^{8}$, but quickly drops below the detection limit when it is less than $1x10^{8}$.

In contrast, the CL signal using luminol-labeled GNPs can be easily observed with as few as 1,000 GNPs (Figure 5.7d), making this approach particularly useful for affinity biosensors based on Scheme 2 illustrated in Figure 5.3 in which the CL signal depends on the number of luminol-labeled GNPs captured through a co-functionalized recognition probe.[197-198] *To our knowledge, this is the first experimental demonstration that the detection sensitivity can be enhanced by at least 10^{4} times by using CL of luminol-labeled GNPs as compared to the optical absorption of GNPs.*

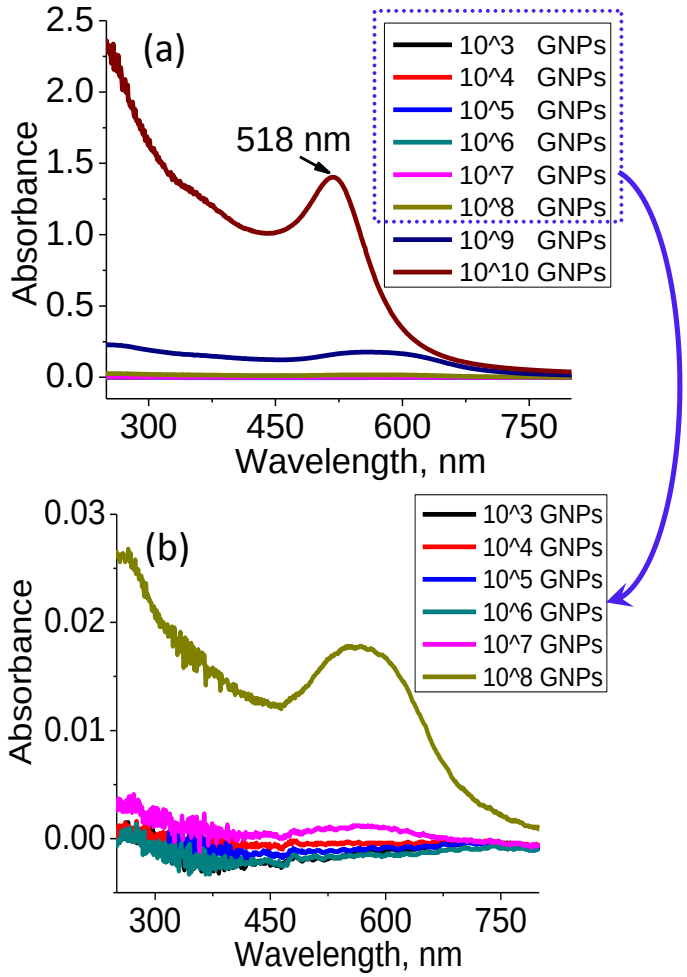

Figure 5.9 (a) The UV-Visible absorption spectra measured with varying number of GNP-MUA-LUM in 350 μL solution in a microcuvette with an optical pathlength of 10.0 mm. (b) The enlarged view to show the absorption spectra of highly diluted GNP-MUA-LUM solutions.

5.3.3 CL Detection of Unlysed and Lysed Red Blood Cells

As illustrated in Figure 5.3, the luminol-labeled GNPs can be used for CL detection under two different schemes. In this study, we focused on demonstrating the detection of blood samples using Scheme 1. Unlysed and lysed sheep blood samples were used to replace $Fe(CN)_6^{3-}$ ions as the analyte which also serves as the catalyst to generate luminol CL. The solutions containing ~$1x10^{10}$ luminol-labeled GNPs were preloaded in different PDMS wells and the solvent was then dried out. CL measurements were performed after adding the mixture of 4.0 μl of NaOH (0.1 M) and 4.0 μl of H_2O_2 (1.41 M) as well as 4.0 μl of blood sample of desired concentrations. The concentration of the sheep red blood cells in the stock blood solution was ~$4.6x10^9$ cells/ml, as

estimated by cell counting. The size of the sheep red blood cell is about 3-4 µm. In some experiments, the sheep red blood cells were lysed following the procedure described in the experimental section. The representative kinetic CL data obtained with the stock solutions of unlysed and lysed blood samples, respectively, and with those after 10^8 times dilution are shown in Figure 5.10. The CL signal of the lysed blood samples experienced a rapid decay with a half life of ~30 seconds (Figure 5.10a and Figure 5.10b), similar to what was observed with $Fe(CN)_6^{3-}$ ions (as shown in Figure 5.7c and Figure 5.7d). It is remarkable that such a strong CL signal can be observed with the lysed blood samples even after dilution by 108 times, which corresponds to ~0.18 cell/well.

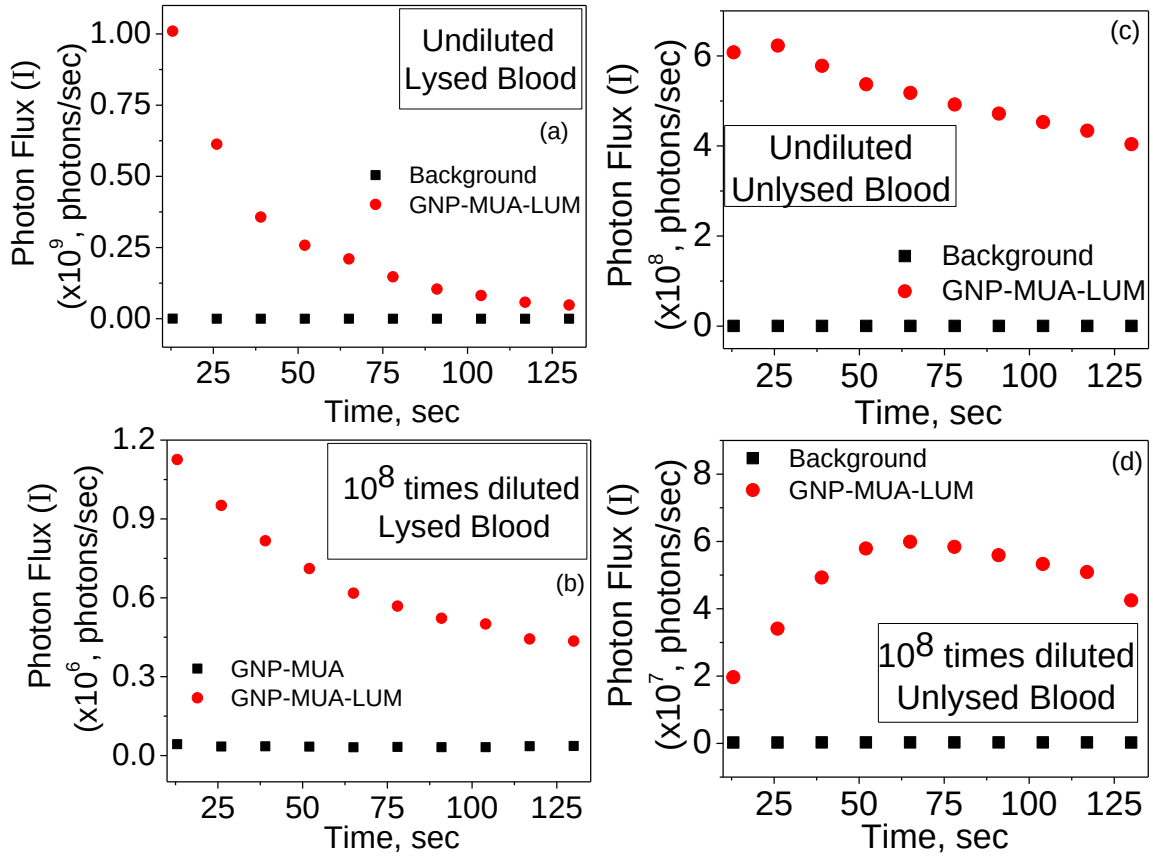

Figure 5.10 The kinetic plots of the CL signal (filled circles) of lysed (panels a and b) and unlysed (panels c and d) blood samples. Panels a and c were measured at stock concentration and panels b and d were measured after 10^8 fold dilution. The black squares represent the background from control experiments without adding any blood sample.

Interestingly, the unlysed blood samples showed quite different kinetics in CL measurements in both original and diluted samples. As shown in Figure 5.10c and Figure 5.10d, the CL signal rises in the initial period (~26 and 65 s, respectively) and then slowly decays. The rising and decay rates were lower in the highly diluted sample as compared to the original one. This is likely because the red blood cells need to be lysed first to release the hemoglobin to the exterior environment. The degradation of the polypeptidic portion of the hemoglobin then takes place, removing the protection to the reduced form of iron (i.e. Fe^{2+}) at the center of the histidine coordination.[171] As a result, Fe^{2+} is quickly oxidized into Fe^{3+} and becomes an active catalyst to facilitate the reaction of luminol molecules to generate CL. In the stock solution of the unlysed blood sample, there are likely many residual hemes outside the cell, hence the initial rise in CL signal is not prominent. But for the sample diluted by 10^8 times (to ~46 cells/ml), likely only a single red blood cell is randomly picked and dispensed into the PDMS well, which was lysed by the high concentration of NaOH (~0.033 M after mixing) to release hemoglobin for subsequent CL reaction. Hence the generation of CL is delayed by ~65 seconds.

Figure 5.11a and Figure 5.11b show the Log-Log plots of the background subtracted maximum CL signal (ΔI_{max}) vs. the dilution factor for lysed and unlysed blood samples, respectively. A linear relationship between $\log(\Delta I_{max})$ and log(dilution) was obtained for the lysed sample in a large range of the dilution factor ranging from 0 to 10^8. A slope of -0.459 is obtained from Figure 5.11a, which is very close to that of $\log(\Delta I_{max})$ vs. $\log(N_{GNP})$ (with N_{GNP} as the number of luminol-labeled GNPs) in Figure 5.8. This confirms that the CL in these experiments is likely based on the same mechanism (i.e. Scheme 1 in Figure 5.3). The unlysed blood sample in Figure 5.11b, however, shows a transition at the dilution factor of ~$5x10^4$. Two straight lines are needed to fit the experimental data, with a slope of -0.308 below 10^4 times dilution and a very small slope of -0.031 above 10^5 times of dilution. At the transition point of a dilution factor of ~$5x10^4$, there are ~370 cells dispensed in the PDMS well by calculation. This number is close to the limit of statistically reliable sampling. Other catalysts beside the hemoglobin from the intact red blood cells may also contribute to the CL signal and generates the CL even after 10^8 times dilution even though the slope is much smaller.

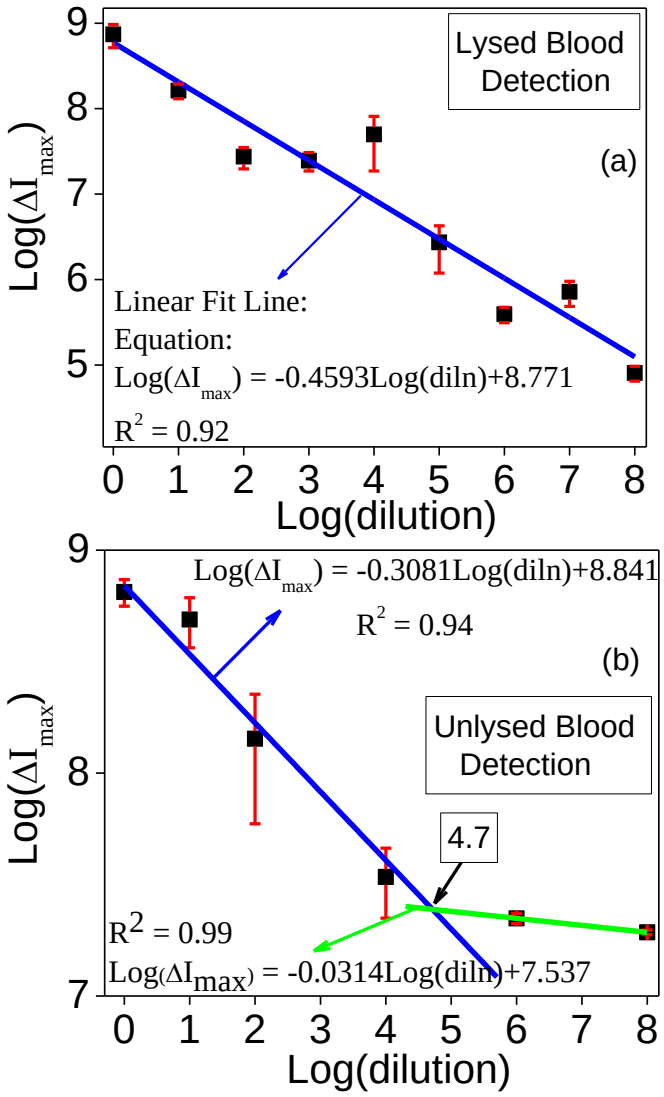

Figure 5.11 Calibration curves of the lysed and unlysed blood samples on the Log-Log scale of ΔI_{max} (the background subtracted peak CL intensity in kinetic measurements) vs. the dilution factor. The solid lines are linear fitting to two regions.

In this study, the CL reaction was carried out in a light tight chamber with a highly sensitive CCD which has relatively high cost. However, the method can be implemented with a photomultiplier tube detector coupled with fiber optics as a simple low-cost system with comparable photon collection efficiency. It is possible to develop a portable CL system for rapid and ultrasensitive point-of-care applications, which remains challenging with other techniques

such as fluorescence methods.[31] This CL method can be also applied on affinity based biosensors by incorporating additional biorecognition probes (such as antibodies or nucleic acid sequences) in luminol-labeled GNPs and using Scheme 2 in Figure 5.3 for analytical detection.

5.4 Conclusions

In conclusion, we have demonstrated that very strong CL signal can be generated with luminol molecules covalently attached to GNPs through an alkane thiol linker. This approach may be adopted for ultrasensitive analysis under two different schemes as shown in this work. The CL signal measured in 1.0 mM $Fe(CN)_6^{3-}$ solution scales linearly with the number of luminol-labeled GNPs in the log-log scale in a wide range from $1.0x10^{10}$ to $1.0x10^{3}$ GNPs in small PDMS wells. The ability to detect as small as 1,000 GNPs with luminol attachment is attributed to a high CL quantum efficiency of luminol molecules comparable to those in bulk solutions. The assessed detection sensitivity by CL from luminol-labeled GNPs is four orders of magnitude higher than that by optical absorption. By preloading sufficient amount of luminol-labeled GNPs in an array of PDMS microwells, we have demonstrated that strong CL can be generated from trace amount of blood samples in which either intact or lysed red blood cells are present. Particularly, the lysed blood sample can be detected following 10^{8} fold dilution. This method can be readily integrated with fiber optics and a low-cost detector into a portable point-of-care system for a rapid and ultrasensitive detection of trace blood contamination in hospitals, forensic sites, or other venues. The luminol-labeled GNPs can be further coupled with specific affinity probes such as antibodies or nucleic acid sequences to develop ultrasensitive biosensors for disease detection.

Chapter 6 - Conclusions and Future Direction

In this dissertation, nanoelectrodes and nanoparticles have been tried for developing different biosensing strategies. Most of our work is driven by the fact that there is a growing demand for label-free, fast, and sensitive techniques, which can at some point be utilized to construct hand-held devices for point-of-care detection. All of these project works provide an understanding of materials, methods and mechanisms of utilizing nanoscale material for different applications and hope that other researchers will benefit from results we have obtained to develop better materials and devices in future.

6.1 Understanding the electron transfer rates (ETRs) at NEAs and GCEs by AC and DC voltammetry

In this study, we used ferrocene functionalized NEAs and GCE (standard for comparison) to study the electron transfer kinetics. Initially, we employed DC voltammetry in both the cases and found that the ETR in case of NEA is very slow when compared to GCE (~17 times). This can seriously limit the use of NEA for biosensing using DC based electrochemical methods. To our surprise, when we used AC voltammetry instead of DC voltammetry we observed 100 times higher electron transfer rate at the NEAs. Lot of effort was made to quantitatively account for this behavior. Finally, we used electrochemical impedance spectroscopy and a proper physical model was used to account for all the anomalous behavior of NEAs when AC electrochemical technique is used. The electrochemical properties of the nanoelectrode were found to critically depend on the unique conical graphitic stacking of the carbon nanofibers, which facilitates a new capacitive pathway in high-frequency AC measurements.

In future, we can take advantage of high frequency signal enhancement given by NEA to develop biosensors, especially for cancerous protease detection. EIS experiments with GCE and NEA functionalized with tetrapeptide needs to be done, by biasing the WE at the formal potential of Fc. This experiment will give us the long range ETR, which can be compared to the values with just Fc attached WE. Optimization of ACV experimental conditions for each sequence of peptides needs to done carefully in the assay buffer. We can easily program the potentiostat to monitor real-time ACV. This will give us information about the kinetic behavior of the enzyme

understudy. The kinetic parameters thus obtained from electrochemistry can be compared from literature values or the values found from other standard assay techniques.

6.2 Dielectrophoretic trapping of bacterial cells at micropatterned NEAs

Rapid detection of pathogens is very crucial in several applications like monitoring water and food quality. We demonstrate the use of AC dielectrophoresis (DEP) and electrochemical impedance techniques with vertically aligned carbon nanofiber (VACNF) nanoelectrode arrays (NEAs) and ITO-coated glass in "points-and-lid" configuration. A nano-DEP device can be fabricated using UV-photolithography. A high frequency ac field was applied between NEA and ITO to generate p-DEP at the tips of exposed CNFs. Enhanced electric field gradient generated at the exposed CNF tips due to reduction in electrode size down to nanometer scale and high aspect ratio (~100) helps to overcome large hydrodynamic drag force experienced by *E. coli* flowing at higher flow velocities was noticed. A significant number of *E. coli* were captured at a high flow velocity of 1.6 mm/sec. A noticeable change in absolute impedance (|Z|) value at the NEA was observed in the Bode plot of impedance experiments. The results obtained in this study suggest the possibility of integration of a fully functional electronic device for rapid, reversible and label-free detection of pathogenic bacteria.

In future, to add more towards detection of pathogen we can integrate the DEP capture process with measuring Raman finger print of the captured pathogen. To enhance the Raman signal it might be necessary to incorporate nanoparticles along with pathogen so that both pathogen and nanoparticles are captured simultaneously, or another way would be to decorate exposed CNF with nanoparticles before DEP. For both the cases theoretical predictions of CM factor needs to be done. The methodologies presented in this chapter can also be directly extended for its use to capture smaller bioparticles like viruses.

6.3 Luminol decorated gold nanoparticles (GNPs) as a sensitive chemiluminescence (CL) biosensor for trace blood detection

CL is a very powerful analytical technique which can provide sensitivity orders of magnitude higher than that of commonly used fluoresecence methods. In conventional CL, the molecules (such as luminol) are dissolved in solutions. In our case luminol was covalently attached to GNPs of ~10 nm diameter. The nanoparticle serves as a carrier with large surface

area to ensure the functionalization of a large quantity of CL molecules. It provides the capability to be either suspended in solution or immobilized on a surface. This enables the application of nanoparticle-functionalized CL for detection of analytes in solution (such as red blood cells) in a multiwell format or as an amplified readout technique in a test strip format based on specific affinity binding. We have demonstrated a detailed procedure to prepare luminol-functionalized GNPs with convincing characterization with UV-Vis and IR spectroscopy and TEM. Two implementation schemes using luminol-GNPs were illustrated. In one scheme luminol-functionalized GNPs were exposed to blood samples of different concentrations and we were able to detect lysed blood samples after dilution by 10^8 times down on single red blood cell. In the other scheme, the CL signal was measured using 1.0 mM $Fe(CN)_6^{3-}$ solution. The CL signal scaled linearly with the number of luminol-labeled GNPs in the log-log scale in a wide range from $1.0x10^{10}$ to $1.0x10^3$ GNPs in small PDMS wells. The ability to detect as small as 1,000 GNPs with luminol attachment is attributed to a high CL quantum efficiency of luminol molecules comparable to those in bulk solutions. The assessed detection sensitivity by CL from luminol-labeled GNPs is four orders of magnitude higher than that by optical absorption.

In future, ultrasensitive readout methods can be developed for the detection of analytes or biomarkers in well-array format or affinity-based test strips. For examples we can detect microbes, proteins, and nucleic acid fragments (DNA, RNA, synthetic nucleic acids, etc.). The chemiluminescent assay can also adapted for the specific detection of virus particles (e.g. Hepatitis C) which is orders of magnitude more sensitive that the state-of-the-art colorimetric method based on light absorption by gold nanoparticles. It can potentially detect Hepatitis infections at very early stage without using PCR-based laboratory techniques. It can also be adapted for diagnosis of various diseases (such as cancers) through the ultrasensitive detection of specific biomarkers (such as proteins, peptide, ligands, and particular sequences of nucleic acid fragments).

Literature Cited

1. http://goldbook.iupac.org.

2. Kim, J. M.; Chang, S. M.; Muramatsu, H.; Isao, K. *Korean J. Chem. Eng.* **2011**, *28*, 987-1008.

3. Thévenot, D. R.; Toth, K.; Durst, R. A.; Wilson, G. S. *Biosens. Bioelectron.* **2001**, *16*, 121-131.

4. Patel, P. D. *TrAC, Trends Anal. Chem.* **2002**, *21*, 96-115.

5. Rogers, K. R.; Lin, J. N. *Biosens. Bioelectron.* **1992**, *7*, 317-321.

6. Rogers, K. R. *Biosens. Bioelectron.* **1995**, *10*, 533-541.

7. Collings, A. F.; Caruso, F. *Rep. Prog. Phys.* **1997**, *60*, 1397-1445.

8. Mehrvar, M.; Bis, C.; Scharer, J. M.; Moo-Young, M.; Luong, J. H. *Anal. Sci.* **2000**, *16*, 677-692.

9. Baird, C. L.; Myszka, D. G. *J. Mol. Recognit.* **2001**, *14*, 261-268.

10. Selvan, S. T.; Tan, T. T. Y.; Yi, D. K.; Jana, N. R. *Langmuir* **2010**, *26*, 11631-11641.

11. Jenkins, M., *Biomedical Polymers*. Woodhead Publishing: Cambridge, UK, 2007.

12. Kim, S. N.; Rusling, J. F.; Papadimitrakopoulos, F. *Adv. Mater.* **2007**, *19*, 3214-3228.

13. http://www.cancer.org/acs/groups/content/@nho/documents/document/caff2006pwsecuredpdf.pdf.

14. *Diabetes Care* **2003**, *26*, 917-932.

15. Nataro, J. P.; Kaper, J. B. *Clin. Microbiol. Rev.* **1998**, *11*, 403-403.

16. Mead, P. S.; Slutsker, L.; Dietz, V.; McCaig, L. F.; Bresee, J. S.; Shapiro, C.; Griffin, P. M.; Tauxe, R. V. *Emerging Infect. Dis.* **1999**, *5*, 607-625.

17. Abubakar, I.; Irvine, L.; Aldus, C. M.; Wyatt, G. M.; Fordham, R.; Schelenz, S.; Shepstone, L.; Howe, A.; Peck, M.; Hunter, P. R. *Health Technol. Assess.* **2007**, *11 (36)*.

18. *http://accessscience.com/content/Pathogen-detection,-food-borne/YB031850*.

19. Fung, D. Y. C. *Comprehensive Reviews in Food Science and Food Safety* **2002**, *1*, 3-22.

20. Melechko, A. V.; Merkulov, V. I.; McKnight, T. E.; Guillorn, M. A.; Klein, K. L.; Lowndes, D. H.; Simpson, M. L. *J. Appl. Phys.* **2005**, *97*, 41301-1-39.

21. Leonard, P.; Hearty, S.; Brennan, J.; Dunne, L.; Quinn, J.; Chakraborty, T.; O'Kennedy, R. *Enzyme Microb. Technol.* **2003**, *32*, 3-13.

22. Taguchi, T.; Takeyama, H.; Matsunaga, T. *Biosens. Bioelectron.* **2005**, *20*, 2276-2282.

23. Mansfield, L. P.; Forsythe, S. J. *Food Microbiol.* **2001**, *18*, 361-366.

24. Rompré, A.; Servais, P.; Baudart, J.; de-Roubin, M.-R.; Laurent, P. *J. Microbiol. Methods* **2002**, *49*, 31-54.

25. Schena, M.; Shalon, D.; Davis, R. W.; Brown, P. O. *Science* **1995**, *270*, 467-470.

26. Lipshutz, R. J.; Morris, D.; Chee, M.; Hubbell, E.; Kozal, M. J.; Shah, N.; Shen, N.; Yang, R.; Fodor, S. P. A. *BioTechniques* **1995**, *19*, 442-447.

27. Southern, E.; Mir, K.; Shchepinov, M. *Nat. Genet.* **1999**, *21*, 5-9.

28. Singh, A.; Goering, R. V.; Simjee, S.; Foley, S. L.; Zervos, M. J. *Clin. Microbiol. Rev.* **2006**, *19*, 512-530.

29. Powledge, T. M. *Advances in Physiology Education* **2004**, *28*, 44-50.

30. Kim, H.-S.; Pyun, J.-C. *Procedia Chemistry* **2009**, *1*, 1043-1046.

31. Knox Van Dyke, C. V. D., Karen Woodfork, *Luminescence Biotechnology: Instrumentation and Applications*. CRC Press, Newyork: 2001.

32. White, E. H.; Zafiriou, O.; Kagi, H. H.; Hill, J. H. M. *J. Am. Chem. Soc.* **1964**, *86*, 940-941.

33. White, E. H.; Bursey, M. M. *J. Am. Chem. Soc.* **1964**, *86*, 941-942.

34. White, E. H.; Roswell, D. F. *Acc. Chem. Res.* **1970**, *3*, 54-62.

35. Wang, J. *Analyst* **2005**, *130*, 421-426.

36. Vo-Dinh, T.; Cullum, B. M.; Stokes, D. L. *Sensors Actuators B: Chem.* **2001**, *74*, 2-11.

37. Arben, M., *Biosensing Using Nanomaterials*. John Wiley & Sons: New Jersey, 2009.

38. Nugent, J. M.; Santhanam, K. S. V.; Rubio, A.; Ajayan, P. M. *Nano Lett.* **2001**, *1*, 87-91.

39. Wang, J.; Musameh, M.; Lin, Y. *J. Am. Chem. Soc.* **2003**, *125*, 2408-2409.

40. Luo, H.; Shi, Z.; Li, N.; Gu, Z.; Zhuang, Q. *Anal. Chem.* **2001**, *73*, 915-920.

41. Cui, D. *J. Nanosci. Nanotechnol.* **2007**, *7*, 1298-1314.

42. Willner, I. *Science* **2002**, *298*, 2407-2408.

43. Patolsky, F.; Weizmann, Y.; Willner, I. *Angew. Chem. Int. Ed.* **2004**, *43*, 2113-2117.

44. Britto, P. J.; Santhanam, K. S. V.; Ajayan, P. M. *Bioelectrochem. Bioenerg.* **1996**, *41*, 121-125.

45. Davis, J. J.; Coles, R. J.; Allen, H.; Hill, O. *J. Electroanal. Chem.* **1997**, *440*, 279-282.

46. Che, G. L.; Lakshmi, B. B.; Fisher, E. R.; Martin, C. R. *Nature* **1998**, *393*, 346-349.

47. Rajesh; Ahuja, T.; Kumar, D. *Sensors Actuators B: Chem.* **2009**, *136*, 275-286.

48. Lin, Y.; Lu, F.; Tu, Y.; Ren, Z. *Nano Lett.* **2003**, *4*, 191-195.

49. Yu, Y.; Cimeno, A.; Lan, Y. C.; Rybczynski, J.; Wang, D. Z.; Paudel, T.; Ren, Z. F.; Wagner, D. J.; Qiu, M. Q.; Chiles, T. C.; Cai, D. *Micro & Nano Letters* **2009**, *4*, 27-33.

50. Heller, I.; Mannik, J.; Lemay, S. G.; Dekker, C. *Nano Lett.* **2009**, *9*, 377-382.

51. Koehne, J.; Chen, H.; Li, J.; Cassell, A. M.; Ye, Q.; Ng, H. T.; Han, J.; Meyyappan, M. *Nanotechnology* **2003**, *14*, 1239-1245.

52. Koehne, J. E.; Chen, H.; Cassell, A. M.; Yi, Q.; Han, J.; Meyyappan, M.; Li, J. *Clinic. Chem.* **2004**, *50*, 1886-1893.

53. Lee, H. J.; Beriet, C.; Ferrigno, R.; Girault, H. H. *J. Electroanal. Chem.* **2001**, *502*, 138-145.

54. Cai, D.; Ren, L.; Zhao, H.; Xu, C.; Zhang, L.; Yu, Y.; Wang, H.; Lan, Y.; Roberts, M. F.; Chuang, J. H.; Naughton, M. J.; Ren, Z.; Chiles, T. C. *Nat Nano* **2010**, *5*, 597-601.

55. Lin, Y.; Lu, F.; Tu, Y.; Ren, Z. *Nano Lett.* **2004**, *4*, 191-195.

56. Wang, J.; Lin, Y. *TrAC, Trends Anal. Chem.* **2008**, *27*, 619-626.

57. Li, J.; Ng, H. T.; Cassell, A.; Fan, W.; Chen, H.; Ye, Q.; Koehne, J.; Han, J.; Meyyappan, M. *Nano Lett.* **2003**, *3*, 597-602.

58. Koehne, J.; Li, J.; Cassell, A. M.; Chen, H.; Ye, Q.; Ng, H. T.; Han, J.; Meyyappan, M. *J. Mater. Chem.* **2004**, *14*, 676-684.

59. Li, Y.; Kaneko, T.; Hirotsu, Y.; Hatakeyama, R. *Small* **2010**, *6*, 27-30.

60. Arrigan, D. W. M. *Analyst* **2004**, *129*, 1157-1165.

61. Kuhr, W. *Nat. Biotechnol.* **2000**, *18*, 1042.

62. Gooding, J. J. *Electroanalysis* **2002**, *14*, 1149-1156.

63. Sosnowski, R.; Tu, E.; Butler, W.; O'Connell, J.; Heller, M. *Proc. Natl. Acad. Sci. U.S.A.* **1997**, *94*.

64. Umek, R. M.; Lin, S. W.; Vielmetter, J.; Terbrueggen, R. H.; Irvine, B.; Yu, C. J.; Kayyem, J. F.; Yowanto, H.; Blackburn, G. F.; Farkas, D. H.; Chen, Y. P. *J. Mol. Diagnostics* **2001**, *3*, 74-84.

65. Popovich, N.; Thorp, H. *Interface* **2002**, *11*.

66. Ghindilis, A. L.; Smith, M. W.; Schwarzkopf, K. R.; Roth, K. M.; Peyvan, K.; Munro, S. B.; Lodes, M. J.; Stover, A. G.; Bernards, K.; Dill, K.; McShea, A. *Biosens. Bioelectron.* **2007**, *22*, 1853-1860.

67. Dill, K.; Ghindilis, A.; Schwarzkopf, K. *Lab Chip* **2006**, *6*, 1052-1055.

68. Varshney, M.; Li, Y. B. *Biosens. Bioelectron.* **2007**, *22*, 2408-2414.

69. Varshney, M.; Li, Y. B.; Srinivasan, B.; Tung, S. *Sensors and Actuators B-Chemical* **2007**, *128*, 99-107.

70. Yang, L.; Bashir, R. *Biotechnol. Adv.* **2008**, *26*, 135-150.

71. Voldman, J. *Annu. Rev. Biomed. Eng.* **2006**, *8*, 425-454.

72. Jianrong, C.; Yuqing, M.; Nongyue, H.; Xiaohua, W.; Sijiao, L. *Biotechnol. Adv.* **2004**, *22*, 505-518.

73. Wang, J. *Small* **2005**, *1*, 1036-1043.

74. Essner, J. Dye Sensitized Solar Cells: Optimization of Gratzel Solar Cells Towards Plasmonic Enhanced Photovoltaics. Kansas State University, 2011.

75. Zhang, X.; Guo, Q.; Cui, D. *Sensors* **2009**, *9*, 1033-1053.

76. http://www.tedpella.com/gold_html/goldsols.htm.

77. Mirkin, C. A.; Letsinger, R. L.; Mucic, R. C.; Storhoff, J. J. *Nature* **1996**, *382*, 607-609.

78. Xia, F.; Zuo, X.; Yang, R.; Xiao, Y.; Kang, D.; Vallee-Belisle, A.; Gong, X.; Yuen, J. D.; Hsu, B. B. Y.; Heeger, A. J.; Plaxco, K. W. *Proc Natl Acad Sci* **2010**, *107*, 10837-10841.

79. Jena, B. K.; Raj, C. R. *Biosens. Bioelectron.* **2008**, *23*, 1285-1290.

80. Mao, X.; Ma, Y.; Zhang, A.; Zhang, L.; Zeng, L.; Liu, G. *Anal. Chem.* **2009**, *81*, 1660-1668.

81. Syed, L. U.; Liu, J.; Prior, A. M.; Hua, D. H.; Li, J. *Electroanalysis* **2011**, *23*, 1709-1717.

82. Syed, L. U.; Liu, J.; Price, A. K.; Li, Y.-f.; Culbertson, C. T.; Li, J. *Electrophoresis* **2011**, *32*, 2358-2365.

83. Cruden, B. A.; Cassell, A. M.; Ye, Q.; Meyyappan, M. *J. Appl. Phys.* **2003**, *94*, 4070.

84. Ren, Z. F.; Huang, Z. P.; Xu, J. W.; Wang, J. H.; Bush, P.; Siegal, M. P.; Provencio, P. N. *Science* **1998**, *282*, 1105-1107.

85. Ngo, Q.; Cassell, A. M.; Austin, A. J.; Li, J.; Krishnan, S.; Meyyappan, M.; Yang, C. Y. *IEEE Electron Device Lett.* **2006**, *27*, 221.

86. Bard, A. J.; Faulkner, L. R., *Electrochemical Methods: Fundamental and Applications*. 2nd ed.; Wiley: New York, 2001.

87. Menon, V. P.; Martin, C. R. *Anal. Chem.* **1995**, *67*, 1920-1928.

88. Wang, J., *Analytical Electrochemistry*. 3rd ed.; Wiley-VCH: 2006.

89. Ordeig, O. *Electroanalysis* **2007**, *19*, 1973-1986.

90. Li, J.; Koehne, J. E.; Cassell, A. M.; Chen, H.; Ng, H. T.; Ye, Q.; Fan, W.; Han, J.; Meyyappan, M. *Electroanalysis* **2005**, *17*, 15-27.

91. Baramee, A.; Coppin, A.; Mortuaire, M.; Pelinski, L.; Tomavo, S.; Brocard, J. *Biorg. Med. Chem.* **2006**, *14*, 1294-1302.

92. Tsierkezos, N.; Ritter, U. *J. Appl. Electrochem.* **2010**, *40*, 409-417.

93. Creager, S.; Yu, C. J.; Bamdad, C.; O'Connor, S.; MacLean, T.; Lam, E.; Chong, Y.; Olsen, G. T.; Luo, J. Y.; Gozin, M.; Kayyem, J. F. *J. Am. Chem. Soc.* **1999**, *121*, 1059-1064.

94. Creager, S. E.; Wooster, T. T. *Anal. Chem.* **1998**, *70*, 4257-4263.

95. Zhang, L.; Austin, D.; Merkulov, V. I.; Meleshko, A. V.; Klein, K. L.; Guillorn, M. A.; Lowndes, D. H.; Simpson, M. L. *Appl. Phys. Lett.* **2004**, *84*, 3972-3974.

96. Banks, C. E.; Davies, T. J.; Wildgoose, G. G.; Compton, R. G. *Chem. Commun.* **2005**, 829-841.

97. Zoski, C. G. *Electroanalysis* **2002**, *14*, 1041-1051.

98. Penner, R. M.; Heben, M. J.; L., L. T.; Lewis, N. S. *Science* **1990**, *250*, 1118-1121.

99. Fan, F.-R. F.; Bard, A. J. *Science* **1995**, *267*, 871-874.

100. Yu, Z.; McKnight, T. E.; Ericson, M. N.; Melechko, A. V.; Simpson, M. L.; Morrison, B. *Nano Lett.* **2007**, *7*, 2188-2195.

101. McKnight, T. E.; Melechko, A. V.; Hensley, D. K.; Mann, D. G. J.; Griffin, G. D.; Simpson, M. L. *Nano Lett.* **2004**, *4*, 1213-1219.

102. Chidsey, C. E. D. *Science* **1991**, *251*, 919-922.

103. Chidsey, C. E. D.; Bertozzi, C. R.; Putvinski, T. M.; Mujsce, A. M. *J. Am. Chem. Soc.* **1990**, *112*, 4301-4306.

104. Sikes, H. D.; Smalley, J. F.; Dudek, S. P.; Cook, A. R.; Newton, M. D.; Chidsey, C. E. D.; Feldberg, S. W. *Science* **2001**, *291*, 1519-1523.

105. Choi, S. H.; Kim, B.; Frisbie, C. D. *Science* **2008**, *320*, 1482-1486.

106. Xia, J. L.; Chen, F.; Li, J. H.; Tao, N. J. *Nat. Nanotechnol.* **2009**, *4*, 505-509.

107. Heller, I.; Kong, J.; Heering, H. A.; Williams, K. A.; Lemay, S. G.; Dekker, C. *Nano Lett.* **2004**, *5*, 137-142.

108. McCreery, R. L. *Chem. Rev.* **2008**, *108*, 2646-2687.

109. Feldberg, S. W. *Anal. Chem.* **2010**, *82*, 5176-5183.

110. Xun, S.; Song, X.; Wang, L.; Grass, M. E.; Liu, Z.; Battaglia, V. S.; Liu, G. *J. Electrochem. Soc.* **2011**, *158*, A1260-A1266.

111. Lu, M. P.; Hsiao, C. Y.; Lai, W. T.; Yang, Y. S. *Nanotechnology* **2010**, *21*.

112. Li, Q. The Study of DNA Dynamics at Carbon Electrode Surface Toward DNA Sensors by Fluorescence and Electrochemical Impedance Spectroscopy. Kansas State University, 2011.

113. Laviron, E. *J. Electroanal. Chem.* **1979**, *101*, 19-28.

114. Finklea, H. O., Electrochemistry of organized monolayers of thiols and related molecules on electrodes. In *Electroanalytical Chemistry: a Series of Advances, Vol 19*, Marcel Dekker: New York, 1996; Vol. 19, pp 109-335.

115. Landis, E. C.; Hamers, R. J. *J. Phys. Chem. C* **2008**, *112*, 16910-16918.

116. Weber, K.; Creager, S. E. *Anal. Chem.* **1994**, *66*, 3164-3172.

117. Randin, J. P.; Yeager, E. *J. Electrochem. Soc.* **1971**, *118*, 711.

118. Wang, D. W.; Li, F.; Wu, Z. S.; Ren, W. C.; Cheng, H. M. *Electrochem. Commun.* **2009**, *11*, 1729-1732.

119. Almond, D. P.; Bowen, C. R. *Phys. Rev. Lett.* **2004**, *92*, 4.

120. http://www.ncbi.nlm.nih.gov/pubmedhealth/PMH0002267/.

121. Bogyo, M. *Proc. eedings of the National Academy of Sciences of the United States of America 107*, 2379-2380.

122. Chen, J.-M.; Dando, P. M.; Rawlings, N. D.; Brown, M. A.; Young, N. E.; Stevens, R. A.; Hewitt, E.; Watts, C.; Barrett, A. J. *J. Biol. Chem.* **1997**, *272*, 8090-8098.

123. Wu, W. Y.; Luo, Y. P.; Sun, C. Z.; Liu, Y. A.; Kuo, P.; Varga, J.; Xiang, R.; Reisfeld, R.; Janda, K. D.; Edgington, T. S.; Liu, C. *Cancer Res.* **2006**, *66*, 970-980.

124. http://www.rndsystems.com/pdf/2199-CY.pdf.

125. Svoboda, K.; Block, S. M. *Annu. Rev. Biophys. Biomol. Struct.* **1994**, *23*, 247-285.

126. Wu, J. R. *J. Acoust. Soc. Am.* **1991**, *89*, 2140-2143.

127. Jung, D. R.; Kapur, R.; Adams, T.; Giuliano, K. A.; Mrksich, M.; Craighead, H. G.; Taylor, D. L. *Crit. Rev. Biotechnol.* **2001**, *21*, 111-154.

128. Lapizco-Encinas, B.; Simmons, B.; Cummings, E.; Fintschenko, Y. *Electrophoresis* **2004**, *25*, 1695-1704.

129. Klodzinska, E.; Buszewski, B. *Anal. Chem.* **2009**, *81*, 8-15.

130. Desai, M. J.; Armstrong, D. W. *Microbiol. Mol. Biol. Rev.* **2003**, *67*, 38-51.

131. Arumugam, P. U.; Chen, H.; Cassell, A. M.; Li, J. *J. Phys. Chem. A* **2007**, *111*, 12772-12777.

132. Pohl, H. A., *Dielectrophoresis: The behavior of neutral matter in nonuniform electric fields*. Cambridge Univ. Press: Great Britain, 1978.

133. Betts, W. B. *Trends Food Sci. Technol.* **1995**, *6*, 51-58.

134. Suehiro, J.; Hamada, R.; Noutomi, D.; Shutou, M.; Hara, M. *J. Electrostatics* **2003**, *57*, 157-168.

135. Castellarnau, M.; Errachid, A.; Madrid, C.; Juarez, A.; Samitier, J. *Biophys. J.* **2006**, *91*, 3937-3945.

136. Park, K.; Akin, D.; Bashir, R. *Biomed. Microdevices* **2007**, *9*, 877-883.

137. Suehiro, J.; Ohtsubo, A.; Hatano, T.; Hara, M. *Sensors and Actuators B-Chemical* **2006**, *119*, 319-326.

138. Liju, Y.; Banada, P. P.; Chatni, M. R.; Kwan Seop, L.; Bhunia, A. K.; Ladisch, M.; Bashir, R. *Lab on a Chip: 6 (7) 896-905* **2006**, *6*, 896-905.

139. Crews, N.; Darabi, J.; Voglewede, P.; Guo, F.; Bayoumi, A. *Sensors and Actuators B-Chemical* **2007**, *125*, 672-679.

140. Tu, Y.; Lin, Y. H.; Yantasee, W.; Ren, Z. F. *Electroanalysis* **2005**, *17*, 79-84.

141. Tu, Y.; Lin, Y. H.; Ren, Z. F. *Nano Lett.* **2003**, *3*, 107-109.

142. Baker, S. E.; Tse, K. Y.; Lee, C. S.; Hamers, R. J. *Diamond Relat. Mater.* **2006**, *15*, 433-439.

143. Arumugam, P. U.; Chen, H.; Siddiqui, S.; Weinrich, J. A. P.; Jejelowo, A.; Li, J.; Meyyappan, M. *Biosens. Bioelectron.* **2009**, *24*, 2818-2824.

144. Edgcombe, C. J.; Valdre, U. *Journal Of Microscopy-Oxford* **2001**, *203*, 188-194.

145. Guillorn, M. A.; Hale, M. D.; Merkulov, V. I.; Simpson, M. L.; Eres, G. Y.; Cui, H.; Puretzky, A. A.; Geohegan, D. B. *Appl. Phys. Lett.* **2002**, *81*, 2860-2862.

146. Teo, K. B. K.; Minoux, E.; Hudanski, L.; Peauger, F.; Schnell, J. P.; Gangloff, L.; Legagneux, P.; Dieumegard, D.; Amaratunga, G. A. J.; Milne, W. I. *Nature* **2005**, *437*, 968.

147. Tuukkanen, S.; Toppari, J. J.; Kuzyk, A.; Hirviniemi, L.; Hytonen, V. P.; Ihalainen, T.; Torma, P. *Nano Lett.* **2006**, *6*, 1339-1343.

148. Hughes, M. P. *Electrophoresis* **2002**, *23*, 2569-2582.

149. Voldman, J. PhD Thesis, MIT, 2001.

150. Burke, P. J., Nano-dielectrophoresis: Electronic Nanotweezers. In *Encyclopedia of Nanoscience and Nanotechnology*, 2004; Vol. 6, pp 623-641.

151. Jones, T. B., *Electromechanics of Particles*. Cambridge University Press: Cambridge, UK, 1995.

152. Pethig, R. *Biomicrofluidics* **2010**, *4*, 022811.

153. Clague, D. S.; Wheeler, E. K. *Physical Review E* **2001**, *64*, 026605.

154. Huang, Y.; Pethig, R. *Meas. Sci. Technol.* **1991**, *2*, 1142-1146.

155. Gray, D. S.; Tan, J. L.; Voldman, J.; Chen, C. S. *Biosens. Bioelectron.* **2004**, *19*, 1765-1774.

156. Ermolina, I.; Morgan, H.; Green, N. G.; Milner, J. J.; Feldman, Y. *Biochimica Et Biophysica Acta-General Subjects* **2003**, *1622*, 57-63.

157. Liu, Y. S.; Walter, T. M.; Chang, W. J.; Lim, K. S.; Yang, L. J.; Lee, S. W.; Aronson, A.; Bashir, R. *Lab Chip* **2007**, *7*, 603-610.

158. Markx G, M. T. a. R. P. *J Biotechnology* **1994**, *32*, 29.

159. Lapizco-Encinas, B. H.; Ozuna-Chacón, S.; Rito-Palomares, M. *J. Chromatogr. A* **2008**, *1206*, 45-51.

160. Kuzyk, A.; Yurke, B.; Toppari, J. J.; Linko, V.; Torma, P. *Small* **2008**, *4*, 447-450.

161. Huang, Y.; Joo, S.; Duhon, M.; Heller, M.; Wallace, B.; Xu, X. *Anal. Chem.* **2002**, *74*, 3362-3371.

162. Xu, G. C., M.; Yang, C.; Sukumar, P.; Choolani, M.; Ying, Y. J. *Journal of Physics: Conference Series* **2006**, *34*, 1106-1111.

163. Irimajiri, A.; Hanai, T.; Inouye, A. *J. Theor. Biol.* **1979**, *78*, 251-269.

164. Huang, Y.; Holzel, R.; Pethig, R.; Wang, X. B. *Phys. Med. Biol.* **1992**, *37*, 1499-1517.

165. Asami, K.; Hanai, T.; Koizumi, N. *Biophys. J.* **1980**, *31*, 215-228.

166. Sanchis, A.; Brown, A. P.; Sancho, M.; Martinez, G.; Sebastian, J. L.; Munoz, S.; Miranda, J. M. *Bioelectromagnetics* **2007**, *28*, 393-401.

167. Li, H.; Zheng, Y.; Akin, D.; Bashir, R. *Microelectromech. Syst.* **2005**, *14*, 103-112.

168. Suehiro, J.; Yatsunami, R.; Hamada, R.; Hara, M. *Journal of Physics D-Applied Physics* **1999**, *32*, 2814-2820.

169. Suehiro, J.; Noutomi, D.; Shutou, M.; Hara, M. *J. Electrostatics* **2003**, *58*, 229-246.

170. Su, Y.; Chen, H.; Wang, Z.; Lv, Y. *Appl. Spectrosc. Rev.* **2007**, *42*, 139-176.

171. Barni, F.; Lewis, S. W.; Berti, A.; Miskelly, G. M.; Lago, G. *Talanta* **2007**, *72*, 896-913.

172. Ronaghi, M.; Uhlén, M.; Nyrén, P. *Science* **1998**, *281*, 363-365.

173. Rechberger, W.; Hohenau, A.; Leitner, A.; Krenn, J. R.; Lamprecht, B.; Aussenegg, F. R. *Opt. Commun.* **2003**, *220*, 137-141.

174. Schmid, G.; Simon, U. *Chem. Commun.* **2005**, 697-710.

175. Jain, P. K.; Lee, K. S.; El-Sayed, I. H.; El-Sayed, M. A. *The Journal of Physical Chemistry B* **2006**, *110*, 7238-7248.

176. Abad, J. M.; Mertens, S. F. L.; Pita, M.; Fernández, V. M.; Schiffrin, D. J. *J. Am. Chem. Soc.* **2005**, *127*, 5689-5694.

177. Hostetler, M. J.; Green, S. J.; Stokes, J. J.; Murray, R. W. *J. Am. Chem. Soc.* **1996**, *118*, 4212-4213.

178. Hostetler, M. J.; Wingate, J. E.; Zhong, C.-J.; Harris, J. E.; Vachet, R. W.; Clark, M. R.; Londono, J. D.; Green, S. J.; Stokes, J. J.; Wignall, G. D.; Glish, G. L.; Porter, M. D.; Evans, N. D.; Murray, R. W. *Langmuir* **1998**, *14*, 17-30.

179. Bartz, M.; Kuther, J.; Nelles, G.; Weber, N.; Seshadri, R.; Tremel, W. *J. Mater. Chem.* **1999**, *9*, 1121-1125.

180. Alivisatos, A. P.; Johnsson, K. P.; Peng, X.; Wilson, T. E.; Loweth, C. J.; Bruchez, M. P.; Schultz, P. G. *Nature* **1996**, *382*, 609-611.

181. Lee, J.-S.; Ulmann, P. A.; Han, M. S.; Mirkin, C. A. *Nano Lett.* **2008**, *8*, 529-533.

182. Su, X.; Kanjanawarut, R. *ACS Nano* **2009**, *3*, 2751-2759.

183. Kim, J.-Y.; Lee, J.-S. *Nano Lett.* **2009**, *9*, 4564-4569.

184. Baptista, P.; Pereira, E.; Eaton, P.; Doria, G.; Miranda, A.; Gomes, I.; Quaresma, P.; Franco, R. *Anal. Bioanal. Chem.* **2008**, *391*, 943-950.

185. Yuan, J.; Shiller, A. M. *Anal. Chem.* **1999**, *71*, 1975-1980.

186. Prilutsky, D.; Shneider, E.; Shefer, A.; Rogachev, B.; Lobel, L.; Last, M.; Marks, R. S. *Anal. Chem.* **2011**, *83*, 4258-4265.

187. Tsukagoshi, K.; Nakahama, K.; Nakajima, R. *Anal. Chem.* **2004**, *76*, 4410-4415.

188. Liu, B.-F.; Ozaki, M.; Utsumi, Y.; Hattori, T.; Terabe, S. *Anal. Chem.* **2002**, *75*, 36-41.

189. Bergervoet, P. W. M.; van Riessen, N.; Sebens, F. W.; van der Zwet, W. C. *J. Hosp. Infect.* **2008**, *68*, 329-333.

190. Zhang, Z.-F.; Cui, H.; Lai, C.-Z.; Liu, L.-J. *Anal. Chem.* **2005**, *77*, 3324-3329.

191. Duan, C. F.; Cui, H.; Zhang, Z. F.; Liu, B.; Guo, J. Z.; Wang, W. *J. Phys. Chem. C* **2007**, *111*, 4561-4566.

192. Taton, T. A.; Mirkin, C. A.; Letsinger, R. L. *Science* **2000**, *289*, 1757-1760.

193. Zhao, L.; Sun, L.; Chu, X. *TrAC, Trends Anal. Chem.* **2009**, *28*, 404-415.

194. Li, D.; He, Q.; Cui, Y.; Duan, L.; Li, J. *Biochem. Biophys. Res. Commun.* **2007**, *355*, 488-493.

195. Silverstein, R. M.; Bassler, G. C.; Morrill, T. C., *Spectrometric Identification of Organic Compounds. 4th ed.* . John Wiley and Sons: New York, 1981.

196. Cui, H.; Wang, W.; Duan, C.-F.; Dong, Y.-P.; Guo, J.-Z. *Chemistry – A European Journal* **2007**, *13*, 6975-6984.

197. Yang, X.; Guo, Y.; Wang, A. *Anal. Chim. Acta* **2010**, *666*, 91-96.

198. Cai, S.; Xin, L.; Lau, C.; Lu, J. *Analyst* **2010**, *135*, 615-620.

Appendix A - ACV data analysis and EIS plots with different equivalent circuit fits

ACV experiment data analysis using Creager's approach

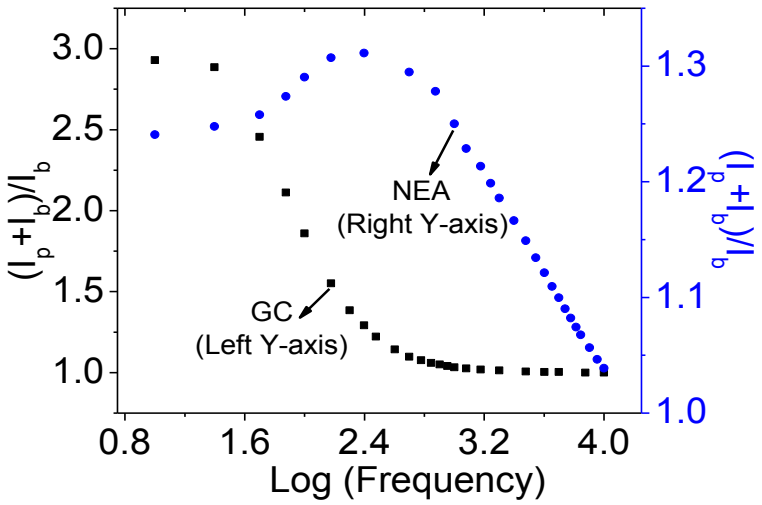

Figure A.1 Plots of $(I_p+I_b)/I_b$ vs. log(frequency) prepared using ACV data shown in Figure 3.7 for the Fc-CH_2-NH_2 modified GCE and CNF NEA, in the fashion reported by Creager et al.[94]

Bode plots of GCE and NEA

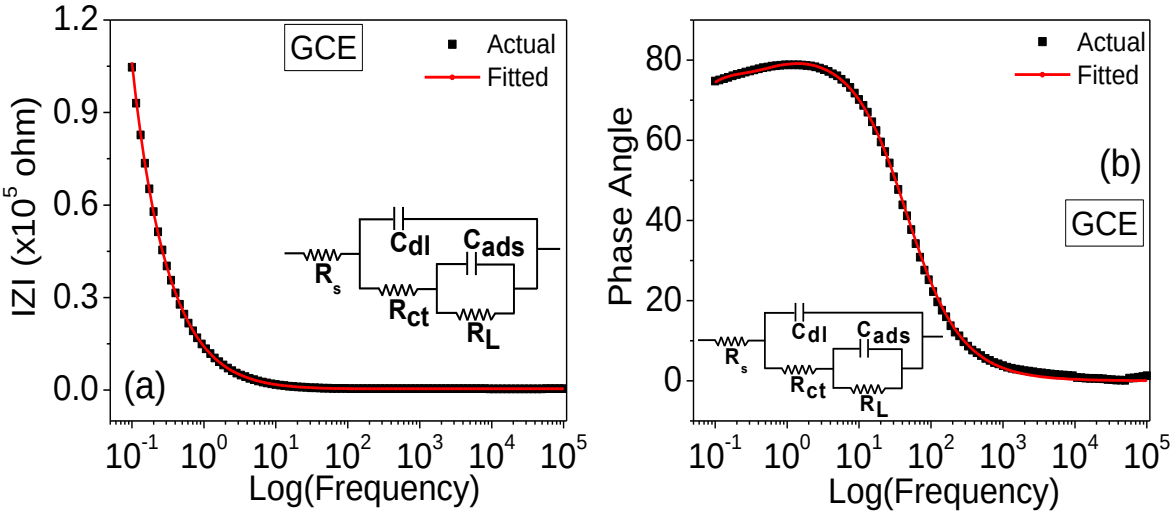

Figure A.2 Bode plots of a GCE functionalized with ferrocene with (a) total impedance vs. log(frequency) and (b) phase angle vs. log(frequency). These are the same EIS data shown in Nyquist plot in Figure 3.11a. The insets are the equivalent circuits used to fit the EIS data.

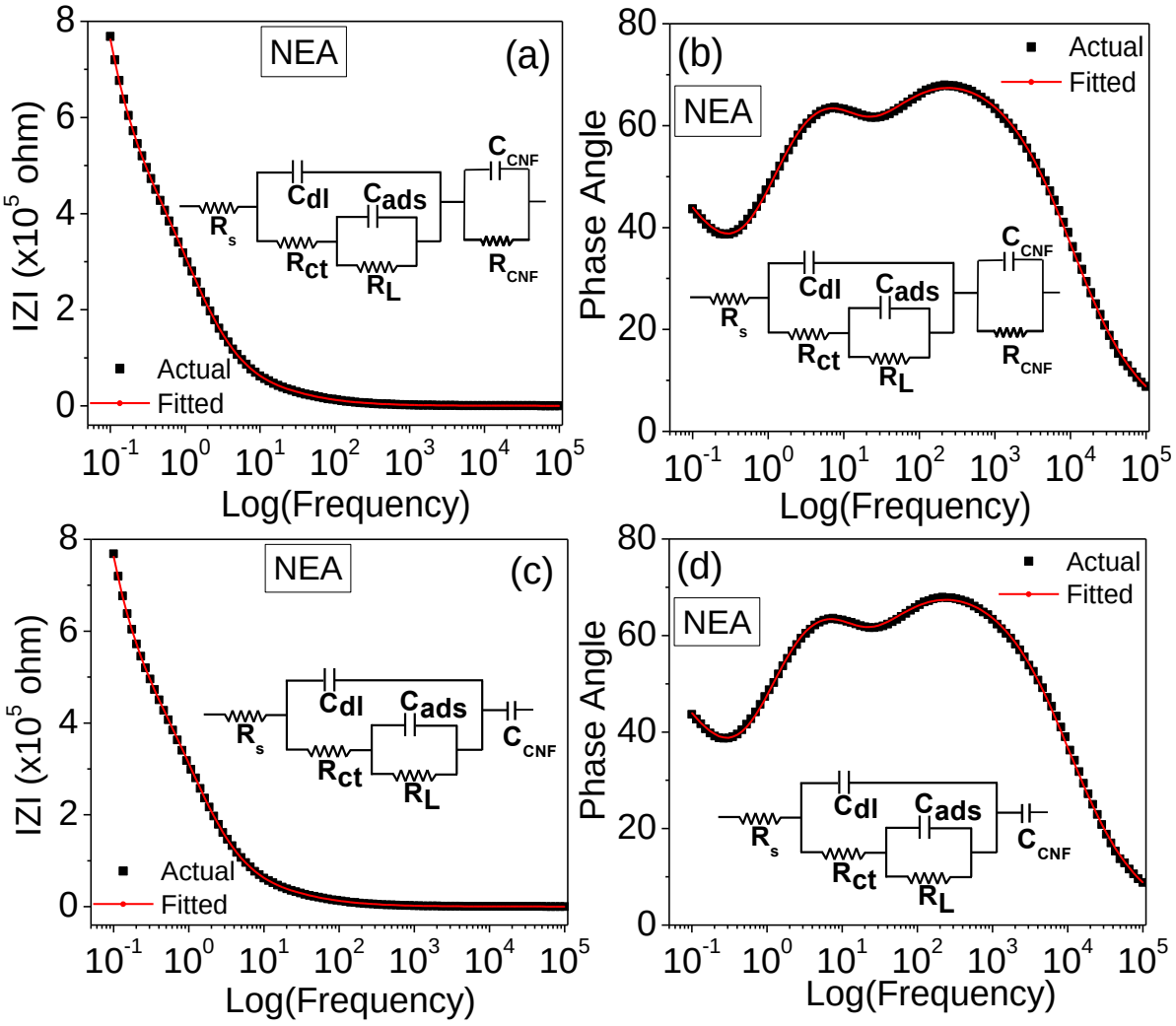

Figure A.3 Bode plots of a CNF NEA functionalized with ferrocene with (a) and (c) the total impedance vs. log(frequency); (b) and (d) phase angle vs. log(frequency). These are the same EIS data shown in Nyquist plot in Figure 3.11b. (a) and (b) use a parallel circuit (C_{CNF} and R_{CNF}) to represent intrinsic properties of the CNF while (c) and (d) only use a single capacitor C_{CNF}. As seen in the figure, the two equivalent circuits fit the experimental EIS data equally well.

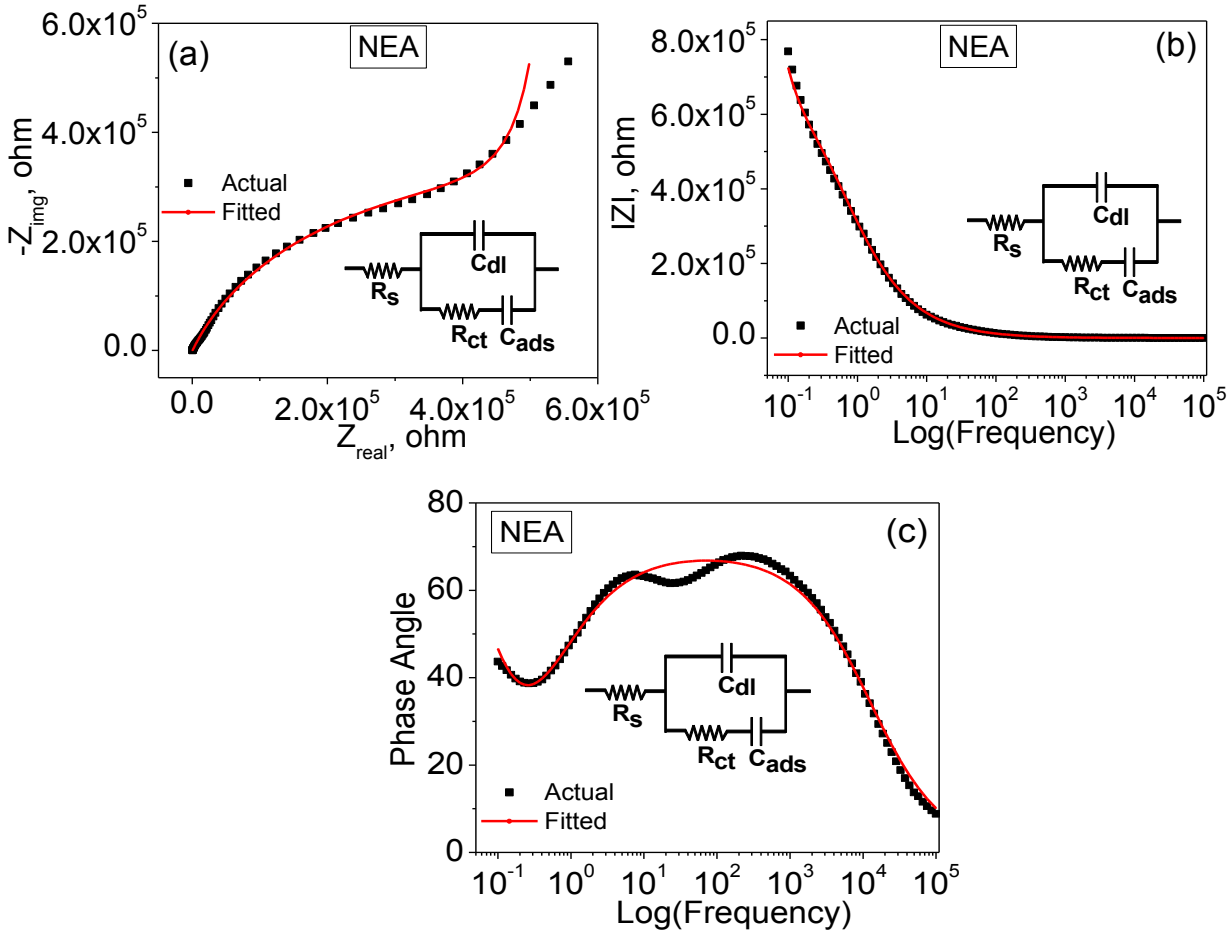

Figure A.4 Nyquist (a) and bode plots of (b) impedance vs. log(frequency) and (c) phase angle vs. log(frequency) of a CNF NEA functionalized with ferrocene, fitted with modified Randles circuit that was used by Creager et al.[94]

Modified Randles circuit which was used by Creager et al. [94] was initially tried to fit the EIS data of the ferrocene functionalized CNF NEA. The plots of which are shown in Figure A.4 and it can be clearly seen that this equivalent circuit cannot fit the data very well. The unsatisfied fitting quality is more obvious when we look at the bode plot (Figure A.4c) of phase angle vs. log(frequency). Particularly, the two peaks at ~5 Hz and ~650 Hz indicate that the circuit should consist of two RC circuits in series as shown in Figure A.3b. This provides strong justification to the equivalent circuit that is used (Figure 3.10b and Figure A.3) to fit the EIS data of the ferrocene-functionalized CNF NEA.

Table A.1 Comparison of the fitting parameters of the two equivalent circuits for the electrochemical impedance spectra of Fc-attached CNF NEA electrodes

Circuit for CNF	R_s, Ω	C_{dl}, F (n)	R_{ct}, Ω	C_{ads}, F (n)	R_L, Ω	C_{CNF}, F (n)	R_{CNF}, Ω	k^o_{ac} (s^{-1})
Parallel C_{CNF}, R_{CNF}	311.3	4.144×10^{-7} (0.864)	5.167×10^4	2.552×10^{-7} (0.976)	2.621×10^5	2.488×10^{-6} (0.707)	2.946×10^7	**38.0**
C_{CNF} only	312.5	4.451×10^{-7} (0.85)	5.997×10^4	2.187×10^{-7}	2.664×10^5	2.561×10^{-6} (0.715)	--	**38.1**

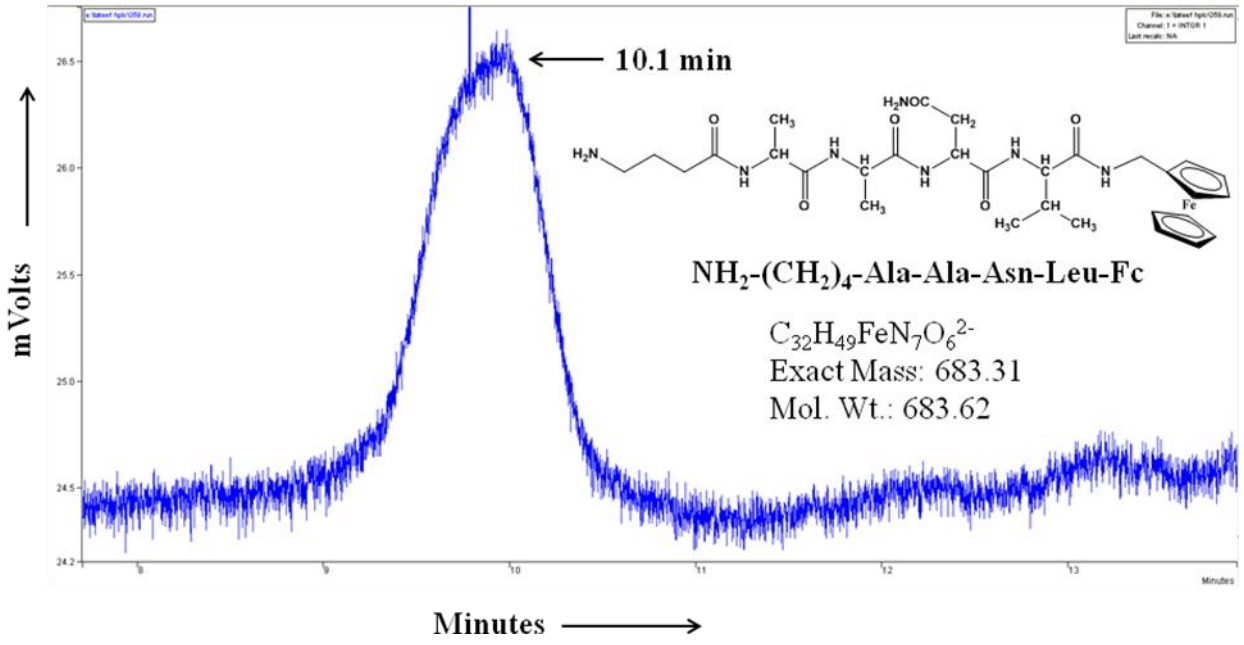

Figure A.5 Chromatogram of authentic ferrocenyl tetrapeptide sample. It elutes at a retention time of ~10.1 min.

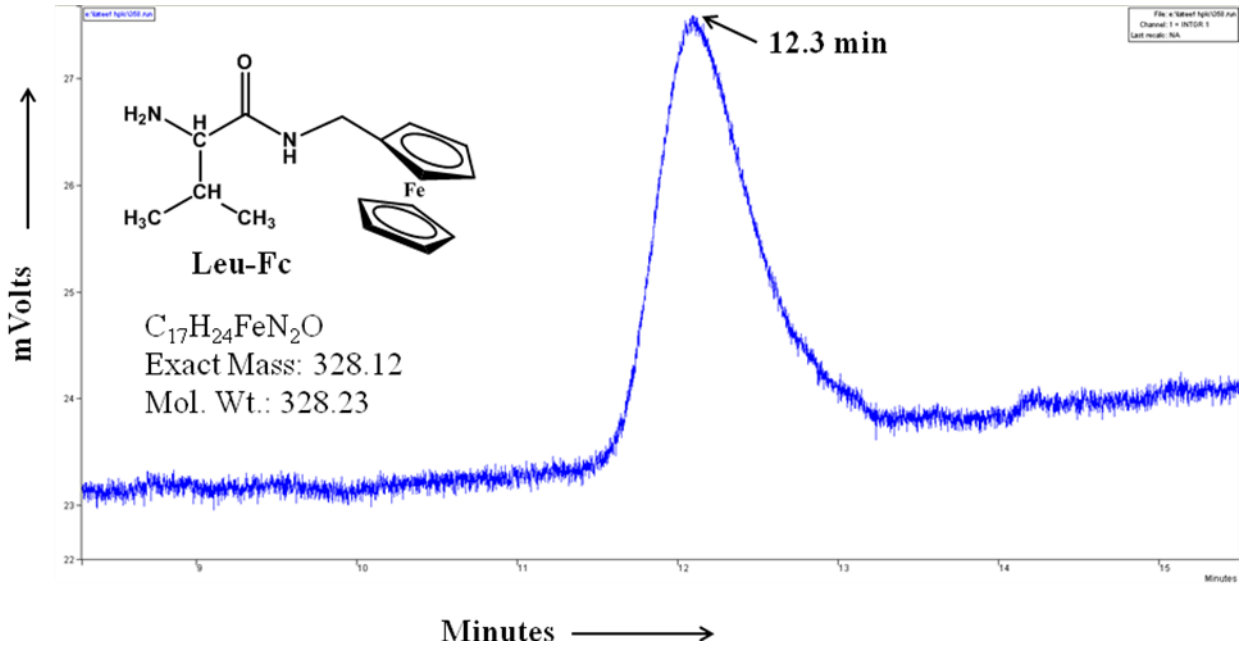

Figure A.6 Chromatogram of authentic fragment Leu-Fc sample. It elutes at a retention time of ~12.3 min.

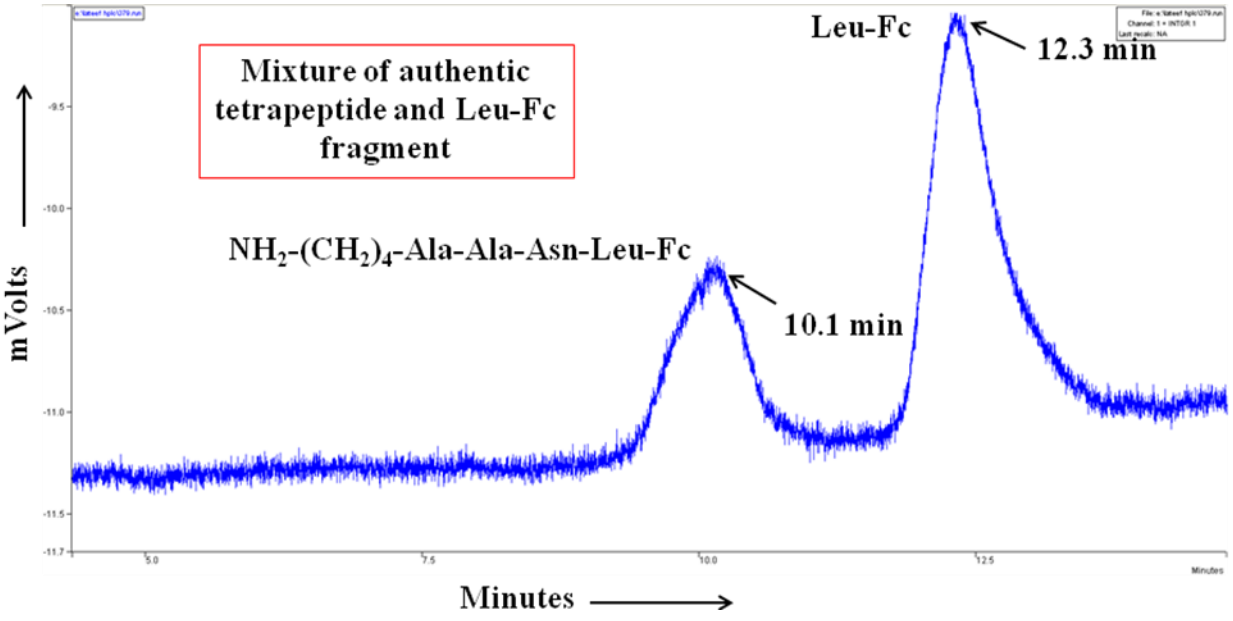

Figure A.7 Chromatogram of a mixture of authentic ferrocenyl tetrapeptide and fragment Leu-Fc sample. Tetrapeptide elutes at ~10.1 min and the fragment at 12.3 min.

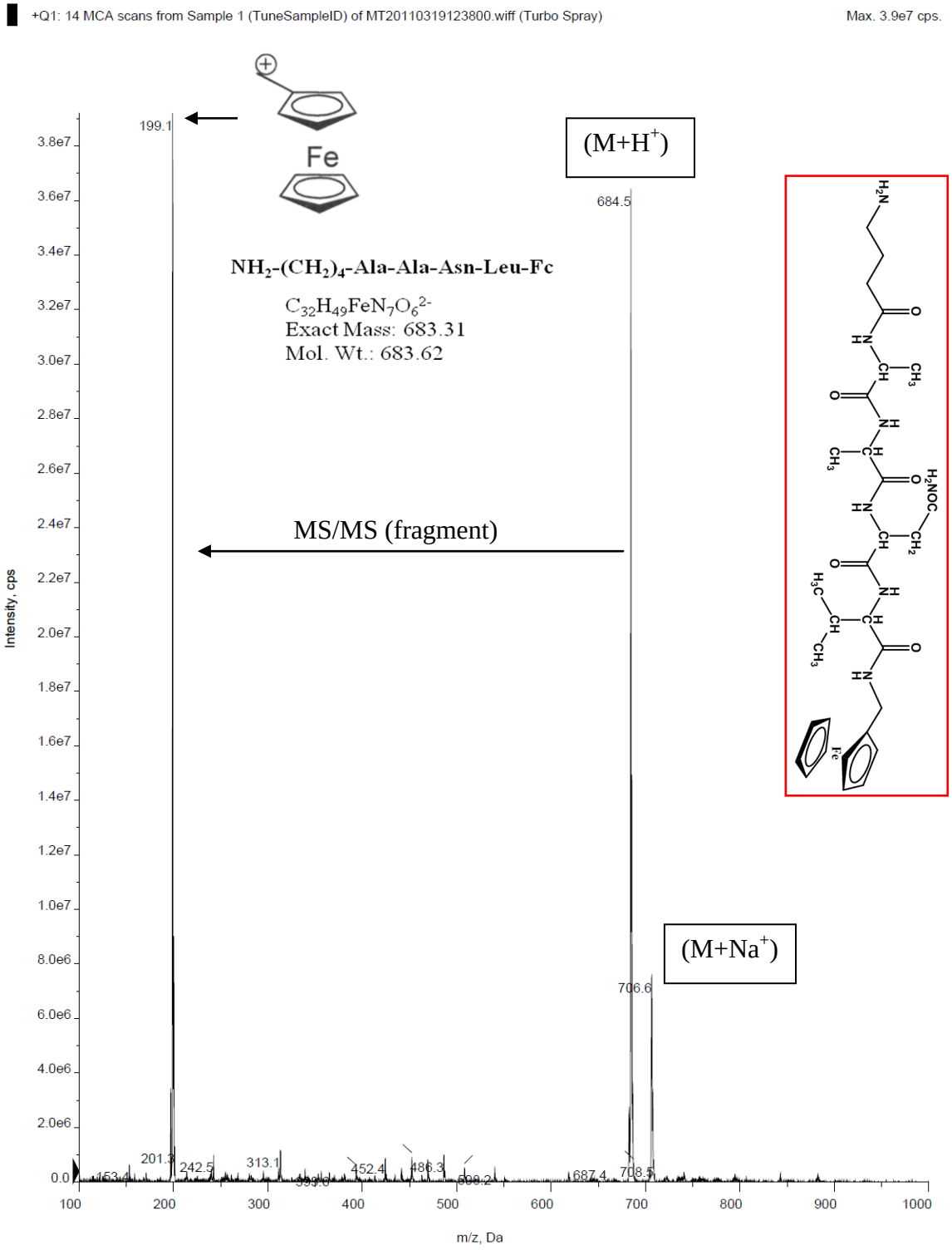

Figure A.8 Mass spectra of authentic ferrocenyl tetrapeptide.

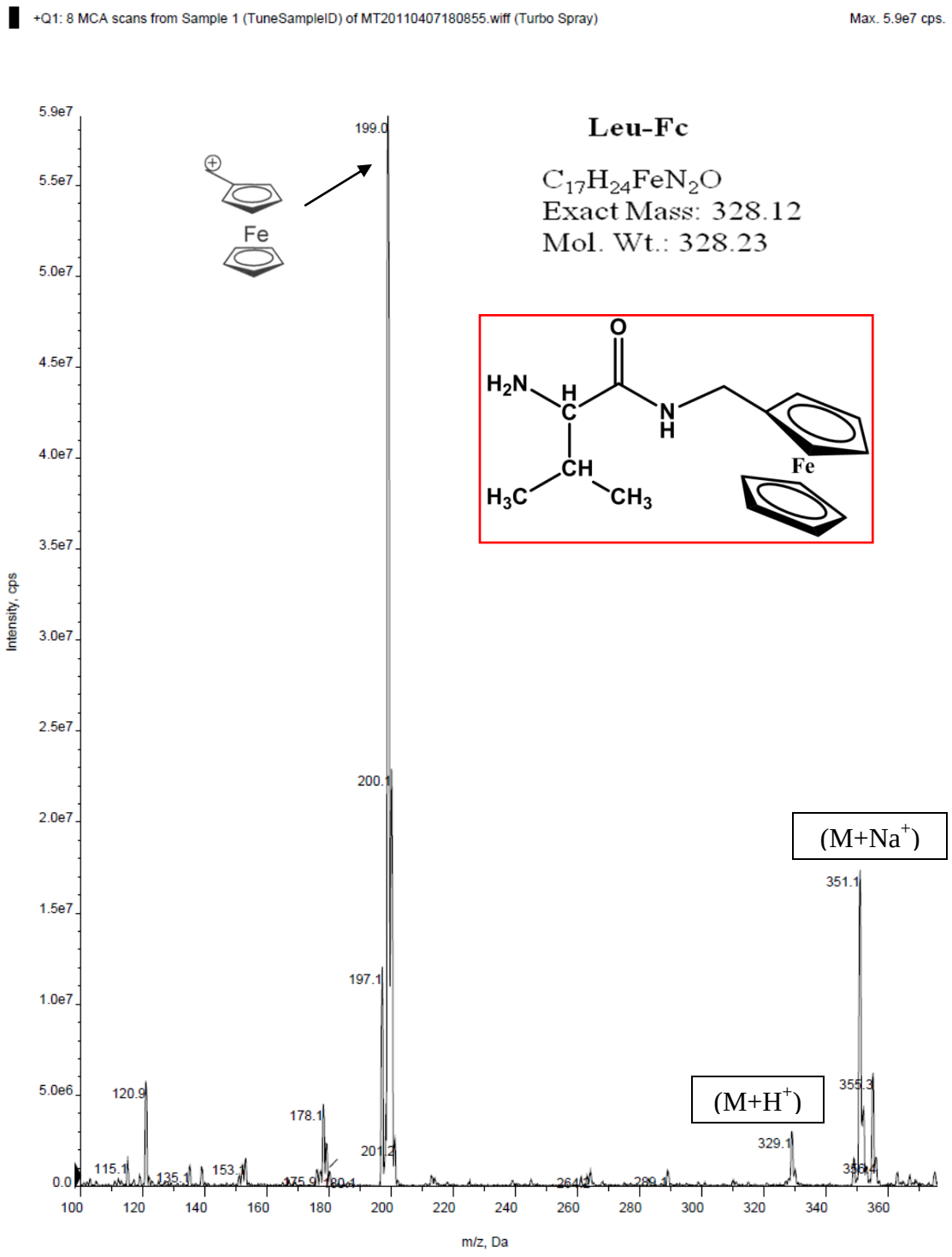

Figure A.9 Mass spectra of authentic Leu-Fc fragment.

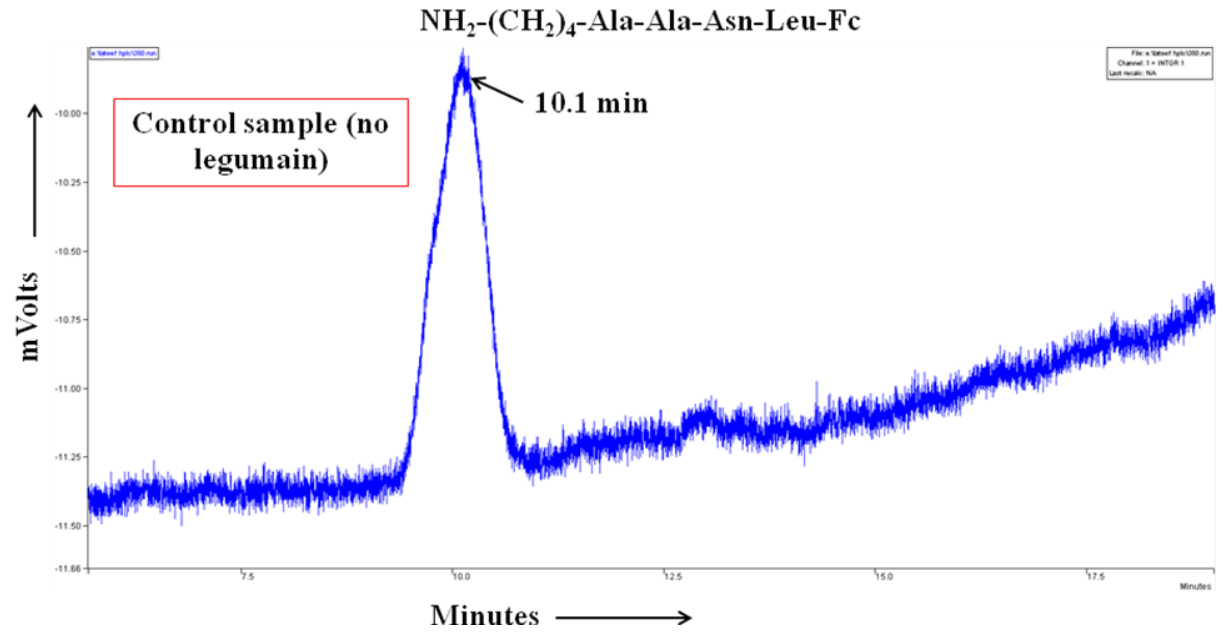

Figure A.10 Chromatogram of control sample i.e. tetrapeptide sample with no legumain added to it. Only one peak at a retention time of 10.1 min can be observed, confirming that no cleavage takes place.

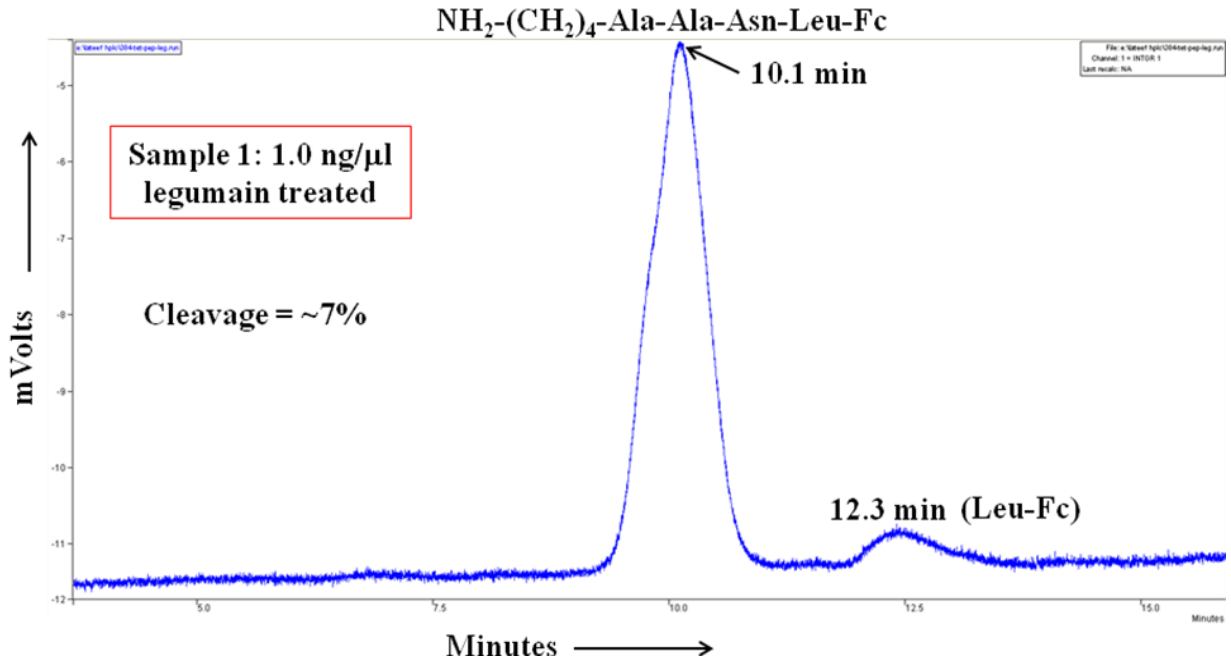

Figure A.11 Chromatogram of tetrapeptide sample (#1) after incubation with 1.0 ng/µl of legumain. Uncleaved tetrapeptide is eluted at 10.1 min and cleaved Leu-Fc fragment is eluted at 12.3 min.

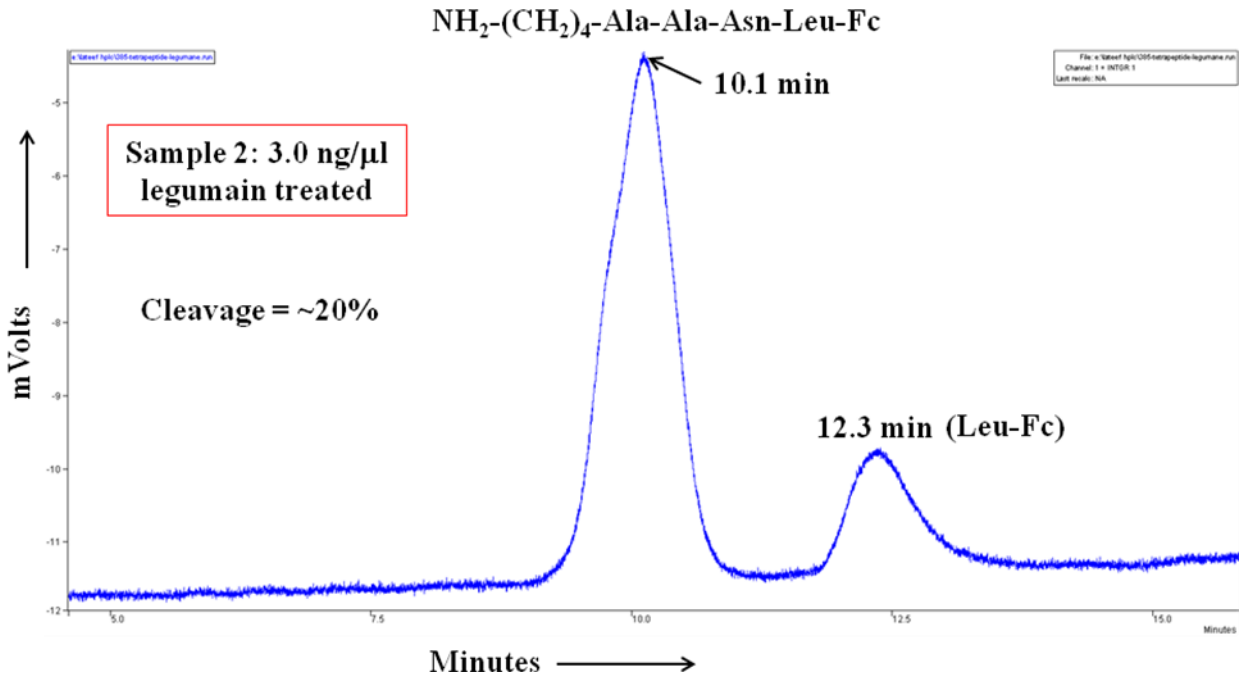

Figure A.12 Chromatogram of tetrapeptide sample (#2) after incubation with 3.0 ng/µl of legumain. Uncleaved tetrapeptide is eluted at 10.1 min and cleaved Leu-Fc fragment is eluted at 12.3 min.

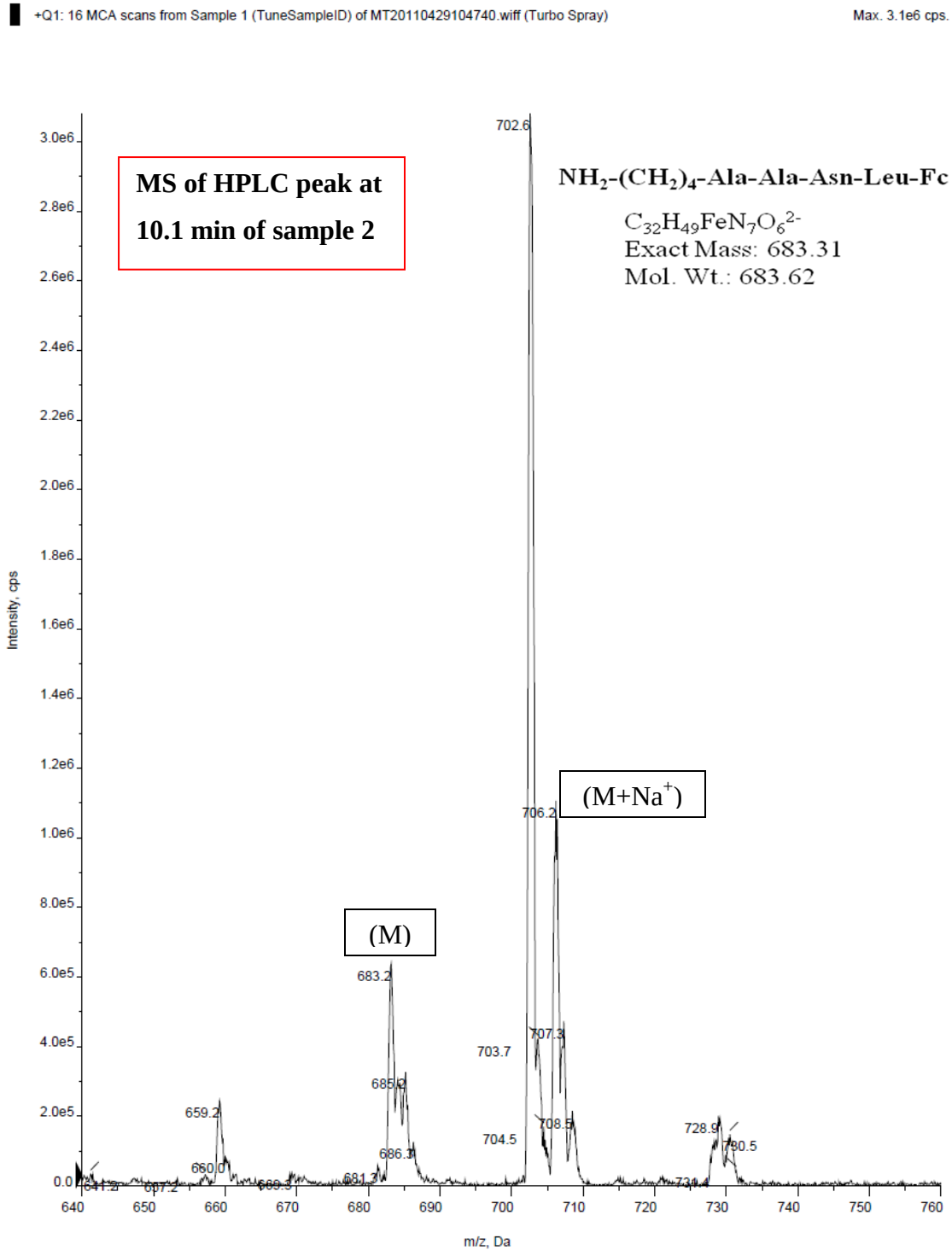

Figure A.13 Mass spectra of peak at 10.1 min of tetrapeptide incubated with legumain (sample #2).

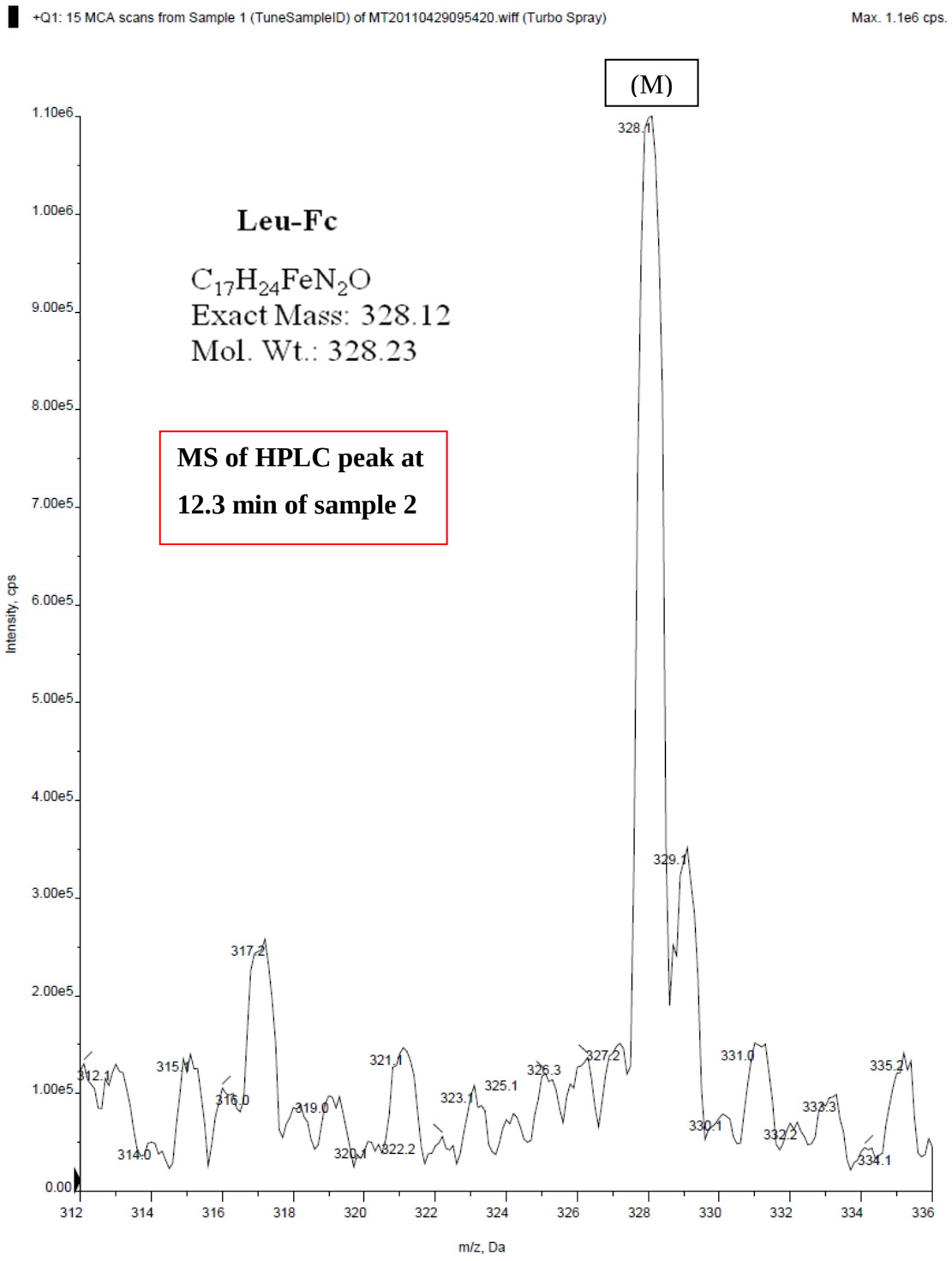

Figure A.14 Mass spectra of peak at 12.3 min of tetrapeptide incubated with legumain (sample #2).

Appendix B - Dielectrophoresis experimental set-up and details

Nano-DEP device and experimental set-up

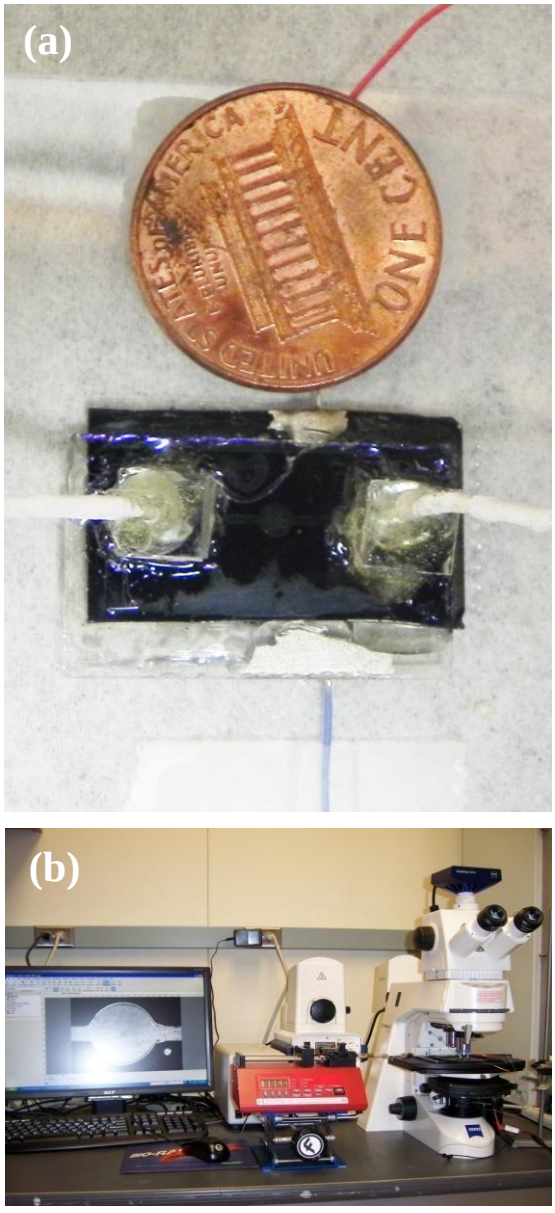

Figure B.1 (a) Shows a nano-DEP device mounted on a glass slide, integrated with microbore tubing and electrical wires. (b) Experimental set-up for DEP and EIS experiments.

Channel heights characterized by a surface profiler

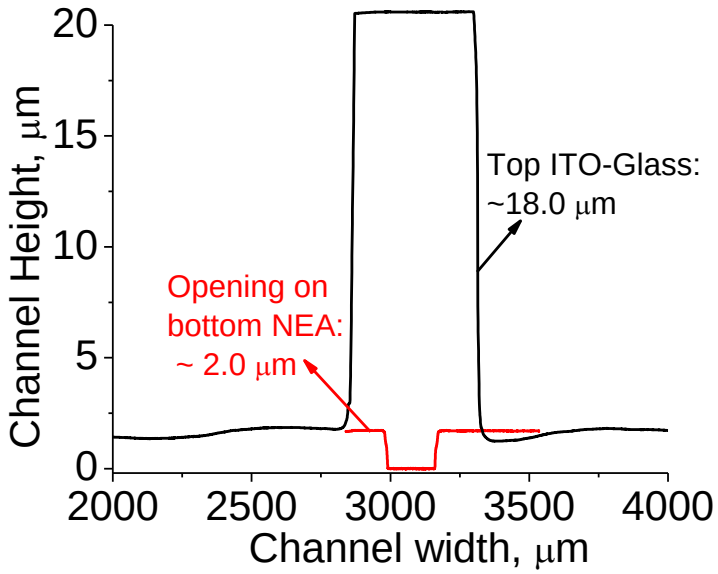

Figure B.2 The microchannel profile measured using profiler. The black curve on the top shows a channel height of ~18.0 μm etched in the SU-8 photoresist on the ITO-glass electrode (flipped upside down in the figure), and the red curve shows the ~2.0 μm deep recessed on the CNF NEA chip to define the 200 μm x 200 μm active area.

Flow velocity profile inside the microfluidic channel

The average flow velocities in the fluidic channel and at the center of the 2 mm diameter circular chamber were calculated from the volumetric flow rate and the channel dimension. More precise flow velocity at the surface of the CNF NEA in the exposed 200 μm x 200 μm area is calculated from the stretched lines in the video. The values are summarized below:

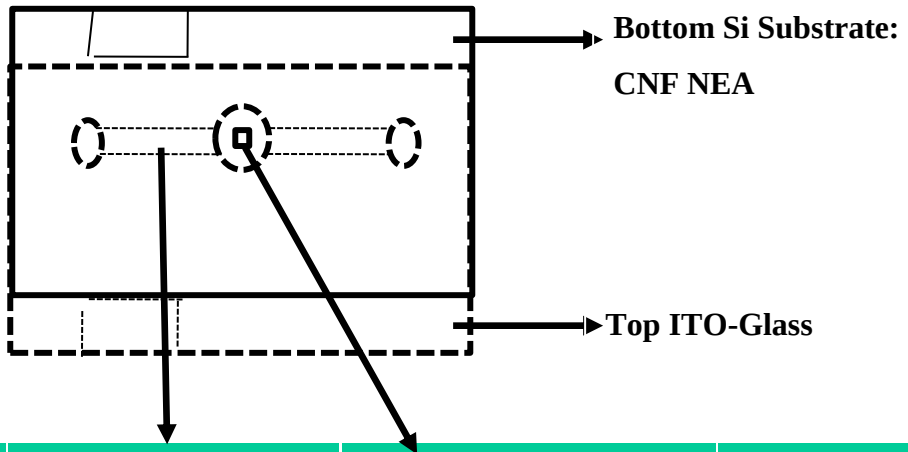

Volumetric flow rate (μl/min)	Average flow velocity in the 500-μm channel	Average flow velocity at the center of the 2-mm dia. circular chamber	Measured flow velocity (From Video)
0.1	0.185 mm/sec	0.046 mm/sec	0.108 mm/sec
0.2	0.370 mm/sec	0.093 mm/sec	0.216 mm/sec
0.4	0.740 mm/sec	0.185 mm/sec	0.432 mm/sec
0.6	1.1 mm/sec	0.278 mm/sec	0.648 mm/sec
0.8	1.5 mm/sec	0.370 mm/sec	0.864 mm/sec
1.0	1.85 mm/sec	0.460 mm/sec	1.1 mm/sec
1.5	2.78 mm/sec	0.695 mm/sec	1.6 mm/sec

Appendix C - Some miscellaneous results related to Chapter 5

UV-Visible spectra of unlysed and lysed sheep blood

Figures C.1a and C.1b below shows UV-Visible spectra of unlysed and lysed blood respectively. As seen in the figures, the lysed sample showed less scattering i.e. less background compared to unlysed blood sample, which is evident by a flat baseline. In case of unlysed blood due to scattering from the intact blood cells higher background can be observed.

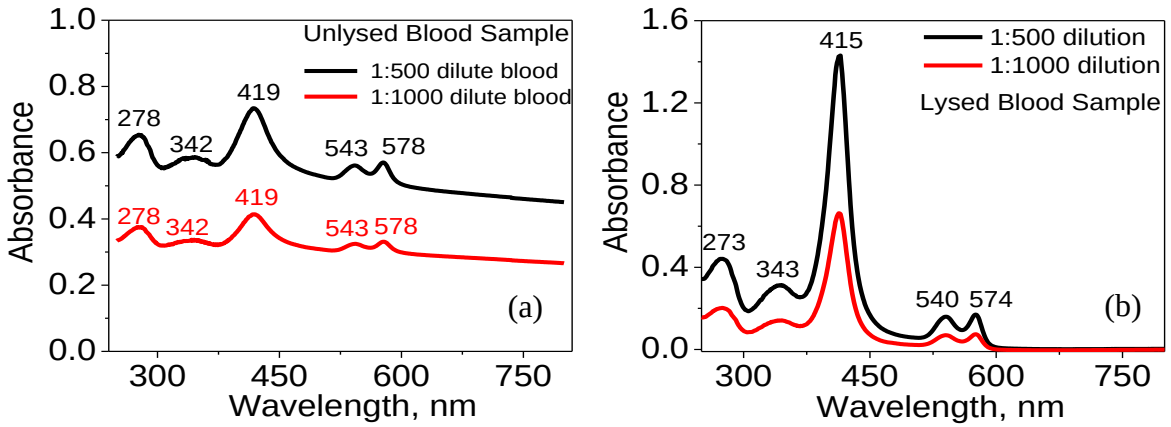

Figure C.1 UV-Visible spectra of (a) unlysed and (b) lysed blood of 500 and 1000 times dilution in 1X PBS buffer.

UV-Visible spectra of luminol

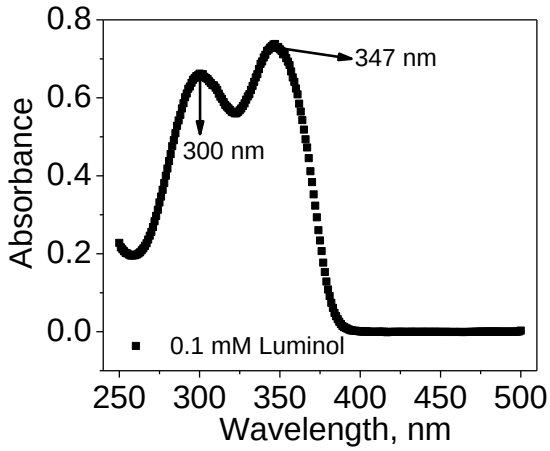

Figure C.2 UV-Visible spectra of 0.1 mM luminol in 0.1 M NaOH solution. Two characteristic peaks at ~347 nm and 300 nm can be seen, consistent with the spectra shown in earlier reports.[1,2]

Chemiluminescence of serially diluted GNP-MUA-LUM solution

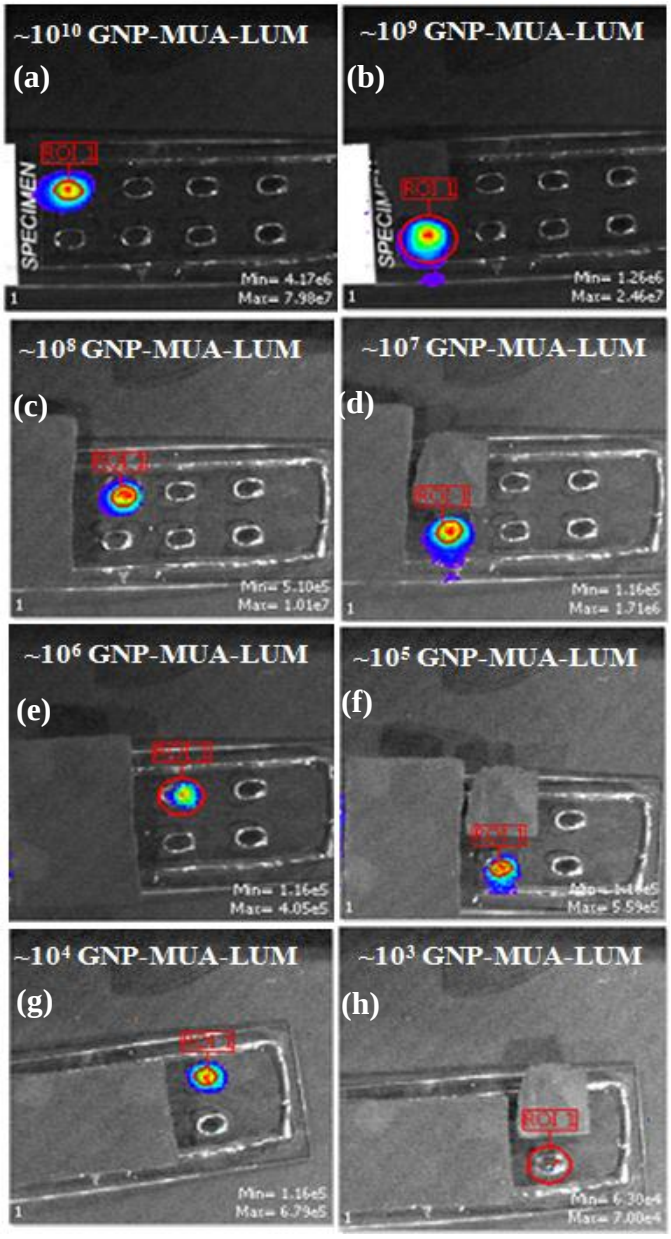

Figure C.3 Chemiluminescence signal recorded by a CCD camera in IVIS Lumina II at PDMS wells loaded with luminol-labeled GNPs (i.e. GNP-MUA-LUM) varying from ~$1.0x10^{10}$ to $1.0x10^{3}$. The images are presented in psuedocolor to represent the chemiluminescence intensities. The number of GNP-MUA-LUM in the well to be measured is indicated on each image. All previously measured wells are covered with a piece of paper to reduce the background.

Comparing chemiluminescence from GNP-MUA-LUM and bulk luminol

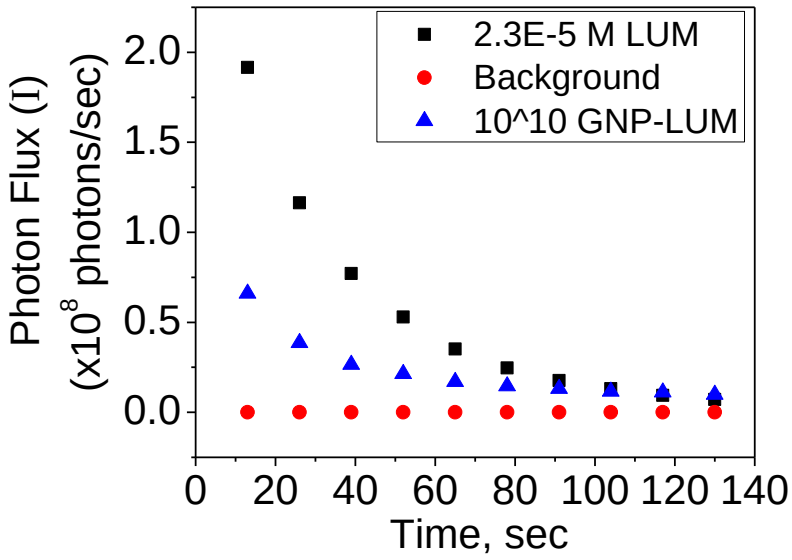

Figure C.4 The comparison of kinetic plots of the CL signal of 1.0×10^{10} luminol-attached gold nanoparticles in a PDMS well (filled triangles), the same amount of luminol molecules dispersed in the solution (filled squares), and blank control sample (filled circles). Each 10-nm-diameter gold nanoparticle is estimated to be attached with ~1.4×10^{3} luminol molecules by assuming the formation of a close-packed monolayer with the same density as that on the flat gold surface. The amount of luminol on 1.0×10^{10} luminol-attached gold nanoparticles is equivalent to 4.0 μL of 23 μM luminol solution used for comparison. The absorption of gold nanoparticles was not corrected.

Analysis of data shown in Figure 5.7 of Chapter 5

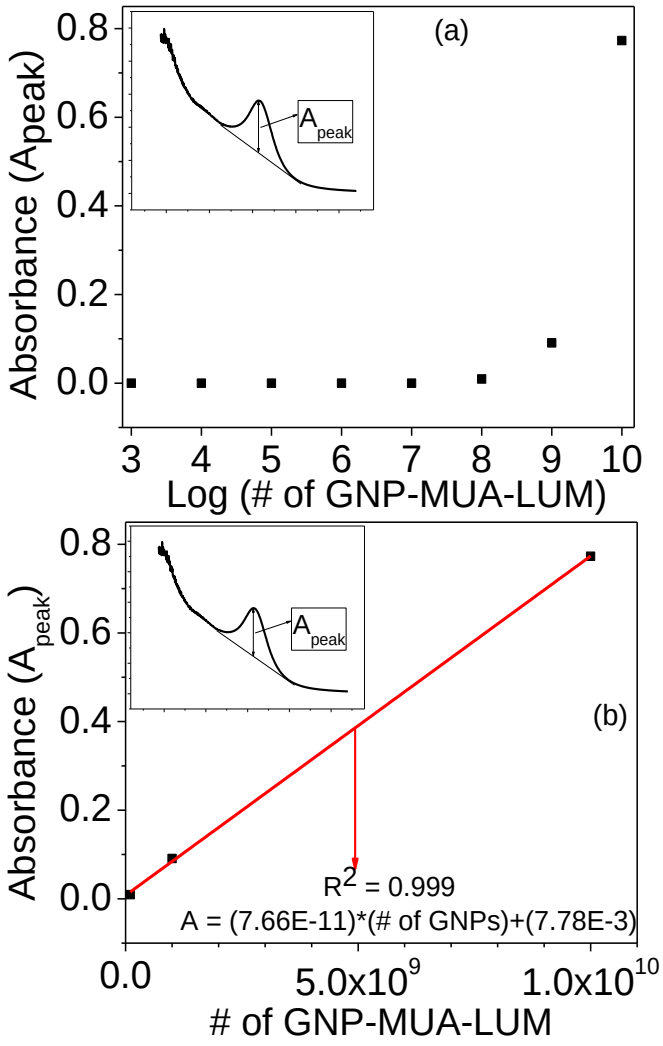

Figure C.5 The background subtracted peak absorption (Apeak) at ~520 nm derived from the UV-visible spectra shown Figure 5.7a and Figure 5.7b. (a) plots the value of A_{peak} vs the logarithm of the number of luminol-labeled GNPs. (b) is the linear plot of A_{peak} vs. number of luminol-labeled GNPs obtained with the sample containing ~$1.0x10^{10}$, $1.0x10^{9}$ and $1.0x10^{8}$ GNP-MUA-LUM. The solid line in (b) is the best fit line, which fits nicely with a linear equation. This indicates that the UV-visible signal linearly decreases till 10^{8} GNPs. At higher dilution (i.e. #GNP-MUA-LUM < 10^{8}) the samples did not show reliable UV-visible signal (as evident from Figure 5.7b). The detection limit by UV-visible absorption is clearly about 10^{7}-10^{8} GNPs/well.

Use of enhancer's to enhance chemiluminescence signal of luminol

It is known that certain enhancers can enhance the CL intensities under appropriate experimental conditions. Commonly p-phenol derivatives are preferred as enhancers to enhance the CL intensity.[3,4] We selected 4-iodophenol as the enhancer to study the CL enhancement effect. CL experiment was performed with 100 times diluted lysed blood sample, along with which 4 μl of 5 mM 4-IP was added. There was ~29 times higher CL intensity observed when compared to the case where no enhancer was added. In future, further careful optimization needs to be done, which may further increase the sensitivity of the CL protocols.

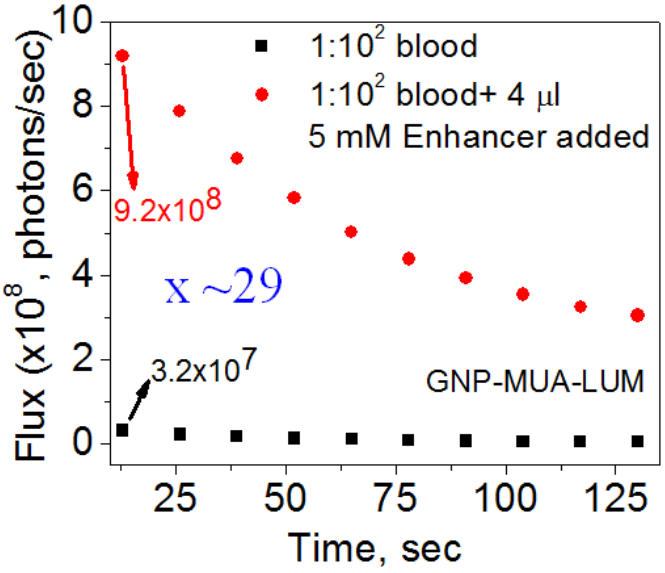

Figure C.6 Chemiluminescence detection of 100 times diluted lysed blood sample with and without enhancer. For the experiment with enhancer 4 μl of 5 mM 4-iodophenol solution (1:1 water and ethanol) was added.

References for Appendix C

1. Sun, Y. G.; Cui, H.; Li, Y. H.; Lin, X. Q. *Talanta* **2000,** *53*, 661-666.
2. Li, S. F.; Li, X. Z.; Xu, J.; Wei, X. W. *Talanta* **2008,** *75*, 32-37.
3. Sanchez, F. G.; Díaz, A. N.; García, J. A. G. *J. Lumin.* **1995,** *65*, 33-39.
4. Kamidate, T.; Maruya, M.; Tani, H.; Ishida, A. *Anal. Sci.* **2009,** *25*, 1163-1166.

Appendix D - List of publications and presentations

Publications

1. Syed, L. U.; Liu, J.; Price, A. K.; Li, Y.-f.; Culbertson, C. T.; Li, J., "Dielectrophoretic Capture of *E. coli* cells at Micropatterned Nanoelectrode Arrays"; *Electrophoresis*, **2011**, 32, 2358-2365 (published in special issue on Dielectrophoresis).
2. Syed, L. U.; Liu, J.; Prior, A. M.; Hua, D. H.; Li, J., "Enhanced Electron Transfer Rates by AC Voltammetry for Ferrocenes Attached to the End of Embedded Carbon Nanofiber Nanoelectrode Arrays"; *Electroanalysis*, **2011**, 23, 1709-1717.
3. Syed. L. U.; Rochford. C.; Wang. F.; Wu. J.; Richter. M.; Balivada. S.; Troyer. D.; Li. J., "An Ultrasensitive Chemiluminescence Method for Trace Blood Detection Using Luminol-Labeled Gold Nanoparticles" manuscript in preparation.
4. Li, Y.-f.; Syed, L. U.; Liu, J.; Hua, D.; Li, J., "Label-free electrochemical impedance detection of kinase and phosphatase activities using nanoelectrode arrays" submitted to *Analytica Chimica Acta*.

Presentations

ORAL

1. Syed, L. U.; Liu, J.; Price, A. K.; Li, Y.-f.; Culbertson, C. T.; Li, J. (2010); "Dielectrophoretic Capture of *E. coli* cells at Nanoelectrode Arrays". Abstracts, 45th Midwest Regional Meeting of the American Chemical Society, Wichita, KS.
2. Syed, L. U.; Madiyar, R. F.; Liu, J.; Price, A. K.; Li, Y.-f.; Culbertson, C. T.; Li, J. (2011); "Using Dielectrophoresis for Reversible Capture and Release of *E. coli* cells at Micropatterned Nanoelectrode Arrays". Abstracts, 46th Midwest Regional Meeting of the American Chemical Society, St Louis, MO.
3. Syed, L. U.; Zhang, L.; Prior, A. M.; Hua, D. H.; Li, J. (2011); "Real-Time AC Voltammetry Based Detection of Cancerous Protease (Legumain) Using

Nanoelectrode Arrays". Abstracts, 46th Midwest Regional Meeting of the American Chemical Society, St Louis, MO.

4. Syed, L. U.; Zhang, L.; Prior, A. M.; Hua, D. H.; Li, J. (Fall-2011); "High-Performance Electrochemical Sensing of Cancerous Protease (Legumain) Using Nanoelectrode Arrays" Abstracts, Materials Research Society, Boston, MA.
5. Syed. L. U.; Rochford. C.; Wang. F.; Wu. J.; Richter. M.; Balivada. S.; Troyer. D.; Li. J. (Spring-2012) "An Ultrasensitive Chemiluminescence Method for Trace Blood Detection Using Luminol-Labeled Gold Nanoparticles" Kansas State University Research Forum, Manhattan, KS.

POSTER

1. Syed, L. U.; Liu, J.; Prior, A. M.; Hua, D. H.; Li, J. (2010); "Distinct Electron Transfer Rates between DC and AC Voltammetry for Ferrocene-Attached Carbon Nanofiber Nanoelectrode Arrays". Abstracts, 45th Midwest Regional Meeting of the American Chemical Society, Wichita, KS.
2. Syed, L. U.; Liu, J.; Price, A. K.; Li, Y.-f.; Culbertson, C. T.; Li, J. (2011); "Dielectrophoretic Capture of *E. coli* cells at Nanoelectrode Arrays". 8th Annual Capitol Graduate Research Summit, Topeka, KS.